UNIVERSITÀ DEGLI STUDI DI MILANO

Department of Physics

PhD School in Physics, Astrophysics and Applied Physics

Cycle XXXIII

Study and Experimental Analysis of an Innovative method for Quench localization in superconducting High Order Magnets

Disciplinary Scientific Sector FIS/01

Director of the school: Prof. Matteo Paris

Supervisor of the Thesis: Prof. Massimo Sorbi

PhD Thesis of:

Samuele Mariotto

Academic Year 2019-2020

Commission of the final examination:

External Referees:
Dr. Giorgio F. Ambrosio
Dr. Pasquale Fabbricatore

Commision Members:
Prof. Ruggero Barni
Prof. Piero Martin
Prof. Lucio Rossi

Final examination:

Date: March 23, 2021

Università degli Studi di Milano, Physics Department, Milano, Italy

List of Publications

- **R. Valente**, et al., "Electromagnetic and Mechanical Study for the Nb_3Sn Cos-Theta Dipole Model for the FCC," in *IEEE Transactions on Applied Superconductivity*, vol. 30, no. 4, pp. 1-5, June 2020, Art no. 4001905, doi: 10.1109/TASC.2020.2972219.
- **M. Sorbi**, et al., "Status of the Activity for the Construction of the HL-LHC Superconducting High Order Corrector Magnets at LASA-Milan," in *IEEE Transactions on Applied Superconductivity*, vol. 28, no. 3, pp. 1-5, April 2018, Art no. 4100205, doi: 10.1109/TASC.2017.2772887.
- **M. Statera** et al., "Construction and Power Test of the Superferric Skew Quadrupole for HL-LHC," in *IEEE Transactions on Applied Superconductivity*, vol. 30, no. 4, pp. 1-5, June 2020, Art no. 4003805, doi: 10.1109/TASC.2020.2979159.
- **S. Mariotto** et al., "Activity on the Sextupole Round Coil Superferric Magnet Prototype at LASA," in *IEEE Transactions on Applied Superconductivity*, vol. 29, no. 5, pp. 1-5, Aug. 2019, Art no. 4004505, doi: 10.1109/TASC.2019.2904462.
- **M. Sorbi** et al., "Construction and Cold Test of the Superferric Dodecapole High Order Corrector for the LHC High Luminosity Upgrade," in *IEEE Transactions on Applied Superconductivity*, vol. 29, no. 5, pp. 1-5, Aug. 2019, Art no. 4001905, doi: 10.1109/TASC.2019.2897113.
- **S. Mariotto**, V. Marinozzi, J. Rysti, M. Sorbi and M. Statera, "Study of a Sextupole Round Coil Superferric Magnet," in *IEEE Transactions on Applied Superconductivity*, vol. 28, no. 3, pp. 1-5, April 2018, Art no. 4003305, doi: 10.1109/TASC.2017.2786267.
- **M. Statera** et al., "Construction and Cold Test of the Superferric Decapole for the LHC Luminosity Upgrade," in *IEEE Transactions on Applied Superconductivity*, vol. 29, no. 5, pp. 1-5, Aug. 2019, Art no. 4004305, doi: 10.1109/TASC.2019.2907197.
- **D. Schoerling** et al., "The 16 T Dipole Development Program for FCC and HE-LHC," in *IEEE Transactions on Applied Superconductivity*, vol. 29, no. 5, pp. 1-9, Aug. 2019, Art no. 4003109, doi: 10.1109/TASC.2019.2900556.

- **M. Sorbi** et al., "Measurements and Analysis of Dynamic Effects in the LARP Model Quadrupole HQ02b During Rapid Discharge," in *IEEE Transactions on Applied Superconductivity*, vol. 26, no. 4, pp. 1-5, June 2016, Art no. 4001605, doi: 10.1109/TASC.2016.2524584.
- **M. Statera** et al., "Construction and Cold Test of the Superferric Octupole for the LHC Luminosity Upgrade," in *IEEE Transactions on Applied Superconductivity*, vol. 28, no. 4, pp. 1-5, June 2018, Art no. 4008705, doi: 10.1109/TASC.2018.2809561.
- **R. Valente** et al., "Baseline Design of a 16 T $\cos\theta$ Bending Dipole for the Future Circular Collider," in *IEEE Transactions on Applied Superconductivity*, vol. 29, no. 5, pp. 1-5, Aug. 2019, Art no. 4003005, doi: 10.1109/TASC.2019.2901604.
- **S. Mariotto** et al., "Fabrication and Results of the First MgB2 Round Coil Superferric Magnet at LASA," in *IEEE Transactions on Applied Superconductivity*, vol. 30, no. 4, pp. 1-5, June 2020, Art no. 4001305, doi: 10.1109/TASC.2020.2972212.
- **L. Fiscarelli** et al., "Magnetic Measurements on the Prototype Magnets of the High-Order Correctors for HL-LHC," in *IEEE Transactions on Applied Superconductivity*, vol. 29, no. 5, pp. 1-5, Aug. 2019, Art no. 4003505, doi: 10.1109/TASC.2019.2899984.

Table of Contents

Chapter 1
Introduction

1.1 Scope of this thesis

This Ph.D. thesis concerns the study of the quench propagation, through electromagnetic and thermal simulations, and the development of a magnetic field measurements system, for the analysis of the field quality, of the new High Order corrector magnets for the Large Hadron Collider upgrade project called High Luminosity LHC. The simulation of the quench development inside the superconducting coil has firstly focused on the analysis of the material properties to reproduce experimental data and secondly on the evaluation of the quench protection system requirements during the powering tests of the magnet. All the simulations have been firstly performed with the program QLASA [1], developed at LASA in Milan and then improved with the combination of QLASA and the STEAM package, developed at CERN [2], to identify the real behavior of the magnet internal voltages. The here presented magnetic field measurements system has been developed in a collaboration framework between INFN Milan and the CERN magnetic field measurement system department and it is based on the classical rotating coil measuring system design. This device is based on the introduction of a system of PCB coils that can be manufactured in the industry with modern technologies which assure accuracy in the building process and low values of uncertainties that cannot be obtained with the previous techniques. Also, the proposed magnetic field measurement system has been developed to be able to measure different types of HO corrector magnets in parallel during the same cryogenic test. This innovation allows measuring at the same time one or more corrector magnets reducing the number of scheduled vertical cryogenic tests which will be necessary to measure all the 54 future HO corrector magnets to be installed in LHC from 2025 to 2027. The high rotational order of the HO corrector represents a challenge for this magnetic field measurement system both for the calibration of the measurements and their accuracy. All the measurements have been compared to 3D simulations of the performances of both the prototypes and the series of the magnets showing a very good agreement both in the principal component of the generated magnetic field and, overall, in the field quality. The 3D electromagnetic simulations have been used also to study the interaction between the different magnets during the energization test and the field quality measurements to better understand the performances of the magnet in the final configuration in

the LHC machine lattice. The main innovative aspect of this thesis concerns the use of this developed magnetic field quality measurement system to evaluate and locate the development of a quench inside the superconducting coils of the magnet. Even if different magnetic measurement system has been already used to detect the development of the quench inside superconducting magnets, lie for example quench antennas, the presented method is based on the measurement of the residual magnetic field which is strongly influenced by the number of the coils quenched in the magnet. By analyzing the magnetic field harmonics produced by the magnetization of the superconductor inside the not-quenched coils, and adding the residual magnetization of the ARMCO Iron, we can precisely identify the quenched coil. Therefore the presented method aims not to detect the development of the quench inside a superconducting magnet, helping to trigger the protection system but is capable to reconstruct, after the magnet discharge, the exact location of the quench. This feature can help during the construction processes of a superconducting magnet prototype to identify weak points of the magnet and also can help during the series production to highlight possible degradation of the superconducting coils which limit the performances of the magnet.

1.2 Thesis Structure

To better introduce the work performed on the quench protection and on the magnetic measurement system describing how we can localize the quench inside the superconducting HO corrector magnets, a brief introduction to accelerators and superconducting magnets is here described in Chapter 1. This introduction aims to describe the scope of a particle accelerator and in particular of particle accelerator colliders which are currently the most powerful accelerator machines to better understand particle physics at high energy scales and the rules which govern particle interactions and their properties. The introduction focuses on the description of the magnetic field produced by a superconducting magnet and how the magnetic field quality can be measured and qualified. The basic notion of magnetic field harmonics is introduced to allow the comprehension of the results of the simulations and data analysis performed during the tests of the magnets. A brief description of the theoretical frame of the rotating coil method for the magnetic measurement system is introduced highlighting the correlation between the magnetic field harmonics and the Fourier decomposition of the voltage induced in the rotating coil PCB. A brief introduction to the High Luminosity LHC upgrade project is introduced in Chapter 2 to better describe the motivation and the requirements for the development of the new superconducting magnet on which this thesis work is performed. A detailed description of the HO corrector electromagnetic and mechanical design is reported together with the description of the development of the new

magnetic measurement system installed at the INFN-LASA laboratories in Milan. To optimize the design of the new magnetic measurement system a set of electromagnetic 3D simulations have been performed. The final configuration obtained for the shaft assure that the cross-talking between the magnet during the cryogenic powering test is negligible. The same set of simulations has been performed also for the configuration of the magnet when installed at LHC showing the same results of the vertical test configuration. Finally, examples of real data of magnetic field quality, taken during the last phase of the prototype development and the first batch of the magnet series, are compared with the 3D electromagnetic simulations showing very good performances of the produced magnet. The quench protection study of the HO corrector magnets is reported in Chapter 3. A brief introduction to the superconductivity is reported together with the description of the main problems which has to be faced during a quench development inside a superconducting magnet. The superconductor wire and all the coils properties are described together with the comparison of the calculated expected differential inductance of the magnet with real data taken from the powering of corrector magnet prototypes. The simulations of the real quench that happened during both the prototype development phase and the series production, are in very good agreement with the data obtained demonstrating high accuracy of the models used. The most innovative aspect of this thesis is reported in Chapter 4. A brief introduction on the observed behavior of the residual magnetic field measured in the HO corrector magnets is reported. An analytical model of the expected behavior of the superconductor coil magnetization contribution is reported with the comparison with experimental data. After the analytical model, a detailed FEM model and 2D simulations are described with the comparison with experimental data showing the possibility to locate exactly the quenched coil inside the superconducting magnet for any rotational order of the main harmonic produced. Finally, the conclusion of this Ph.D. work is reported with discussed future perspectives for additional analysis of this new type of investigation of the quench development inside superconducting magnets.

1.3 Particle Accelerators: Colliders

In the research field of particle physics, accelerators are used to bring the speed of charged particles, such as protons or electrons, near the speed of light. The main goal of this acceleration is to create collisions among the accelerated particle or between the accelerated particle and a fixed target. Depending on the type of particle in the collision, part of the energy of the relativistic accelerated particles is used in the interaction to produce hadron and lepton showers which cascade is revealed and reconstructed by the high energy physics detectors. By studying the particle generated during the interaction, physicists can

retrieve their properties and observe their interactions with the known ones understanding the fundamental laws which rule our Universe and all the matter. To accelerate particles both electric and magnetic fields are used. However, only the electric field is used to increase particle energy and speed reaching a very high fraction of the light speed. Two types of particle accelerators can be used, linear accelerators, which use mainly radiofrequency cavities with high values of an electric field to increase the energy of the traveling particles and their linear acceleration, and circular ones, where particles are bent by dipole magnets and longitudinal accelerated by radiofrequency cavities. The main advantage of a circular accelerator, instead of a linear one, is the possibility of keeping the particles in the same set of radiofrequency cavities which are used firstly, to increase the energy of the particle at the working point, and secondly to compensate the beam energy loss during the revolution inside the machine. As already said, to keep the particle confined and controlled in the center of the circular accelerator huge main dipole magnets create the needed Lorentz Force provided by the magnetic field produced. Usually, in a particle accelerator, many charge particles are accelerated together in the same set of magnets and RF cavities. To compensate for the divergence of the beam, due to the mutual repulsion of the particles and additional instabilities, the use of a unique dipolar magnetic field is not enough. A quadrupolar magnetic field in the cross-section plane of the beamline provides a focusing effect in one direction and a defocusing effect in the other one. To provide a net focusing effect in both the transversal directions of the beamline, two quadrupolar magnets, rotated by 90° between them and alternated with dipole magnets, are used in the so-called *FODO* cell. The net focusing effect keeps the dimensions of the beam limited in the transversal direction to beam one, providing an oscillation pattern which is a function of the two quadrupolar magnets gradient and the distance between them. In the particle physics frame, circular accelerators are used as colliders where two counter-rotating beams are accelerated at the same time and then focused in specific interaction points where the particle physics experiments are located. Today, the most powerful collider in the world is the Large Hadron Collider near Geneva in Switzerland, see Fig. 1.1. The particles travel through a 27 km tunnel and are accelerated up to the energy of 7 TeV for each colliding beam. The energy of the particle collision is fixed by the maximum energy which the bending magnet can accept. By fixing the length of the collider, and so the radius of each single bending magnet, the relativistic energy of every single bunch can be calculated as E=0.3BR where the curvature R is measured in km, the main dipole magnetic field B is measured in Tesla and the energy in TeV. To increase the nominal energy of the collider two possible solutions can be adopted: increase the length of the collider and so the bending radius or increase the magnetic field strength. The dimensions of the accelerator have many different constraints and its costs increase with

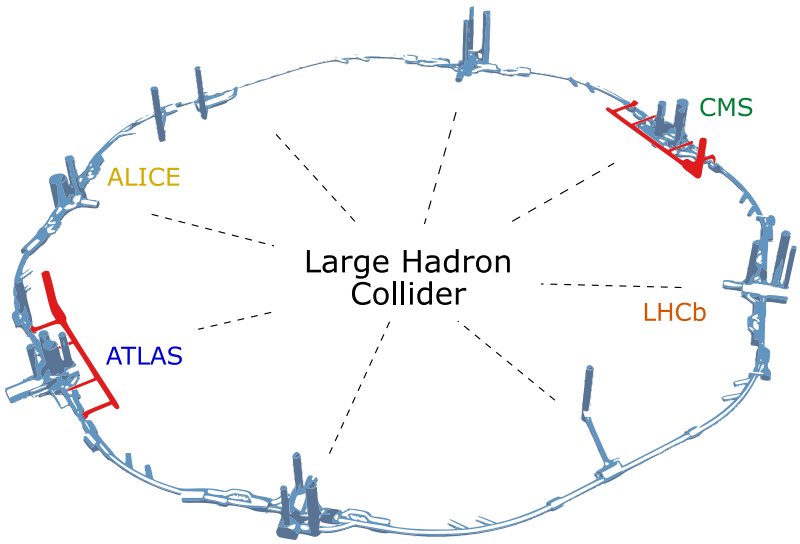

Figure 1.1: *Sketch of the underground structure of the Large Hadron Collider. The sketch has been simplified for clarity and the main interaction points are highlighted*

the length of the tunnel which contains the machine. To keep the dimensions reasonable, the only way to exploit higher particle energy is to increase the magnetic field of the main bending dipoles of the accelerator. Starting from the history of the accelerator, electromagnets were able to generate magnetic fields up to 1/1.5 T with only copper coils and up to 2 T combining copper coils with iron yokes. However, to overcome the iron saturation for magnetic fields higher than 2 T, the use of copper coils cannot be longer considered due to their large occupied volumes and high values of loss energy through the joule effect. Therefore, nowadays, superconducting magnets are mainly used for particle accelerators thanks to their ability to transport a huge amount of current without heat generation and their compact dimensions. LHC uses more than 1200 superconducting magnets with a nominal main magnetic field of 8.33 T which provides collision energy of $\sqrt{s}$=14 TeV in the mass center frame, see Fig. 1.2. Because the accelerated particles have the same charge but travel in counter-rotating directions, also the directions of the magnetic field have to be flipped between the two beams. To reduce the space in the tunnel occupied by the magnets, the two beams are bent by the same superconducting dipoles in the twin-aperture configuration. The magnetic field is produced in both the two beamlines by $\cos\theta$ NbTi superconducting coils. The electromagnetic forces acting on the coils during energization are managed by a single mechanical structure made by a stainless-steel collar and the magnetic field flux lines are focused on the bore through the iron yoke surrounding the structure. Both protons and heavy ions can be accelerated and bring to the collision in the 4

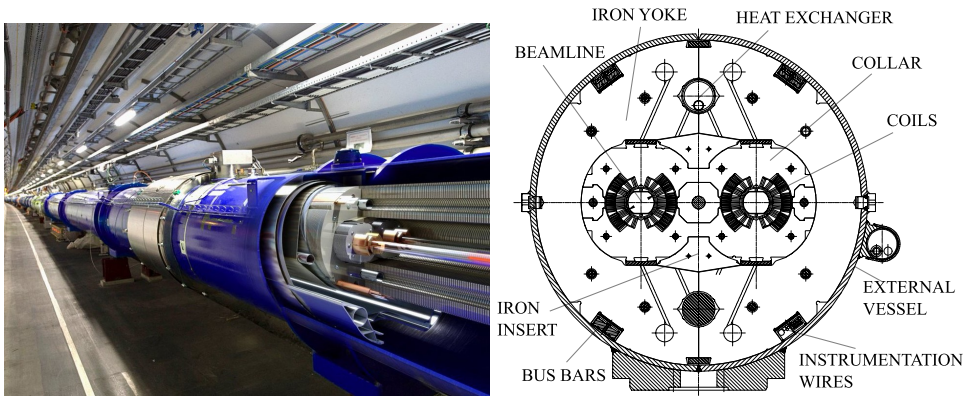

Figure 1.2: *Rendering of an LHC main dipole cut to observe the particle bunches traveling in the tunnel [3](left). Cross section of an LHC dipole. The mechanical structure is highlighted and the different connection and superconducting coils are clearly visible [4],(right).*

main interaction points where the ATLAS (IR1), CMS (IR5), ALICE (IR2), and LHCb (IR8) experiments are located. Near the interaction point, a particular configuration of quadrupole magnets, called low-β^* quadrupoles, squeeze the particles in a quasi-single point to increase the number of possible interactions for the particle physics research. The rate number of collisions produced in the collider can be described by the luminosity of the accelerator. The total number of collisions per second can be obtained by multiplying the luminosity L of the collider and the cross-section σ_{pp} of the interaction, see Eq. 1.1.

$$\frac{dN}{dt} = L\sigma_{pp} \quad \text{where} \quad L = fN_b\frac{N_1N_2}{4\pi\sigma_x\sigma_y} \tag{1.1}$$

The luminosity is directly proportional to the revolution frequency of the particles and the number of particles in each colliding bunch and by squeezing the beam sizes (σ_x,σ_y) at the interaction points through the focusing quadrupoles, the number of particle collisions can be increased by several orders of magnitude. The use of dipoles and quadrupoles in a particle collider, however, is not sufficient to assure the stability of the beam. All the magnets used in an accelerator have imperfections due to construction process errors or technical limits which cannot be overcome and could cause resonant instabilities in the beam bringing to the loss of the bunches. To compensate them, additional magnets with a higher order of rotational symmetry are installed in the accelerator and tuned according to the results of the beam stability analysis.

1.4 Magnetic Field Harmonics

To describe the magnetic field quality of a single particle accelerator magnet we can decompose the generated magnetic field in the known magnetic field harmonics, [5]. In the bore area, where no current sources are present, we can set the divergence of the magnetic field to zero and consider the null curl of the magnetic field to obtain the following set of equation:

$$\frac{\partial B_x}{\partial x} + \frac{\partial B_y}{\partial y} = 0 \quad \frac{\partial B_x}{\partial y} - \frac{\partial B_y}{\partial x} = 0 \tag{1.2}$$

where the x and y directions identify the cross section plane of the magnet. These equations, however, are only valid if $\frac{\partial B_z}{\partial x} = 0$, $\frac{\partial B_z}{\partial y} = 0$ and $\frac{\partial B_z}{\partial z} = 0$ which means that the longitudinal field is constant inside the magnet. By extending the magnetic field definition to the complex variables described in Eq. 1.3 the new variable is an analytic function of the complex variable $\mathbf{z} = x + iy$ satisfing the Cauchy-Riemann condition.

$$\mathbf{B} = B_y(x, y) + iB_x(x, y) \tag{1.3}$$

The new definition of the magnetic field can so be rewritten as a power series of the complex variable $\mathbf{z}$ with complex coefficients $\mathbf{C}_n$ as described in Eq. 1.4.

$$B_y(\mathbf{z}) + iB_x(\mathbf{z}) = \sum_{n=1}^{\infty} \mathbf{C}_n \left(\frac{x + iy}{R_{ref}} \right)^{n-1} \tag{1.4}$$

The complex coefficients of the power series, called magnetic field harmonics, can be also decomposed in their real and complex parts and normalized to a fixed reference radius value R_{ref} from the central rotational axis of the magnet often calculated as 2/3 of the magnet bore radius.

$$\mathbf{C}_n = B_n + iA_n \tag{1.5}$$

$$B_y(\mathbf{z}) + iB_x(\mathbf{z}) = \sum_{n=1}^{\infty} (B_n + iA_n) \left(\frac{x + iy}{R_{ref}} \right)^{n-1} \tag{1.6}$$

The normal and skew components of the harmonics identify the two same components of the magnetic field for each of the rotational order of the magnet, as we can see in Fig. 1.3. Because the optimization process of the magnet design aims to create a pure 2m-order magnet, where m is the rotational order symmetry in the magnetic field, often the magnetic field harmonics are also normalized to the main field harmonic component B_m and multiplied by a 10^4 factor becoming measured in *units*, see Eq. 1.7.

$$B_y(\mathbf{z}) + iB_x(\mathbf{z}) = 10^{-4} B_m \sum_{n=1}^{\infty} (b_n + ia_n) \left(\frac{x+iy}{R_{ref}} \right)^{n-1} \tag{1.7}$$

In a dipole magnet, the main normal component B_1 is equal to the magnetic field at the center of the magnet, while, for a quadrupole magnet, the main field component B_2 is linked to the generated gradient by the relationship G=B_2/R_{ref}. The obtained coefficients are so called "*normalized multipoles*" and they measure the accuracy of a magnet to the ideal perfect 2m-order magnetic field that has to be produced by it. The normalized multipoles can be so directly obtained from the magnetic field harmonics using the Eq. 1.8.

$$\mathbf{c}_n = b_n + ia_n = 10^4 \frac{\mathbf{C}_n}{B_m} = 10^4 \left(\frac{B_n}{B_m} + i \frac{A_n}{B_m} \right) \tag{1.8}$$

Using the cilindrical coordinates and knowing the trigonometric transformation $(cos(\phi)+isin(\phi))^n = (e^{i\phi})^n = e^{in\phi} = (cos(n\phi)+isin(n\phi)$, each single component of the magnetic field, in the magnet cross-section, can then be rewritten as function of the normal and skew component of the harmonics:

$$B_x(r,\theta) = \sum_{n=1}^{\infty} \left(\frac{r}{R_{ref}} \right)^{n-1} (B_n sin((n-1)\theta) + A_n cos((n-1)\theta)) \tag{1.9}$$

$$B_y(r,\theta) = \sum_{n=1}^{\infty} \left(\frac{r}{R_{ref}} \right)^{n-1} (B_n cos((n-1)\theta) - A_n sin((n-1)\theta)) \tag{1.10}$$

$$B_r(r,\theta) = \sum_{n=1}^{\infty} \left(\frac{r}{R_{ref}} \right)^{n-1} (B_n sin(n\theta) + A_n cos(n\theta)) \tag{1.11}$$

$$B_\theta(r,\theta) = \sum_{n=1}^{\infty} \left(\frac{r}{R_{ref}} \right)^{n-1} (B_n cos(n\theta) - A_n sin(n\theta)) \tag{1.12}$$

1.5 Rotating Coils

Many different methods to measure the magnetic field harmonics are used in the currently operating research centers which produce superconducting magnets. According to different aspects of the produced magnet, like for example its length, the bore diameter, the order, if it is normal conductive or superconducting, many technologies for the measure of the magnetic field harmonics reach different accuracy and have different sources of errors. One of the main techniques used for superconducting accelerator magnets is the "Harmonic Rotating Coil Method". This method allows to sample the magnetic flux variation linked to a rotating coil in the magnet bore and correlate this function of the

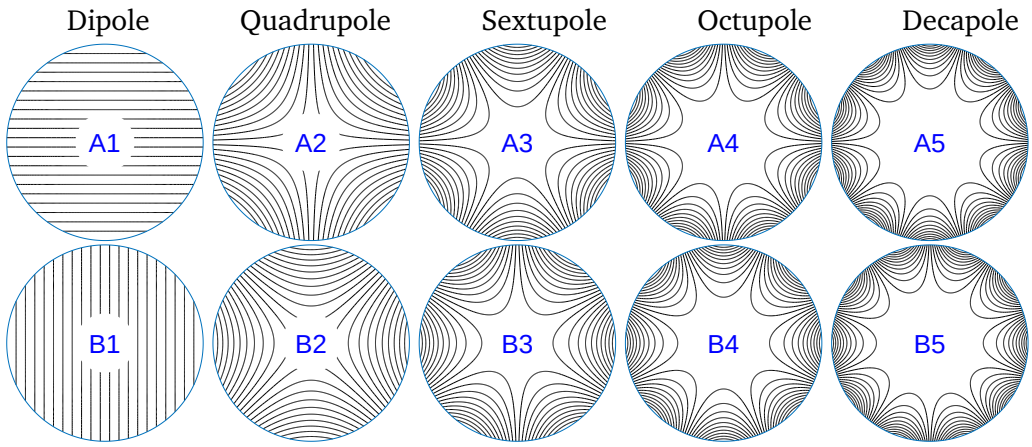

Figure 1.3: *Isolines of the magnetic field produced by the different magnet order inside the bore.* ***Top layer****: skew configuration of a magnetic field.* ***Bottom layer****: normal configuration.*

angular position with all the different n-order magnetic field harmonics produced. It has been early developed, using analog integrators, to acquire several points per turn without dead time between consecutive angular positions. The use of a voltage integrator, connected to the measuring rotating coil, makes it possible to exploit the Faraday law eliminating the time dependence of the integration between two consecutive steps. The magnetic flux is therefore described as a function of the angular position, having integrated over a fixed angular interval defined by an external encoder which triggers the integrator. This method prevents also the requirement of a constant rotating speed to have a uniform time interval for each angular position. The plane of the loop of the rotating coil can be oriented in any direction, as in Fig. 1.4, but the two specific configurations of complete "*radial*" coils and complete "*tangential*" are often used for their easy fabrication process, characterization and data analysis. Considering a generic configuration where z_1 and z_2 are the locations of the two sides of the coil and approximating the model to a single turn coil, the magnetic field flux induced during the rotation can be written as:

$$\Psi = LRe\left[\int_{z_1}^{z_2} B(z)dz\right] \tag{1.13}$$

where L is the length of the coil. Using the multipole expansion previously described in Eq. 1.4, the expression can be described directly as a function of the harmonic coefficients.

$$\Psi = LRe\left[\sum_{n=1}^{\infty} \frac{1}{nR_{ref}^{n-1}} C_n(z_2^n - z_1^n)\right] \tag{1.14}$$

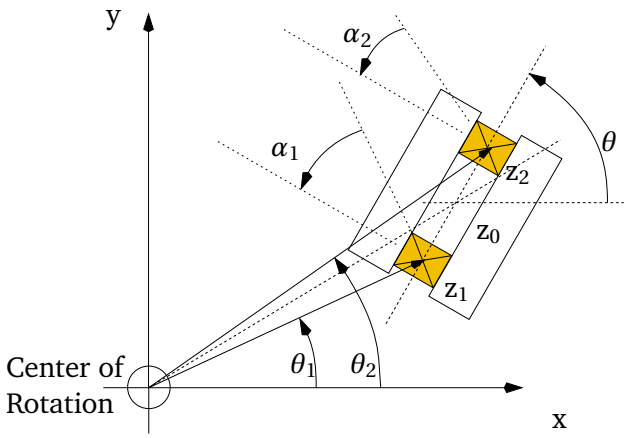

Figure 1.4: *Sketch of the rotating coil during the rotation in the magnet bore at the reference radius. The position of the two cross-sections of the coil is highlighted and tilted with an angle θ to consider the most general configuration of the measurement. Usually, without considering errors of the planarity of the coil, a complete tangential or radial configuration is used for the measurements*

Neglecting possible errors in the rotation velocity or displacement from the ideal circular path of the coil, we can describe the rotation at two fixed radius R_1 and R_2 with initial phases and fixed angular velocity. The last member of the previous equation can be written as:

$$z_2^n - z_1^n = \left(R_2^n e^{in\theta_2} - R_1^n e^{in\theta_1}\right) e^{in\theta} = \left(R_2^n e^{in\frac{\Delta\theta}{2}} - R_1^n e^{-in\frac{\Delta\theta}{2}}\right) e^{in\theta_0} e^{in\theta} \tag{1.15}$$

where we defined the initial phase θ_0 as an average of the two initial phases and the phase difference $\Delta\theta$ between θ_2 and θ_1. Compacting the flux expression by collecting the dependency from the coil geometry parameters in a single complex coefficient χ_n as:

$$\Psi(\theta) = LRe\left[\sum_{n=1}^{\infty} \frac{\chi_n}{nR_{ref}^{n-1}} C_n e^{in\theta}\right] \tag{1.16}$$

$$\chi_n = \left(R_2^n e^{in\frac{\Delta\theta}{2}} - R_1^n e^{-in\frac{\Delta\theta}{2}}\right) e^{in\theta_0} \tag{1.17}$$

The introduced complex parameters χ_n are called geometrical factors and are related to the sensitivity of the coil ruled by the transversal dimensions of the turns in the cross-section plane of the rotating coil. The value of the magnetic flux here described is sampled by the rotating coil as a function of the rotation angle in a discrete N points series during the single turn. We can therefore indicate as ψ_k each single sampled flux. To retrieve the harmonic

coefficients a Discrete Fourier Transform (DFT) is operated on the sampled flux according to Eq. 1.18.

$$\Psi_n = \sum_{k=1}^{N} \psi_k e^{-2\pi(n-1)\frac{(k-1)}{N}} \quad \text{with} \quad n = 1...N \tag{1.18}$$

The DFT complex coefficients Ψ_n can be correlated with the field harmonic coefficients C_n. The relation between the two types of coefficients, for an even number of points and the simplified model of a single turn coil, is reported in Eq. 1.19.

$$C_n = \frac{2}{N}\frac{1}{L}\frac{nR_{ref}^{(n-1)}}{\chi_n}\Psi_{n+1} \quad \text{with} \quad n = 1...\frac{N}{2} \tag{1.19}$$

The presented result is only valid for a single turn model for a rotating coil. In practice a single rotating coil is composed of N_t turns stacked on each other in different layers or wounded side by side. The presented process for the calculation of the harmonic coefficients can be also done for the upgraded multi-turns rotating coil model, leading to a slightly different equation:

$$C_n = \frac{2}{N}\frac{R_{ref}^{(n-1)}}{k_n}\Psi_{n+1} \quad \text{with} \quad n = 1...\frac{N}{2} \tag{1.20}$$

Each of the new coefficients k_n is the complex coil sensitivity factor for the n^{th} magnetic field harmonic. They are proportional to the coil geometric factors χ_n previously described and are generally calculated during the calibration process of the rotating coil shaft. In the case of a perfect radial or tangential coil, the sensitivity factors reduce to a pure real or imaginary number. For a perfect radial coil the sensitivity is equal to:

$$k_n^{radial} = \frac{N_t L}{n}\left(R_2^n - R_1^n\right) \tag{1.21}$$

where we set the initial phase $\theta_0 = 0$ and R_1 and R_2 the internal and external radius of the coil. If we consider a pure tangential coil we can describe the sensitivity factors as function of the middle point radius from the central rotation axis and the coil aperture defined by the variable $\Delta\theta$.

$$k_n^{tangential} = \frac{2iN_t L}{n}R^n \sin\left(\frac{n\Delta\theta}{2}\right) \tag{1.22}$$

A linear combination of two to five rotating coils, instead of using a single one at a fixed radius, can be used to improve the accuracy of the measurements for n>1.

1.5.1 Compensation Scheme

Generally, a rotating coil system is composed of 3 or 5 rotating coils at the same time and centered in the same reference system of the magnetic field measurement shaft. The exact position of the winding of every single coil has to be calibrated to have the best accuracy during the measurement of the magnetic field. The combination of the signal of one or more coils, at different radius, can be used to further increase the accuracy of the measurement. Generally, like in the magnetic field measurement system installed at LASA for the characterization of the HO corrector magnets, two raw signals are obtained from the combination of 5 symmetrical coils (Coil A, Coil B, Coil C, Coil D, Coil E).

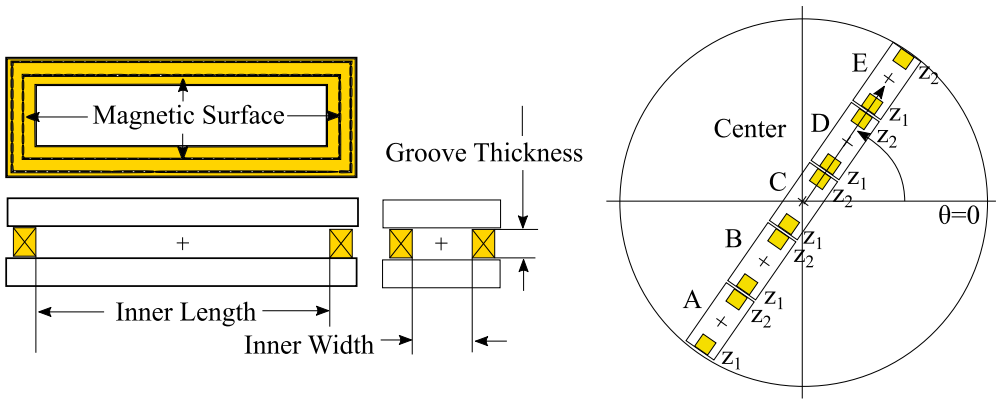

Figure 1.5: *Graphic representation of the geometric parameters of a single rotating coil useful to calculate the single sensitivity factor, (left). The yellow details describe the paths of the winding which has to be precisely calibrated during the preparation of the rotating coil shaft. A scheme of the 5 coils used to fully characterize a magnetic field is reported here showing the location of each single rotating coil center and the position of every single winding, (right). The rotating coil here reported is a radial design used for example in the magnetic measurement system for the high order corrector magnets studied in this thesis.*

The first signal is composed of the raw electromagnetic induction voltage induced in the main external coil (Coil A) and is used to evaluate the main component of the generated magnetic field inside the superconducting magnet. Indeed, the external coil is the most sensitive because its located at a higher reference radius and the magnetic field produced increases with the distance from the central rotational axis of the magnet for each magnetic field order greater than the dipole one. The second signal is obtained through a particular combination of the rotating coils and it aims to suppress the principal magnetic field harmonics to increase the sensibility to the imperfection of the generated magnetic field. Knowing for example that a dipole magnet produces a uniform magnetic field inside the bore, the subtraction of the central rotating

coil (Coil C) from the external rotating coil (Coil A) signal will cancel the main dipole harmonic without affecting the higher harmonic orders. To retrieve the magnetic field harmonics from the DFT (Discrete Fourier Transform) of the induced voltage on the rotating coil, the sensitivity factor could be combined with the same scheme of the coils signals. To compensate for the quadrupolar magnetic field, the combination of 4 rotating coils can be exploited using the following scheme:

$$\text{Compensation:} \quad A-B-C+D \qquad k_n^{cmp} = k_n^A - k_n^B - k_n^C + k_n^D \tag{1.23}$$

Using an amplifier, each coil signal can be also multiplied by a gain factor to create additional compensation schemes to cancel higher magnetic field harmonic orders. Considering also the gain factors, the total sensitivity factor which has to be used to calculate the magnetic field harmonics can be described by the Eq. 1.24.

$$k_n^{cmp} = g_A k_n^A + g_B k_n^B + g_C k_n^C + g_D k_n^D + g_E k_n^E \tag{1.24}$$

1.5.2 Center Localization and Feed Down Correction

One of the main problems with the rotating coil system is the localization of the central rotational axis of the magnet and the alignment of the rotating shaft referee frame with it. The misalignment between the rotating coil shaft and the magnet understudy could create additional magnetic field harmonics which do not corresponds with the real produced field quality of the magnet. If the reference system of the magnet, see Fig. 1.6, is translated by a distance in the **z** complex plane, the harmonic coefficients of the magnetic field quality could be described as a function of the real harmonics calculated in the centered reference system using the Eq. 1.25.

$$\mathbf{C}_n^{'} = B_n^{'} + i A_n^{'} = \sum_{k=n}^{\infty} \left(\frac{(k-1)!}{(n-1)!(k-n)!} \right) \mathbf{C}_k \left(\frac{\Delta \mathbf{z}}{R_{ref}} \right)^{k-n} \tag{1.25}$$

Moreover, the translated magnet reference system could also be rotated to the axis of the measuring reference system imposing a phase for the magnetic field harmonics. The phase of each single harmonic is not equal to the rotation between the two reference systems but is a function also of the rotational order calculated. The harmonic coefficients, rotated by an angle θ can be written in the non rotated reference system according to the equation:

$$\mathbf{C}_n^{'} = B_n^{'} + i A_n^{'} = \mathbf{C}_n e^{in\theta} \tag{1.26}$$

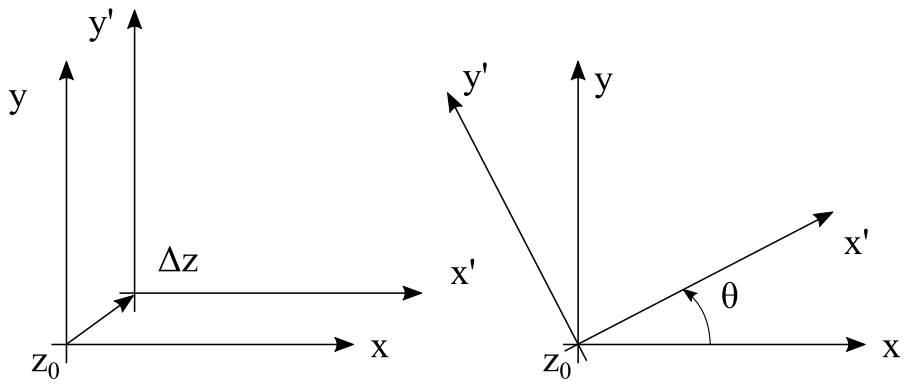

Figure 1.6: *Sketch of the possible translation (left) and rotation (right) between the reference system frame of the magnet and the one used by the rotating coils for the analysis of the produced magnetic field quality*

To evaluate the exact position and rotation of the center of the magnet, a possible solution is to compute the value of $\Delta\mathbf{z}$ which cancel non-allowed magnetic field harmonics in the measured spectrum of the field quality. The calculation of the magnet center has to be different for high values of rotational order and low values like for the dipoles. In a dipolar magnetic field, much rotational order of harmonics is allowed by the symmetries of the magnet. Therefore, to evaluate the magnet center, very high values of not allowed magnetic field harmonics have to be considered. A common procedure is to calculate the value of $\Delta\mathbf{z}$ which cancels the fields harmonics greater than the 8th order up to the 15th order and which minimize the value of non allowed harmonics in the central reference frame. A different approach is used when a 2m-poles magnet is considered. If the two reference systems are not centered, the most sensitive magnetic field harmonics, affected by this error, is the 2(m-1)-pole harmonic. For example, a shift in one direction on a quadrupolar magnetic field can be described by an additional dipolar magnetic field superimposed on the produced one which is measured by the rotating coil system. The definition of the $\Delta\mathbf{z}$ shift that has to be imposed on the rotating coil reference system, *feed-down correction*, is, therefore, the value that satisfies the following equation:

$$\Delta\mathbf{z} = -\frac{R_{ref}}{m-1}\frac{\mathbf{C}_{m-1}}{\mathbf{C}_m} \tag{1.27}$$

Using the result obtained from this equation we can therefore obtain the real magnetic field quality produced by the magnet by replacing the value of the translation into the Eq. 1.25.

Chapter 2
High Order Corrector Magnets

2.1 Introduction

The Standard Model of particle physics has been completed recently by the discovery of the Higgs Boson in 2012, Nobel Prize for Peter Higgs [6], at the Large Hadron Collider, LHC. Thanks to the huge amount of statistic obtained during the different collision run of the machine, particle scientists have obtained the necessary amount of data to determine the statistic significance at 5 σ of the discovery and determine the mass of this particle, compatible with a value between 125 and 127 GeV/c^2, [7] [8]. To evaluate and characterize all the physical properties of this particle, like its charge, the spin and all its interactions with the other known particles, the data acquired from the Run2 of LHC, ended between 2018 and 2019, are currently being analyzed. It is expected to achieve a level of accuracy never obtained before allowing to evaluate the existence possibility and indirect effects of physics beyond the standard model over the yet discovered ones. To further increase the potential of discovery and allow the study of a new extended Particle Physics Model over the SM, a new upgrade project called High Luminosity LHC [9], HL-LHC, has been studied and developed in the last few years. The principal aim of this upgrade is to achieve an instantaneous luminosity larger than the LHC nominal value by a factor of five increasing the data sample provided to experiments by an order of magnitude. The upgraded LHC will deliver proton-proton collisions at an energy of $\sqrt{s}$=14 TeV in the center of mass reference frame with an instantaneous luminosity of 6.5 $10^{34}cm^{-2}s^{-1}$ and integrated luminosity of 3000 fb^{-1}. The development of the project depends on several technological innovations, [10]. New superconducting magnets will be implemented in the beamline. Near the Interaction Points, IP, new Inner Triplet Magnets, based on Nb_3Sn superconductors, will be installed to reduce the transversal dimension of the beam during the crossing. A higher value of luminosity, for the magnets and the electronic components used to focus the beam, translate into a higher dose of radiation of about 30 MGy, which can bring to the damage and faults of the material. The reduction of the transversal beam sizes at the IP corresponds also to an increase of them inside the bore of the inner triplet, an increased crossing angle and dimensions of the beam separation main dipole

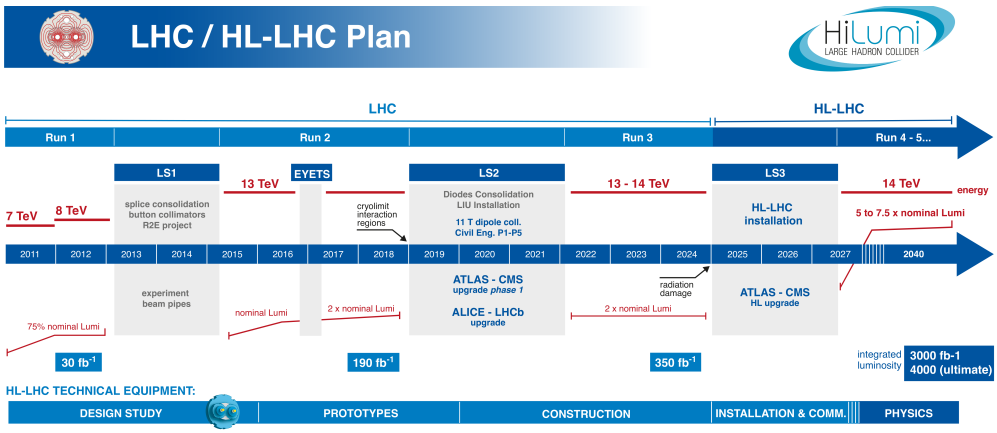

Figure 2.1: *Time table of the HL-LHC project upgrade with details on the beam energy and the shutdowns of the collider. Both the experiment upgrade and magnets installation are enlighted showing the variation of the beam energy in the center of mass reference frame expected and the increasing of the luminosity during the future run.*

before the interaction. The transversal sizes of the beam in a particle accelerator can be generally described by the β function. This parameter is linked to the actual beam sizes by the equation $\sigma(s) = \sqrt{\epsilon\beta(s)}$ where the s parameter identify the position along the beam direction, $\sigma(s)$ is used to measured the width of the supposed Gaussian beam shape in the transversal direction and ϵ identifies the RMS geometrical beam emittance which is a constant value along the beam trajectory where no linear acceleration is applied to the particles. At the interaction point of a particle collider, the β function assumes its minimum value called β^* while for all the interaction region the beam transversal sizes can be approximated by the expression $\beta(z) = \beta^* + z^2/\beta^*$ where z is the distance from the particles interaction point. From this expression it is clear that with smaller sizes of the beam in the interaction point, the transversal dimensions of the beam tube increase rapidly immediately before and after the beam crossing where the focusing magnets, also called low-β^* quadrupole magnets, are installed in the accelerator lattice. The increased number of interactions per second will cause also a higher pile-up and events seen by the detectors. To withstand the radiation dose of this new number of events, components of the detectors will be substituted and upgraded to achieve better performances and reconstruction of the particles generated after the collisions. The currently available collimation system, designed for the LHC nominal energy and beam intensity will be substituted and optimized to cope with the expected HL-LHC beam losses. To allow the installation of the new collimation system, the old Nb-Ti 8.33 T dipole, which is 15 m long, will be replaced by an 11 Nb_3Sn T main dipole with a length of approximately 11 m to provide the same bending

strength, [11]. To increase the intervention flexibility the cryogenic plant in the IR will be completely redesigned. The new cryogenic system will separate the RF cavities from the superconducting magnets avoiding the warm-up of the entire arc in case of faults or damages and increasing the overall efficiency. A new type of superconducting RF cavities, called crab cavities, will be installed before the IPs and used to rotate the counter-rotating bunches increasing their overlap during the crossing and which will enhance the collision probability of the protons. New MgB_2 low losses and high-power superconducting link lines will be implemented to simplify the access to the power supply of a portion of the interaction point machines. New diagnostic and advanced modeling will be necessary to assure machine protection and deal with the increased energy of the collider and fully exploit the physics potential of the upgrade.

2.2 MAGIX PROJECT AND INFN-CERN COLLABORATION

The HL-LHC project, as already described, will completely modify the layout of the superconducting magnets of the near IP regions besides the experiments. Many different types of magnets are required to precisely provide the exact amount of beam focusing and stability before the collision. Even if the requirements, on the magnetic field quality of the Inner Triplet Magnets (Q1, Q2, Q3) and the separation dipole magnet (D1), are very tight [12], a dedicated series of corrector magnets are required to fine-tuning the performances of the layout of the whole magnets. According to the required multi-order of the magnetic field needed for the correction, 5 different types of High Order Corrector Magnets, starting from the skew quadrupole up to the 6^{th} order of magnetic field harmonic, have been studied and built by INFN-LASA with feedback from the collaboration with CERN, (Agreement HL-LHC KE2291). All 5 prototypes have been already built and tested at LASA at an operational temperature of 4.2 K and 2.2 K in a vertical cryostat. All the magnets have reached the required specification of energization and quench protection performances allowing the starting of the production series of all the 54 series magnets within a new collaboration between CERN, INFN, and the industry, (Agreement HL-LHC K3085). The magnetic field quality of the different prototypes has been measured at CERN in the SM18 laboratory during the vertical cryogenic tests used also to check the performances of the magnets. The only prototype, which magnetic field has been characterized at INFN-LASA is the skew quadrupole MQSXFP1. In the second agreement, the INFN has been in charge of qualify and control all the production steps of the magnet series production. The different magnets of the series are built and assembled at Saes Real Vacuum (SRV), Italy. All the magnets are then tested and qualified at INFN LASA laboratory in a vertical cryostat to evaluate the powering performances and the produced magnetic field quality. Finally, the magnets are

shipped to CERN which is responsible for the integration in the cold mass of the Interaction Region corrector package. The first four magnets of the series have been already tested at LASA with positive feedback on their performances and the second half of the first batch of the production has been already built and assembled at SRV. The magnets have been delivered at LASA at the end of 2020 and the first vertical cryogenic full test is expected at the beginning of February 2021.

2.3 Electromagnetic and Mechanical Design

As mentioned above, the electromagnetic and mechanical design of all the High Order Corrector magnets has been developed by INFN-LASA superconducting magnet group. The requirements for the corrector package performances have been fixed by the expected quality of the quadrupole triplet and the available mechanical space for the integration in the package layout. All the required magnetic field harmonics have been associated with a single magnet to separate the different contributions avoiding nested magnet solutions and allowing more freedom in the parameters operational space. The corrector package is composed of the MCBXF orbit corrector magnet developed by CIEMAT, [13], and 9 High Order corrector magnets, two magnets for each order to provide the normal and skew component except for the quadrupole which is only skew.

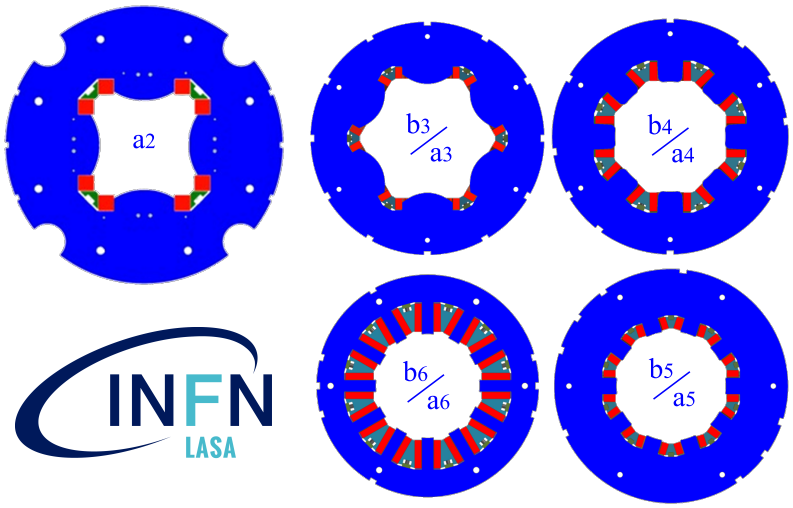

Figure 2.2: *Cross section of all the HO Corrector Magnets with the corresponding magnetic field main harmonic produced. The normal and skew configurations of the magnet have the same configuration except for the skew quadrupole, which is not required in the normal configuration, and the normal dodecapole which has a longer mechanical length than the skew dodecapole.*

The main expected magnetic field error of the main triplet magnets is represented by the skew magnetic field quadrupolar component which would cause the divergence of the particles and the beam loss if not properly compensated. Both the normal and skew contributions of the corrector package are used to correct energy dependent errors of the quadrupolar magnetic fields. The spread in energy and momentum of the accelerated particle, which are focused by the inner triplet magnets, causes a variation of the focal length of the quadrupole magnets like, in optic, light rays of different wavelength are not refracted in the same direction which depends by the material refraction index. This non linear behavior is usually called as "chromaticity" effect and is always present in particle accelerator with the use of focusing elements. The octupolar magnets are used in particle accelerators to correct beam interaction effects with the accelerator elements like space charge effects and in particular are used to obtain the Landau damping of the particles while decapole and dodecapole magnets are used to correct principally the imperfections of the first allowed harmonics of dipoles and quadrupole magnets. All these different magnet types are especially needed in the IP region due to the higher transversal dimensions of the beam, compared to the sizes in the collider arc, which enhance the effects of the magnets field errors on the beam dynamic. Due to the small available space for the insertion of the magnets, the superferric design has been chosen to obtain very short ends length and a simplified construction process of the racetrack superconducting coils. The magnetic field quality produced by this design is mainly ruled by the iron pole shape which has to be precisely produced with low mechanical tolerances. The particular shape of the iron poles follows a slightly modified equation of the perfect n-order equipotential surface which produces a perfect n-order multipolar magnetic field. This correction has been introduced to compensate for the finite dimensions of the poles in the transversal dimensions and the harmonic contributions of the superconducting coils cross-sections. All the magnets have a bore aperture diameter of ϕ =150 mm and the poles are excited by superconducting NbTi racetrack coils which flux is closed on the external iron yoke increasing the focusing of the produced magnetic field. The final operational temperature in the accelerator lattice is 1.9 K and the superconducting coils are directly in contact with the superfluid liquid helium allowing higher heat exchange to increase the stability in the superconductor state. All the materials used for the construction of the magnets have to withstand the expected amount of radiation of 25 MGy. The body of the whole magnet is composed of pure ARMCO iron laminations, produced by AK Steel, which are precisely machined by electro-erosion to assure the precision of the pole profiles within the requested tolerance of +/- 0.03 mm. This type of iron has been several times used for the construction of particle accelerator magnets thanks to its high purity and magnetic performances like the low values of residual magnetization

TABLE 2.1.
REVIEW OF PERFORMANCES AND OPERATIONAL PARAMETERS OF ALL THE HO CORRECTOR MAGNETS

Parameter	Units	MQSXF	MCSXF/MCSSXF	MCOXF/MCOSXF	MCDXF/MCDSXF	MCTXF	MCTSXF
Order		2	3	4	5	6	6
Aperture	[mm]	150	150	150	150	150	150
Integrated Strength	[Tm]	0.700	0.095	0.069	0.037	0.086	0.017
Coil Length	[mm]	457	192	172	172	498	123
Magnet Length	[mm]	614	254	233	233	575	200
Magnetic Length	[mm]	401	168	145	145	469	99
Gradient	[T/m^{n-1}]	34.8	224	3680	40480	585600	550400
Number of Apertures		1	1	1	1	1	1
Number of Circuits		1	2	2	2	1	1
Units Needed		4	8	8	8	4	4
Spares		2	4	4	4	2	2
Cable Data							
Strand Diameter	[mm]	0.7	0.5	0.5	0.5	0.5	0.5
Insulation Thickness	[mm]	0.07	0.07	0.07	0.07	0.07	0.07
Alpha (Cu/Not Cu)		2.1	2.1	2.1	2.1	2.1	2.1
Coil Design							
Material		Nb-Ti	Nb-Ti	Nb-Ti	Nb-Ti	Nb-Ti	Nb-Ti
Nturns/Pole		754	288	372	228	432	432
Cable Length/Pole	[m]	1230	104	105	59	439	112
Operational Parameters							
Coil Peak Field	[T]	3.6	2.23	2.09	1.63	1.57	1.5
Temperature	[K]	1.9	1.9	1.9	1.9	1.9	1.9
Nominal Current	[A]	174	99	102	92	85	84
Overall Current Density	[A/mm^2]	314	308	317	286	264	261
Loadline		44%	31%	31%	26%	27%	27%
L_{diff} @ I_{nom}	[mH]	1530	213	220	120	805	177
Stored Energy	[kJ]	30.8	1.72	1.55	0.67	3.6	0.73

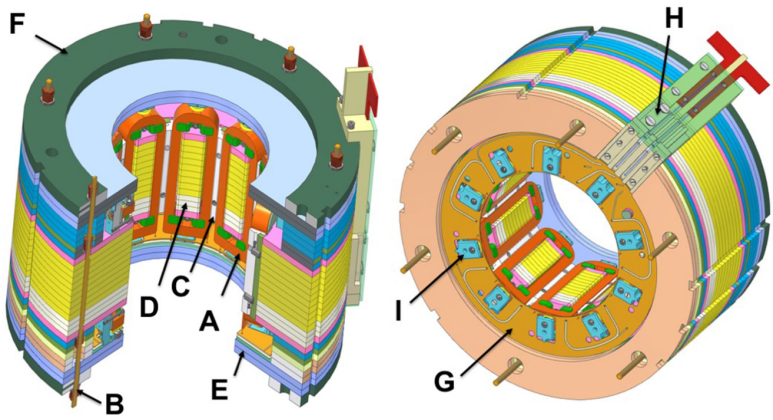

Figure 2.3: *Picture of the MCDXFP1 (first decapole prototype) corrector magnet cad model. The model is cutted, (left), to observe the internal side of the iron laminations and the superconducting coils mounted on each pole. The mechanical details are the following: superconducing coils(A), CuBe rods(B), wedges(C), magnetic pole(D), flux return laminations of the end cap(E). Additional details of the connection side are visible in the model, (right): stainless steel closing plate(F), connection board(G), electrical connection box(H), longitudinal plates(I). For more details see [14]*

at cryogenic temperatures. At the two ends of the magnets, closing iron laminations with a larger internal radius, compared to the ones of the magnet core which compose the poles, are used to create the end caps which protect and contain the superconducting coil ends. Additional iron laminations are used to create a closing path for the flux along the axial direction of the magnets. This expedient improves, in general, the performances of the correctors focusing the magnetic field inside the bore of the magnet. All the iron laminations pack is pressed by Cu-Be tie rods which provide also the axial alignment of the magnet. The external side of the iron lamination pack is then closed by stainless steel plates, fixed always through the same rod of the lamination, to create the mechanical interface with the mounting system for the LHC lattice. The external radius of the magnets has been limited to the maximum internal radius of the final configuration cryostat at CERN and different grooves, which are precisely machined on the external radius of the magnets as the iron poles profile, allow for easy and standard installation of the two different operating configurations (normal and skew) assuring precisely alignment of all the magnet. To assure radiation damage resistance of the magnet, the superconducting coils are impregnated with CTD-101K epoxy resin [15] and the insulation layers towards ground have been tested during the prototype construction using both BTS2, by Arisawa industry, and Duratron. Also, the single wire insulation is composed of reinforced S2 glass to prevent any electrical shorts during the

coil energizing. All the coils are mechanically supported by wedges on their long side. During the assembly of the magnets, the wedges are pushed against the coils to provide a preload which compensates the thermal contraction and the Lorentz forces during the cool down and energizing of the magnet. On the shorter side of each superconducting coil, a small plate is used only to fix the vertical position of each coil along the magnet axis. The coils support towards the iron pole is composed of a thin layer of 304/L stainless steel to prevent direct contact between the coil insulation layer and the iron yoke. The connection between every single coil is created in a PCB layer placed on the connection side of the magnet before the end iron laminations. The PCB is composed of insulation disks of Arlon and lamination sheets of copper from which the paths of the connections are created using standard etching techniques. The PCB is insulated from the rest of the magnet using two additional Arlon disks and covered with liquid polyimid to protect the connections. The PCB is then connected, through a hole in the external iron yoke laminations, with the external power lines to energize the magnet. The external connection is composed of two separated standard boxes to avoid connections error during the mounting process in the final configuration at CERN. The first box, designed by INFN, contains the external connection for the powering supply made by two copper plates for the connections with the bus-bars. The second box, designed according to CERN specifications, contains all the voltage taps for the quench detection system and magnet control.

2.3.1 RCSM Design

Thanks to the acquired experience during the electromagnetic and mechanical design of the HO corrector magnets, the INFN-LASA group has also developed, in the INFN-CERN collaboration framework for the HL-LHC upgrade project, a new type of superferric corrector magnet suitable for particle accelerator which uses MgB_2 superconducting wires instead of the conventional LTS superconductors. This new class of superconductor magnet, called Round Coil Superferric Magnet, RCSM, is suitable for strain-sensitive superconductor materials that require high values of bending radius in the winding process of the construction of the superconducting coil. This new design is particularly developed for the construction of arbitrary multipole order magnets. The iron yoke is shaped with an arbitrary number of poles being able to create the desired harmonic component magnetic field using only round superconducting coils connected in anti-series to cancel the solenoidal component. The first idea of the particular design of this superferric magnet has been studied by I. F. Malyshev and V. Kashikhin [16], who also built a quadrupole prototype with HTS tapes working in a persistent current mode operation [17], and optimized by

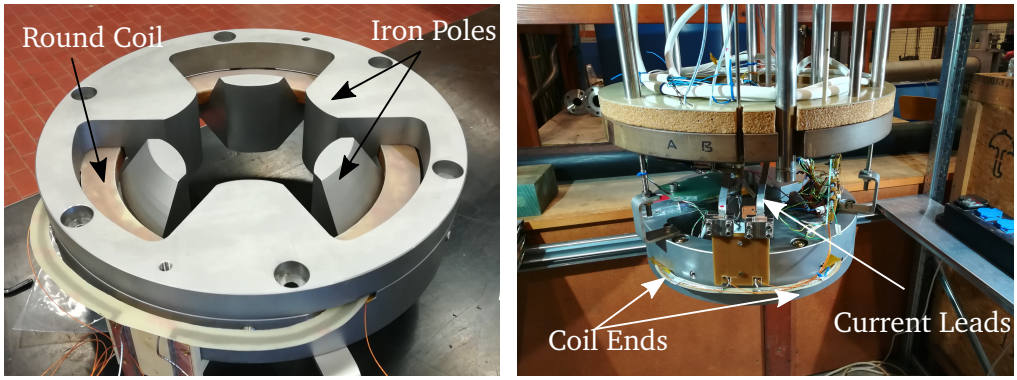

Figure 2.4: *Picture of the first assembled semi-module prototype of the full RCSM magnet. The six alternating iron poles (left) redirect the solenoidal magnetic field, produced by the round superconducting coil, in the magnet trasnversal plane creating the sextupolar harmonic component desired. The magnet has been already testes at LASA at the cryogenic temperature of 4.2 K in the vertical cryostat reaching the 78% of the SSL.*

G. Volpini and J. Rhysti who first tried to use MgB_2 tapes for the coil realization [18]. The ARMCO iron yoke design and coil geometrical dimensions have been optimized to create the first prototype of a sextupole corrector magnet, see Fig. 2.4, with an integrated magnetic field equal to 75% of the classical sextupole HO corrector satisfying the same magnetic field quality required for particle accelerator corrector magnets, [19]. The developed design has a modular configuration allowing to build separately the different parts of the iron yoke which are then assembled with the round superconducting coils. The whole complete magnet is composed of two modules, necessary to provide the required integrated magnetic field, each of them made up of two round coils with their corresponding iron yoke and poles. The first RCSM semi-module has been already built and tested at the LASA department. The magnet design parameters have been reported in Table 2.2. The MgB_2 wires have been insulated with a polyester filament while the ground insulation, performed using BTS2 sheets, and the impregnation process, using the CTD-101K epoxy resin, have been inherited from the HO corrector coil design. Also, the mechanical design of the magnet is very close to the HO corrector design. The two pieces of the iron yoke are centered with an external groove and the rotational alignment of the poles is made by Cu-Be rods which provide also the compression in the axial direction to the magnet. The mechanical support of the coil is provided in the axial direction by the two sides of the iron poles connections and in the radial direction by spring washers to counter react the Lorentz Forces during coil powering. The superconducting coil has been firstly successfully tested without the iron yoke and poles to verify the performances of the spring

TABLE 2.2.
PARAMETERS OF THE RCSM MAGNET AND MgB_2 WIRE

Magnet Parameters		Coil and Wire Parameters	
Nominal Current	148.81 A	Turns Number	336
Ultimate Current	161 A	Layers Number	28
Magnet SSL @ 4.2 K	300 A	Radial Thickness	32.3 mm
Coil SSL @ 4.2 K	333 A	Axial Thickness	18 mm
Stored Energy @ I_{nom}	1.1 kJ	Internal Radius	133 mm
Stored Energy @ I_{ult}	1.23 kJ	Radial Insulation	0.15 mm
Inductance @ low-I	375 mH	Axial Insulation	1.2 mm
Inductance @ high-I	73 mH	Wire Diameter	1±0.01 mm
Two Modules Length	360 mm	Filaments	37
Integrated Field	67 Tmm	Filament Diameter	55 μm

Wire Composition				
MgB_2	Monel	Niobium	Nickel	Copper
11.5%	46%	14.5%	14%	14%

washer system [20]. A second test of the whole first semi-module configuration have been made at LASA vertical test station at 4.2 K. The nominal and ultimate current values have been reached without any quench and the powering has been successfully performed up to the current limit of 236 A which corresponds to the 78% of the magnet loadline. The detailed analysis of the magnet performance is not reported here because this novel type of magnet, on which optimization I performed my Master degree thesis and followed the construction process, during my Ph.D., with electromagnetic 3D simulations and quench analysis of the measured signals, is not the main argument of this thesis. However, the analysis has been reported in [21] together with the comparison between the experimental data and magnet simulations finding a very good agreement in the predicted behavior. The magnet is scheduled to be upgraded with a second semi-module to further evaluate the performances and complete the characterization with the analysis of the magnetic field quality produced by a complete module.

2.4 QUALITY CHECKING

The construction process of all the HO corrector prototypes and magnets series has to be carefully checked to detect possible non-compliance with the technical specifications of the magnets. For the mechanical quality, the dimensions of all the produced parts of a magnet have to be measured and have to satisfy the mechanical tolerances imposed by the design. All the iron laminations are carefully inspected and measured by a numerically controlled touch probe for

the detection of bumps in the pole profiles or the external grooves. During the assembly of the iron laminations the length of the pole, derived from the thickness of each single iron lamination and their mechanical tolerances, is controlled and verified. An additional iron lamination can be used to compensate for small variations of this length to provide the right amount of packing factor in the magnet. Dimensional inspections are also performed on all the superconducting impregnated coils to assure that no mechanical interferences during the assembly would damage the coil or the iron poles. All the coils are checked for cracks and delaminations of the external insulation layers and their quality has to be firstly approved by the S.R.V. industry and then by INFN. The number of the turn of every single coil is also checked. During the prototype development, this number has been controlled by measuring the total wire DC resistance and compared to the resistance of the other identical coils. However, to detect possible counting errors of the turn number, the resistance has to be measured with high precision of 1 part over 1000 due to the high number of turns in the coils (typically from 200 to more than 400). A calibrated current is applied in each single coil and the voltage drop is measured using a 4 wire method to retrieve the value of the total resistance, [22]. During the measurements, the small variations of the temperature inside the coils, which would affect the precision causing drift of the total resistance, are compensated by performing multiple simultaneous tests on the referee coil and the inspected one. Recently, for the production of the magnet series, a new method for the calibration of the coil turns number has been developed at LASA, [23]. Two coils of the same type of magnet are powered in anti-series to produce opposite magnetic fluxes in a single iron core. A pickup coil, winded on the iron core, is used to detect the variation of magnetic flux, and therefore induced current variation, which will be created by a difference in the number of turns in the two inspected coils. This method has higher accuracy than the previous one and is capable of evaluating variations of one single turn with high reliability. All the coils and the PCB connections have to withstand the electrical quality tests. The insulation of the coils and the PCB has to be tested to verify their integrity before and after the final assembly in the magnet. Both the coil to ground and turn to turn insulation are tested and, according to CERN requirements, a 2 kV DC voltage is applied between the coil and the ground measuring the leakage current. The single coil is considered suitable to be installed in the magnet if the leakage current is lower than 10 μA.

2.5 Magnetic Measurement Test Station at LASA

As described previously, the INFN research group has been in charge of the development of the High Order corrector magnets for the High Luminosity LHC update program. Together with the design and construction of the magnets,

the LASA laboratory has been selected to perform the cryogenic test of both the developed prototypes, tested also at CERN SM18 after the thermal cycle to certificate the performances, and all the magnet series production. The first part of the cryogenic test, performed at LASA, is composed of the powering of each single magnet up to its nominal current, at first, and then up to the ultimate current. During the ramp-up of the current, the magnet could experience some training which triggers the quench protection system forcing the magnet to discharge on an external dumping resistance, in case of the MQSXF magnet, or on the only internal developed resistance in case of all the other HO corrector magnets. After the establishment of the magnet stability, a thermal cycle is performed and the magnet is again cooled-down to cryogenic temperature for a second powering after the thermal cycle. The magnet has to reach the nominal current with a maximum of one single quench and has to perform at nominal current for the entire 1-hour stability test without any quench events. After the powering test, a complete magnetic measurement test can be performed to measure the field quality produced. To fully characterize the magnet, as we can see from Fig. 2.5, two magnetization cycles are performed to set the magnetization level of the magnet and the stair-step cycle used to measure the field quality at different current values. All the powering cycles can be fully automatized while the rotating coil measurement system continues to acquire the magnetic field produced. The switching from positive to negative current

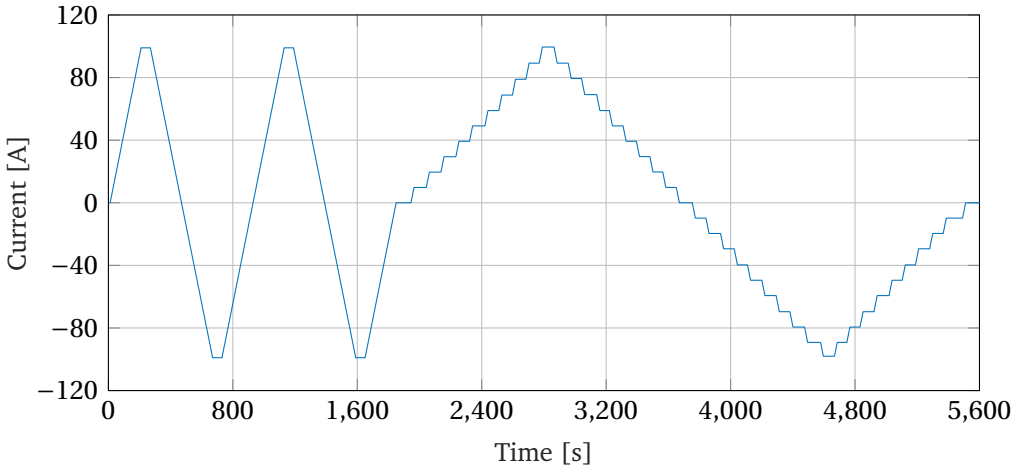

Figure 2.5: *Example of magnetic measurement powering cycle of the magnet. The first two complete cycles are used to fix the iron magnetization level at the future working one when the magnet will be installed in the beamline. The stair steps cycle, instead, is used to evaluate, at different levels of current, the magnetic field quality and magnet transfer function.*

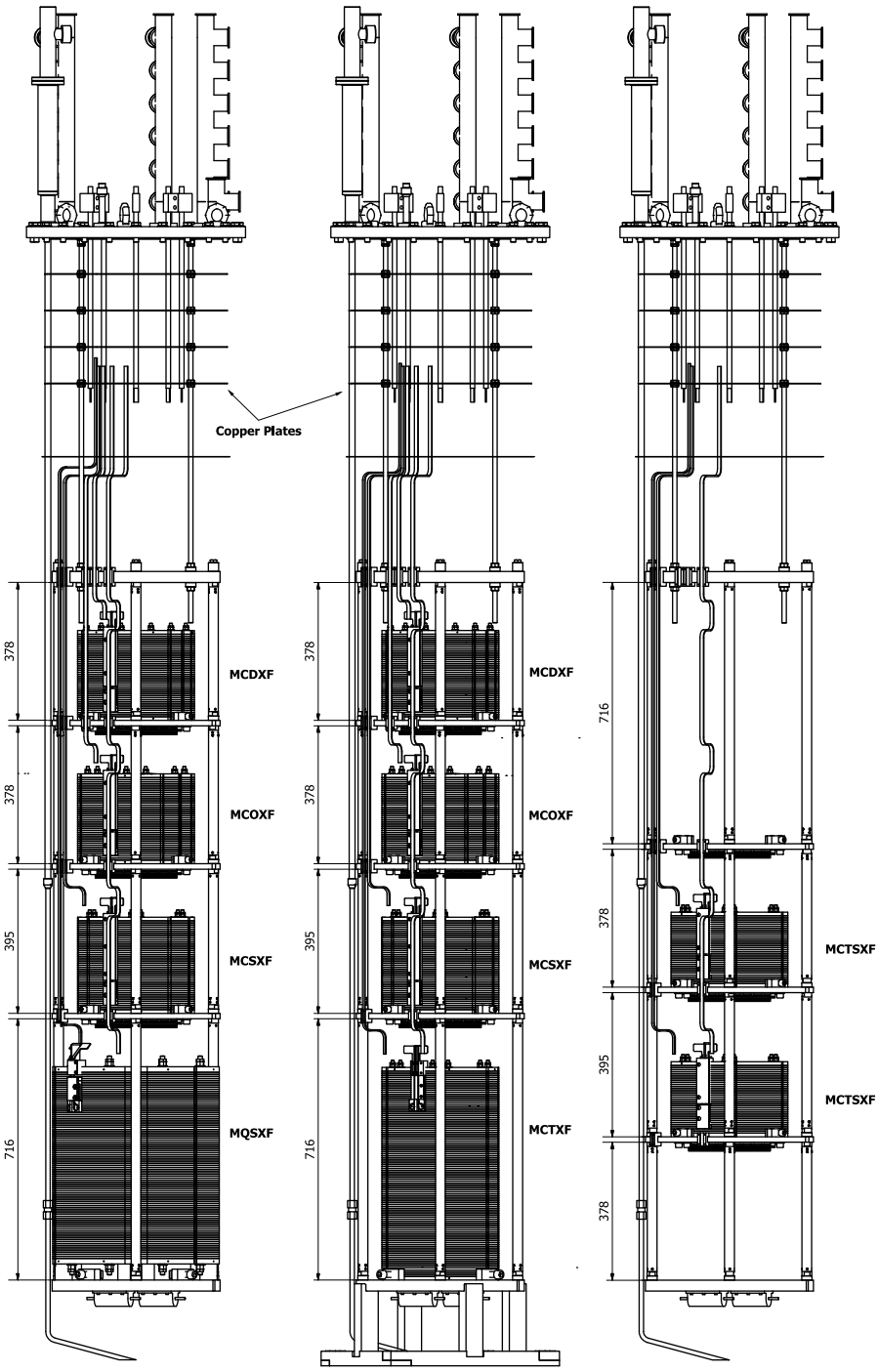

Figure 2.6: *Different configurations of the vertical magnets stack for the cryogenic tests performed at LASA. The longer magnets, MCTXF and MQSXF, are placed at the bottom of the stack while, according to necessity, the position of the shorter magnets could be exchanged.*

has been incorporated in the control system of the power converter used at LASA and a PID controller adopted to fine-tuning the amount of current that flows in the magnet. The current during the plateau has to be stable within 10^{-3} to avoid oscillation of the magnetic field produced during a single turn of the rotating coil and this limit is fixed by the needed accuracy in the measured magnetic field quality measured in units of the main produced field. To speed up the test of all the magnet series, three stacked configurations of the magnet, inside the vertical cryostat, have been designed to be used at LASA, see Fig. 2.6. With this configuration, a common line is used for all the magnets and four different power lines are used one at a time for the magnets powering. The magnetic measurements system, used during the tests performed at LASA, has been developed in collaboration with CERN which has been in charge of designing the rotating coils and the data acquisition system together with the motor powering unit. The data acquisition system hardware is composed of a patch panel, connected to the voltage taps of the rotating coils, 2 Fast Digital Integrators which integrates the signal over the angular steps of the encoder

Figure 2.7: *Data acquisition systems and motor unit for the magnetic field measurements of the HO corrector magnets. Acquisition rack which contains the patch panel, the FDIs and the encoder and motor control boards all connected to the main computer for the user interface, (left). Motor Unit which rotates the PCB coil in the vertical cryostat. The motor contains also the encoder for the trigger of the FDIs at fixed angular positions, (right).*

unit, the encoder which is synchronized with the digital integrators, and the motor unit which control the rotation speed, see Fig. 2.7. The integration of all the hardware systems is performed with the FFMM (Flexible Framework for Magnetic Measurements) framework which performs also the direct analysis of the acquired signal and calculates the magnet field quality. The patch panel has 30 multiple connections and redundancies allowing the hardware combination of different signals to remove possible noise, defects, or compensate undesired harmonics in the rotation. Two different types of signal compensation schemes are used for the HO corrector magnets. For the MQSXF magnet, a quadrupolar scheme is used to compensate the dipole and quadrupole harmonic, allowing the signal to be composed by all the higher magnetic field harmonics only. To obtain the main field harmonic produced by the magnet, a separate voltage tap of the external coil, which is the most sensitive as it is located at a higher radius value, is sampled during the rotation and analyzed as described in Section 1.5. The INFN, within this Ph.D. study and research, has been in charge of the integration of the CERN designed system with the mechanical structure of the vertical cryostat already used at LASA. To fit the rotating coil inside the vertical cryostat a mechanical mounting system has been developed. The rotating shaft has been fixed throw stainless steel flange which shrinks around the top and bottom of the external rotating coil tube and assures the correct centering inside the mechanical structure which supports the magnets. The rotating coil shaft is connected throw a junction carter to the top connection shaft. The connection between cryogenic temperature and room one is made by a small ball bearing sealing element designed from the one used at SM18 at CERN for the vertical cryostats. To fit the HO corrector magnet test configuration inside the vertical cryostat and cover the three possible configurations, previously described, a new rotating coil has been developed by CERN magnetic measurement department and shipped at LASA at the end of 2020, see Fig. 2.8. The new rotating coil shaft is composed of a G10 T-beam internal supporting system with 5 slots for the installation of the rotating coil PCBs. Its diameter is equal to 130 mm and has a measuring reference radius of 50 mm for the characterization of the HO corrector magnets. However, to configure the all magnetic measurement system and verify the integration with the INFN mechanical structure, a temporary rotating shaft has been borrowed to LASA together with the CERN equipment. The temporary shaft, see Fig. 2.9, is composed of a single 1.5 m external carbon fiber shell which contains a 1.311 m long PCB with the 5 typical symmetrical coils for the sample of the magnetic field at different reference radii. The signal acquired from the external coil of this rotating shaft is sampled at a reference radius of 43 mm, due to the width of the shaft equal to 90 mm, which is lower than the 50 mm reference radius of all the High Order corrector magnets. Therefore, the sensitivity of this shaft to the magnetic field produced is expected to be lower than the new rotating coil.

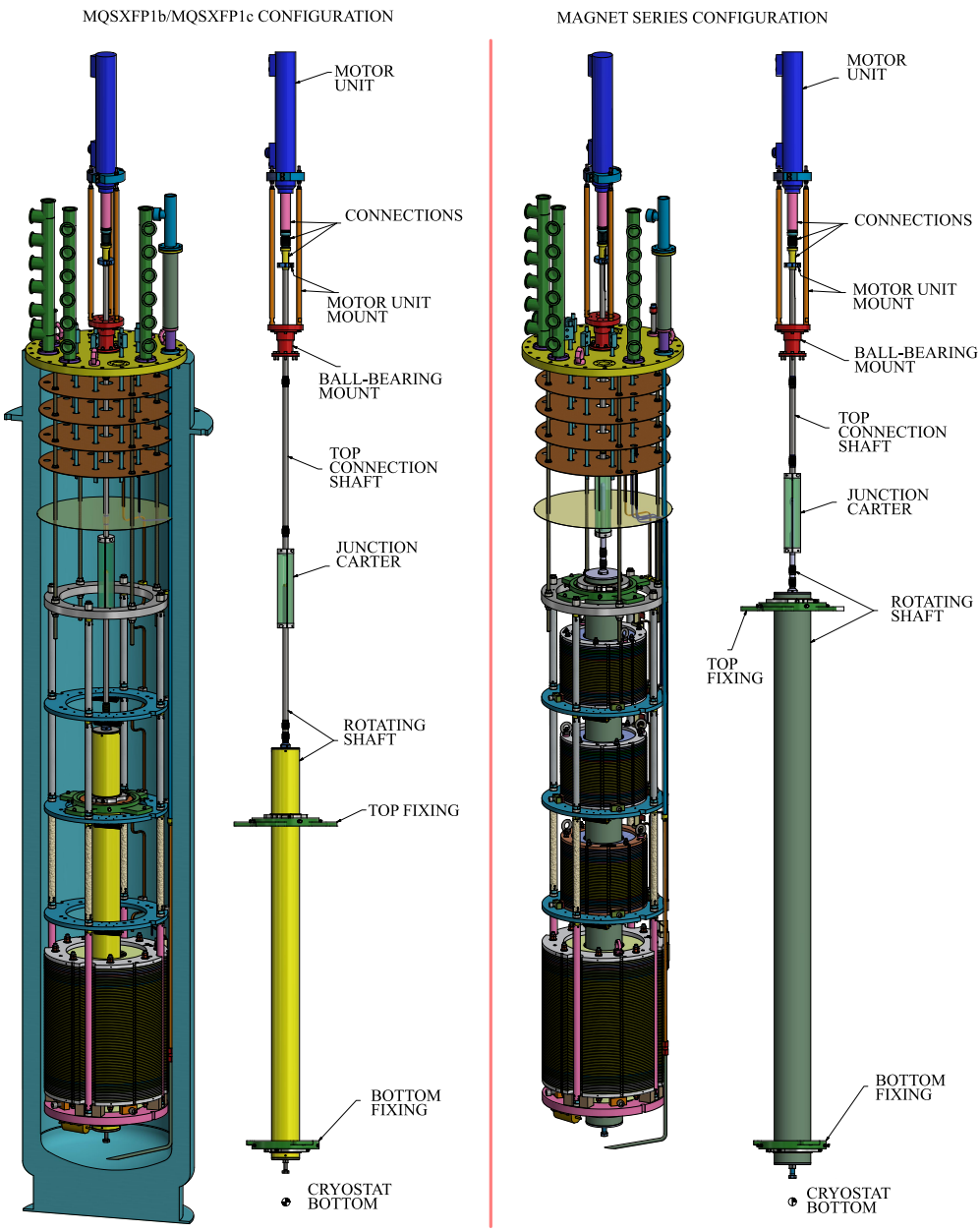

Figure 2.8: *Two different configurations of the rotating coil shaft system are displayed. The temporary shaft used for the MQSXFP1b test and the MQSXFP1c-MCDXF01 assembly test is a CERN shaft developed with a single 1.3 m long PCB with 5 coils, (left). The final shaft is designed to fit the magnet configuration for the vertical cryogenic tests,(right). The probe consists of 5 equal PCB each composed of 5 symmetrical coils at the different radius. The first three PCBs from the top are dedicated to the first three short magnets while the other two PCBs have to be sampled together to acquire the magnetic field of the longer magnets (quadrupole and dodecapole).*

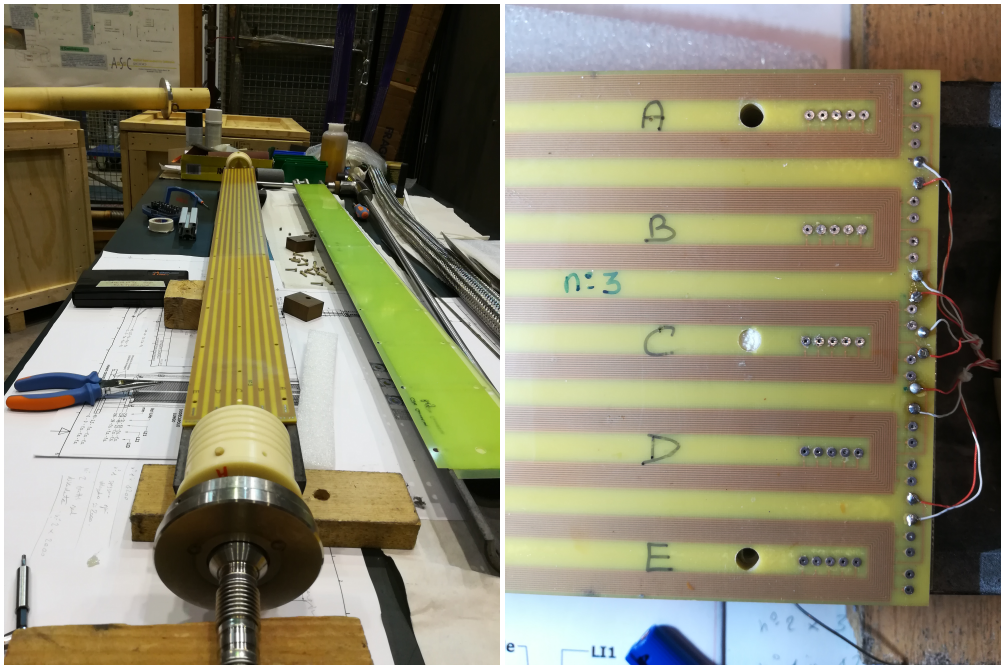

Figure 2.9: *Details of the single rotating coil temporary shaft used for the measurements of the MQSXFP1 magnet and the first batch of HO corrector series. The PCB runs for all the length of the shaft and two layers of Kapton are used to insulate the copper paths from the carbon-fiber case (left). Each PCB, as described in the theoretical model of the rotating coil measuring method, can be composed by several single windings like the 5-coils layout here adopted.*

To retrieve the real magnetic field quality and the magnetic field produced at the reference radius a software extrapolation is performed offline by scaling the single magnetic field harmonics. The distance of the magnets in the vertical cryostat configuration has been studied to prevent any cross-talking up to the full magnets powering. In particular, the length of the PCB coils of the new shaft has been set to cover the entire magnetic length of all the HO correctors with different pickup coils. To evaluate the exact needed length, we can calculate the variation of the magnetic field sampled by the rotating coil. In Fig. 2.10 we reported the magnetic radial field produced by every single HO corrector of the series as a function of the rotational axis position z. We can observe the difference between the short magnets like the MCSXF, MCOXF, and MCDXF, and the longer magnets like MQSXF and MCTXF. Using the profile and choosing a length of the PCB coil, we can calculate the lost fraction of the sampled magnetic field produced by the magnet during the magnetic field measurement with the new rotating shaft. To cover all the produced magnetic fields, the new

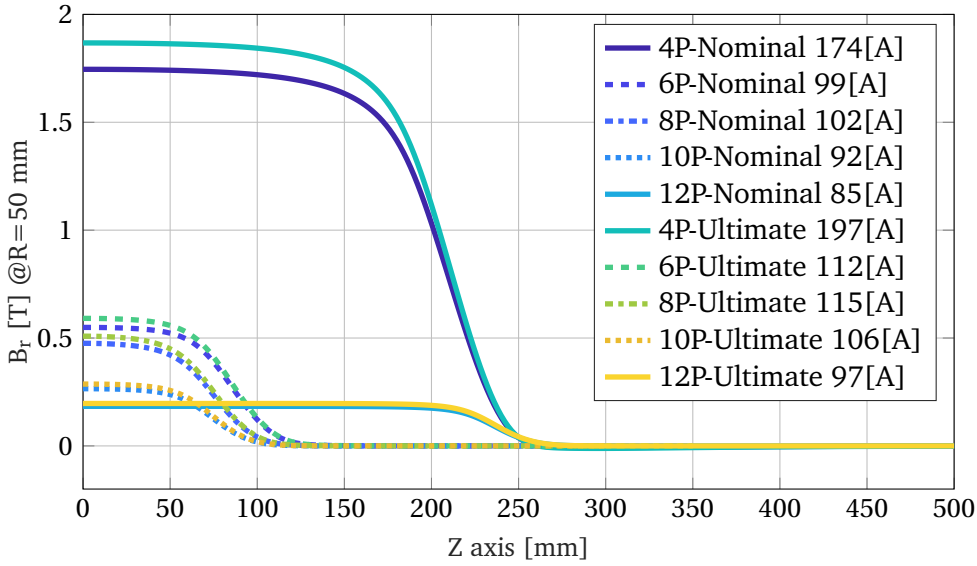

Figure 2.10: *Graphic of the variation of the produced magnetic radial field of the HO corrector magnets at the reference radius of 50 mm from the magnet rotational axis. The produced profile from each magnet is also reported at the nominal and ultimate current.*

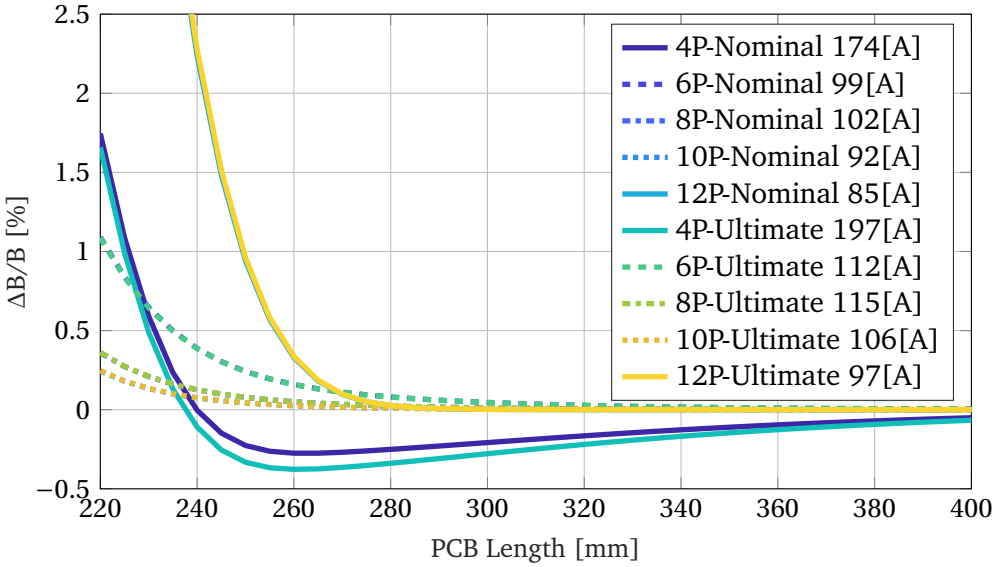

Figure 2.11: *Rapresentation of the fraction of the produced magnetic field for each single magnet which is lost by the PCB rotating coil as function of the length of the paths.*

shaft mounts two connected PCBs at the bottom slot, where the longer magnets will be mounted, to double the sensitive area. Indeed, the reported lost fraction, see Fig. 2.11, is considered for a single PCB coil mounted on the center of the shorter magnets and for two connected PCB coil mounted together in the lower slot of the rotating coil shaft. The required distance between the magnets in the vertical cryostat configuration has been set to be higher than the free space between the correctors when mounted in the beamline layout at LHC to avoid any cross-talking effect. The free space allows for PCB coils of 358 mm which assure a cover of the produced magnetic field higher than 99.7% for each type of magnet. The required distances between magnets in the beam layout are 45 mm between each short corrector and 90 mm space between MCTXF and MQSXF magnets. To evaluate the cross-talking effect, 3D simulations of the fringing field of the magnet prototype layout initially had been already performed using COMSOL by Dr. Giovanni Volpini, [24]. An improved analysis has been performed on the final prototype and magnet series layout using OPERA 3D software. The cross-talking effect has been evaluated both in the electromagnetic attraction between energized magnets and in the variation of their magnetic field quality if mutually coupled. Since the electromagnetic fringing field decreases with the order of the magnet two possible critical configurations of the magnets have been studied to evaluate the magnitude order of the cross-talking. Considering the layout in the interaction region in the beam lattice at CERN, the interaction between a normal and a skew sextupole has been simulated measuring the magnetic field produced and analyzing the field quality variation due to the induced magnetization, reported in Table 2.3.

TABLE 2.3.
CROSS TALKING BETWEEN MCSXF AND MCSSXF

Order	MCSXF		MCSXF on MCSSXF off		MCSXF + MCSSXF	Both On	
	a_n units	b_n units	a_n units	b_n units	A_n/B_n Tmm	A_n Tmm	B_n Tmm
3^{rd}	0.038	10000	0.019	10000	63.645	63.643	63.621
9^{th}	0.034	0.394	0.005	0.367	0.003	-0.004	0.002
15^{th}	0.004	-0.540	-0.003	-0.539	-0.003	-0.004	-0.003
21^{st}	-0.003	0.021	-0.002	0.022	-	-	-

In the simulations, the magnets are reproduced at their nominal current and the variation in the field quality is evaluated powering both and only one of them. Powering the normal sextupole and observing the shift of the skew harmonics the not allowed harmonics are negligible and are not considered. The allowed harmonics show to be all less than 1 unit and the total variation

TABLE 2.4.
CROSS TAKING BETWEEN MQSXF AND MCTXF

Order	MQSXF standalone	MQSXF + MCTXF off	Variarion
	B_n [Tmm]	B_n [Tmm]	Δ [%]
2^{nd}	718.76	718.13	-0.006
	b_n [units]	b_n [units]	Δ [%]
6^{th}	11.2	11.5	+2.9
10^{th}	-7.8	-8.1	-2.2
14^{th}	-0.49	-0.26	+62.6
18^{th}	-0.11	-0.06	+62.5

can be considered negligible compared to the single field quality of the magnet. The same study has been performed between the skew quadrupole and normal dodecapole. To study the effect of the cross-talking, simulations of the powered quadrupole are performed standalone and with the presence of the normal dodecapole to add the effect of the iron magnetization. The variation of the harmonics is reported in Table 2.4.

2.6 DESIGN STABILITY

During the construction process of the magnet, the mechanical tolerances of the pieces created for the assembly have to be taken into account for the stability of the magnet design. One of the main parameters under observation during the assembly is the thickness of the iron laminations obtained from the sheets of ARMCO Iron Grade 4 coming from the CERN supply. The nominal parameter accepted during the mechanical assembly for each iron lamination is a thickness of 5.8 mm and they are carefully sorted for every single magnet to match the exact desired length of the iron poles and the total mechanical length of the magnet. The space between the end of the iron pole and the closing iron laminations is occupied, on the connection side, by the PCB box at which every single superconducting coil is soldered. During the assembly of the MCOFX01 and, in detail, during the installation of the closing plates of the magnet, due to the tolerances of the iron laminations, the coil connections with the PCB box have been deformed and pushed towards the iron poles. The proposed solution to avoid the mechanical interference is the re-machining of one of the last closing iron laminations creating different holes corresponding to the position of the PCB screws, see Fig. 2.12. A series of OPERA 3D simulations have been used to evaluate the feasibility of this solution applied to all the magnets orders, focusing on the variation of their performances. Different parameters have been used to evaluate the variation in the simulations: the integrated main field as a function of the current, or equivalent the transfer

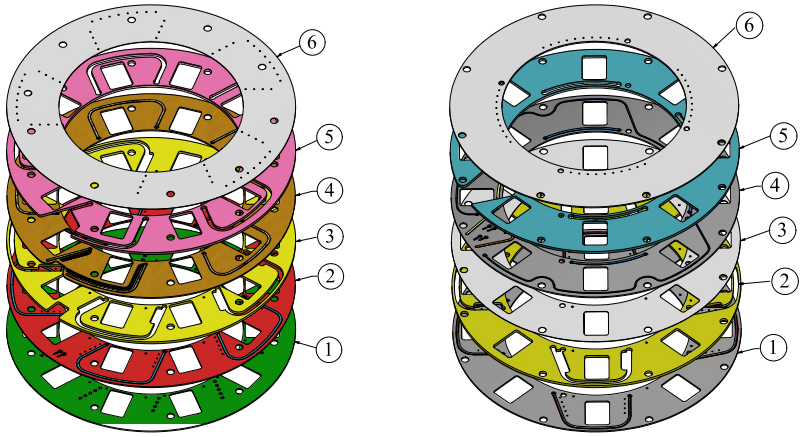

Figure 2.12: *Exploded view of PCB Boxes of MCDXF and MCOXF. All the Arlon layers are clearly visible: Lowe arlon sheet (1),Lower printed circuit (2), Lower PCB protection sheet (3), Upper printed circuit(4), Upper PCB protection sheet(5), Upper arlon sheet(6)*

function, the allowed/non-allowed magnetic field harmonics, and the magnetic field decay rate outside the magnet. Possible effects of the mesh in the model symmetry have been avoided by using the same overall mesh dimension both in the referee simulation and studied cases. Due to the complete asymmetry of the holes in the closing iron lamination, two different simulation cases have been compared for the MCOXF01 magnet to evaluate the magnitude of the variation in the performances. The first simulation has a symmetrical configuration of the holes and the second one is performed with a complete asymmetric distribution which describes the exact position of the holes in the

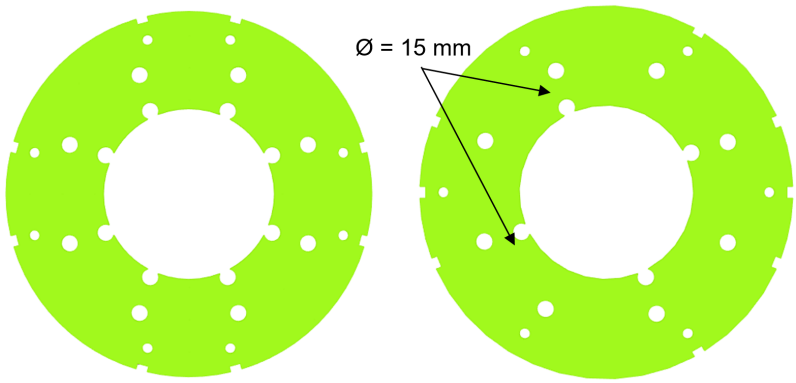

Figure 2.13: *Comparison between the complete symmetrical configuration (left) used in Opera3D for the first simulation and the exact configuration (right)of the holes as inferred from the technical drawing of the PCB box design.*

magnet. The difference in the hole distribution can be immediately recognized in Fig. 2.13. The complete asymmetrical configuration, together with the effect of the holes, considers also the influence of the iron laminations cut near the PCB box created for the connections of the magnet with the bus bar. Because the symmetrical configuration imposes the symmetry of the model to the middle cross-section plane of the magnet, the cut for the connection box is neglected. The results of the simulations for the MCOXF magnet are reported in Fig. 2.14 and Fig. 2.15. The first allowed harmonic is reported to better visualize the most important variation on the produced magnetic field quality. All the other harmonics, especially the non-allowed ones, have a variation of fewer than 2 units over all the range of magnet energization. The little improvement in the field quality is not related to the variation of the main field suggesting that the holes in the last lamination contribute to the compensation of the non allowed harmonics. The same type of study has been performed also on MCDXF, MCSXF, and MQSXF magnets, while MCTXF is not affected by this mechanical interference due to the more space between the superconducting coils, the PCB box, and the iron laminations. Especially for MQSXF, which has a higher integrated main field and more iron laminations, the variation of the magnetic field quality and the integrated main field is negligible. The study has been performed on all the ranges of the magnets energization but, as a summary, only the nominal current of the magnets is reported in Table 2.5. The new configuration used in these simulations considers all the different asymmetries of the holes in the iron laminations and the external cut for the PCB connection contribution. The variation of the harmonics is always lower than

TABLE 2.5.
HO CORRECTORS MAGNETS PERFORMANCE VARIATION

Magnet	Parameter	Units	Reference Value	New Value	Variation
MQSXF I_{nom}=174A	B_2	[Tmm]	699.82	699.80	-0.002%
	a_6	[units]	-7.48	-8.23	-0.75
	a_{10}	[units]	-10.21	-10.45	+0.24
	TF	[Tmm/A]	4.0225	4.0224	-0.002%
MCSXF I_{nom}=99A	B_3	[Tmm]	92.37	93.38	+0.01%
	b_9	[units]	48.21	49.07	+0.86
	a_9	[units]	2.61	1.81	-0.8
	TF	[Tmm/A]	0.9431	0.9432	+0.01%
MCDXF I_{nom}=92A	B_5	[Tmm]	38.57	38.58	+0.02%
	b_{15}	[units]	-1.21	-4.89	-3.68
	a_{15}	[units]	0.01	1.67	+1.61
	TF	[Tmm/A]	0.4192	0.4193	+0.02%

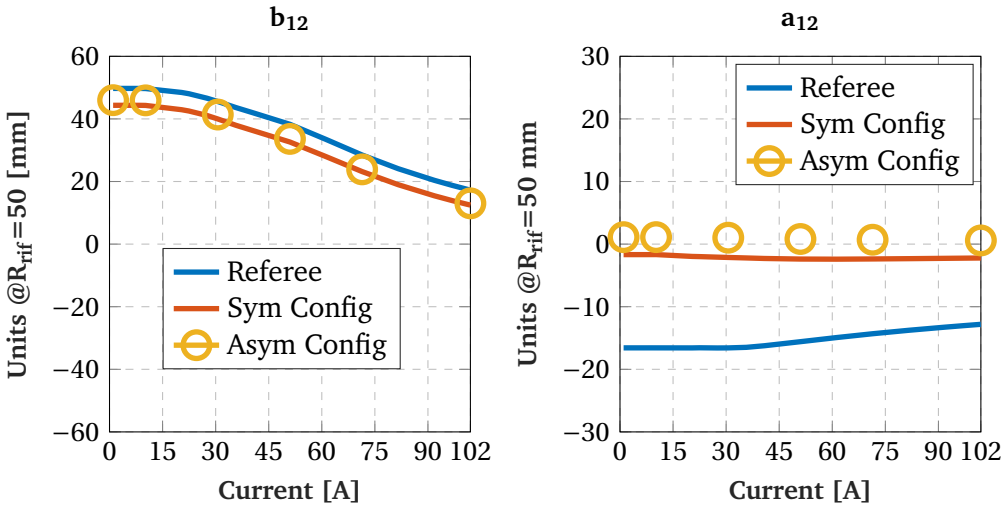

Figure 2.14: *First allowed magnetic field harmonic produced by the MCOXF01 magnet. Both the symmetric and asymmetric configurations are compared to the referee model.*

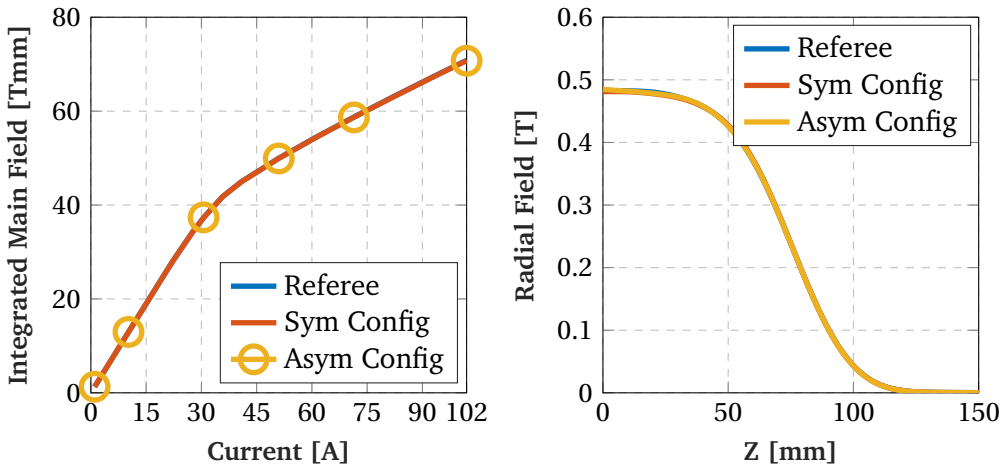

Figure 2.15: *Performances of the MCOXF01 width different configurations of the holes in closing lamination in the connection side of the magnet. Differences in the produced magnetic field can be compared to the uncertainty of the BH curve used in the model.*

5 units for the allowed ones. All the other harmonics here not reported have a lower variation amplitude. the field quality of the new configurations satisfies the requirements from CERN and the variation of the harmonics is compatible with the accuracy of the magnetic measurement system.

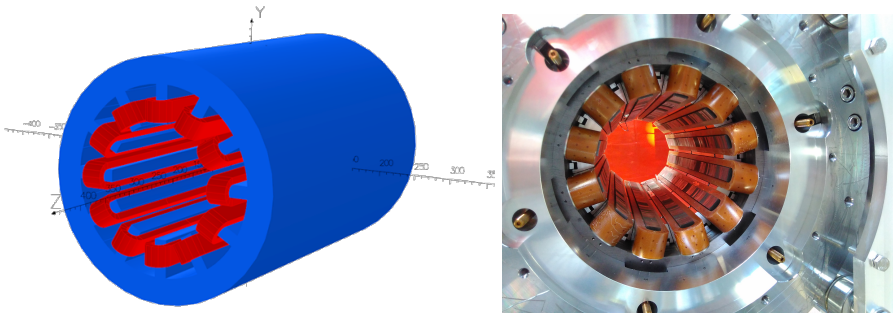

Figure 2.16: *Opera 3D model of the MCTXF magnet which has been used to evaluate the stability of the elctromagnetic design as function of possible misalignment or tilt of the coils and the iron lamination during the assembly (left). Picture of the assembly of the first real MCTXF magnet of the series production, courtesy of SRV s.p.a. (right).*

An extensive study has been also performed to evaluate possible errors during the construction process due to possible misalignment of the iron laminations inside the magnet or the coils around the iron poles. A 3D model of the MCTXF magnet, chosen for its length and magnetic field quality which has a high sensibility to misalignment and error of positioning, has been used to evaluate the magnitude of the possible errors, see Fig. 2.16. The mechanical tolerances evaluated through 3D magnetostatic simulations are displacements of the coil packages center towards one of the iron poles. This displacement can be observed in the produced superconducting magnets due to the tolerances of the coil dimensions and their supports which lay on the side of the iron yoke between two neighboring poles. In the simulation, all the coils are displaced in one of the transversal directions to the rotational symmetry axis up to 0.1 mm. The variation of the magnetic field harmonics, calculated at this maximum displacement, has shown the increment of the nearest magnetic field harmonics to the main order of the magnet. The non allowed harmonic b_5 is equal to -47.4 units and the non allowed harmonic b_7 is equal to -4.6 units. The skew components of these harmonics are not produced by this type of displacement and are less than 1 unit (compatible with the precision of the measurements of the rotating coils system). A skew component of the magnetic field harmonics is eventually produced with an angular phase of the position of the coil inside the magnet. The angular initial phase of the coil package has been calculated making the hypothesis that the first coil is displaced against its pole in the $\vec{e_\theta}$ direction and all the other coils follow the same behavior due

to the loading of the wedges against their long sides. The main harmonic produced by this displacement is the skew a_6 which is equal to 20.4 units due to the reduced value of the magnetic field main harmonic B_6. The tilt of the superconducting coil has been analyzed by applying a rotation to the iron structure around one of the transversal directions (x or y in Fig. 2.16). The maximum possible rotational displacement of 0.1 mm is limited by the gap between the coils and their mechanical supports at the end caps of the magnet. The effect of this type of displacement on this particular model of the magnet is negligible and hard to separate from the uncertainty of the simulation model. The last possible displacement of the coils to the iron package reference system is a translation along the rotational axis of the magnet. The end supports of the coils, in the end caps of the magnet, limit also this displacement to a maximum of 0.3 mm. To evaluate the effect of this misalignment, a single coil of the model has been shifted in the longitudinal direction without affecting all the other coils. The only non allowed harmonic produced by this shift is the skew a_4 which results equal to -1.1 units. Considering the accuracy of the magnetic measurement system, the two last displacements cannot be evaluated for every single magnet due to their low impact on the total magnetic field quality. Instead, a small rotation of the coils around the rotational axis or their global displacement in the transversal direction can be easily evaluated through the magnetic measurement system installed at LASA and therefore corrected before the installation in the accelerator lattice.

2.7 Magnetic Field Quality

2.7.1 MQSXFP1 magnet

The first magnetic measurement, performed using the rotating coil system installed at LASA, has analyzed and characterized the performances of the MQSXFP1 corrector magnet. Two different assemblies of this particular magnet have been measured: MQSXFP1b and MQSXFP1c. The third assembly MQSXFP1c has been measured with MCDXF01, which is the first magnet of the series production, using the same temporary rotating coil provided by CERN. To center the magnets in the rotating coil reference system, the feed-down correction, previously described in Section 1.5.2, has been performed at room temperature before the magnet cool-down in the vertical cryostat. The center of the magnet has been aligned with the rotating coil reference system with a maximum displacement of 0.2 mm (in the [x,y] coordinates plane) to avoid possible non-linearities in the evaluation of the magnetic field produced by the magnet. The centering procedure has been checked before and after the magnet mounting structure movement into the vertical cryostat to check for any residual misalignment released by the mechanical vibrations of the shift. The

compensation scheme used for the measurement is the classical quadrupole compensation and the sensitivity coefficient of the shaft has been calculated at cryogenic temperature applying thermal contraction variation coefficients to the geometric parameters of the rotating coil. Two magnetization pre-cycles up to the ultimate current have been performed on the magnet before the stair-steps measuring cycle which amplitude has been fixed to 20 A for each step. The measured main component of the magnetic field produced, see Fig. 2.17, has been compared both between the two different assemblies and together with the 3D simulations, performed with OPERA 3D with the standard BH curve of the ARMCO iron provided by CERN. In the MQSXFP1b assembly, the integrated main field at the nominal current is equal to 709 Tmm (700 Tmm calculated from the simulation) while, at the ultimate current. it is equal to 760 Tmm (756 Tmm for the simulation). The same values have been measured for the assembly MQSXFP1c. The measurements on this assembly have been done during the first cryogenic test, where the magnet has been powered to reach the ultimate current and perform all the training process, and the second cryogenic test after a thermal cycle used to evaluate the memory of the magnet. All the results are compatible with the previously measured values showing very good repeatability of the produced magnetic field. Analyzing the main integrated field, or equivalent the transfer function of the magnet, see Fig. 2.18, the residual magnetization level at zero current is less than 0.8 Tmm (1‰ of the produced magnetic field at nominal current) showing very good magnetic permeability of the iron used for the magnet. Very good compatibility has been obtained with the simulation data showing that the discrepancy between the measured integrated main field and the calculated one is equal to a Δ =1.2% at the nominal current and equal to the Δ =0.5% if calculated at the ultimate current of the magnet. Analyzing the plateau of the transfer function for low values of energizing current, the measured magnet shows a slightly different linear behavior from the simulated one. This difference is also clearly visible in the crossing of the experimental and simulated curves at 56 A when the iron poles of the magnet start to saturate. Analyzing the measured magnetic field quality, the magnet is perfectly within the requirements imposed by CERN quality department. All the magnetic field harmonics are well beyond the limit of 100 units and in particular: the normal non-allowed harmonics have a maximum range of 1.5 units, on all the magnet power spectrum of currents, while the skew non-allowed harmonics have a maximum variation of 5.1 units. The only allowed harmonics (a_6,a_{10} and a_{14}) are reported in Fig. 2.19 on the right. The shape of each single allowed harmonics is very well reproduced by the simulations with a small offset on all the currents ranges. This possible effect may be due to a rotation of the magnet coils or a possible magnetization effect especially at low current values where the measured a_6 harmonics saturates before the simulated one. In Table 2.6 we reported all the magnet skew

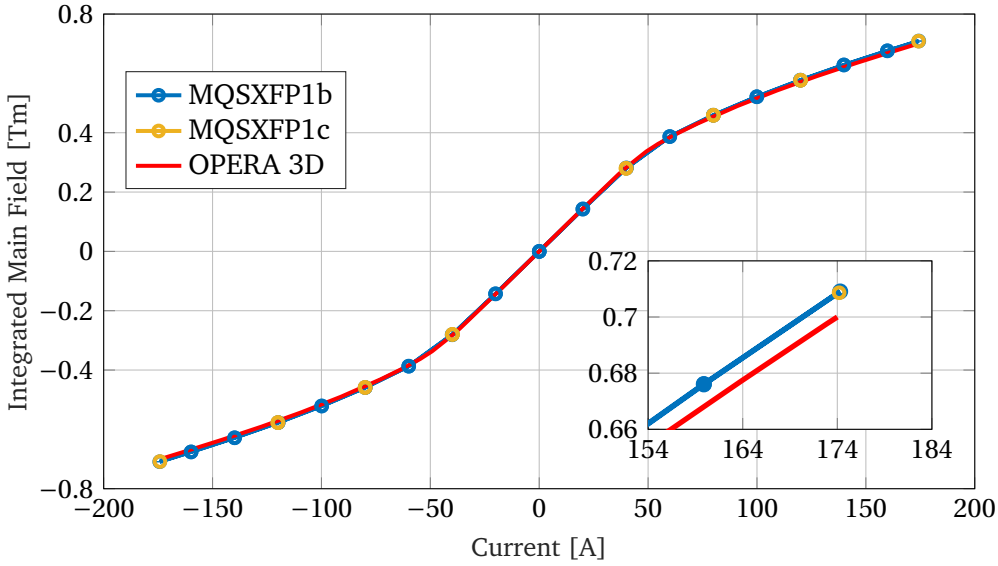

Figure 2.17: *Measured Integrated Main Field at the R_{ref} =50 mm of the MQSXFP1 magnet. Both the two measurements of the different assemblies are clearly visible and are compared to simulations. A zoomed view of the measurement at the nominal current is reported on the low right corner.*

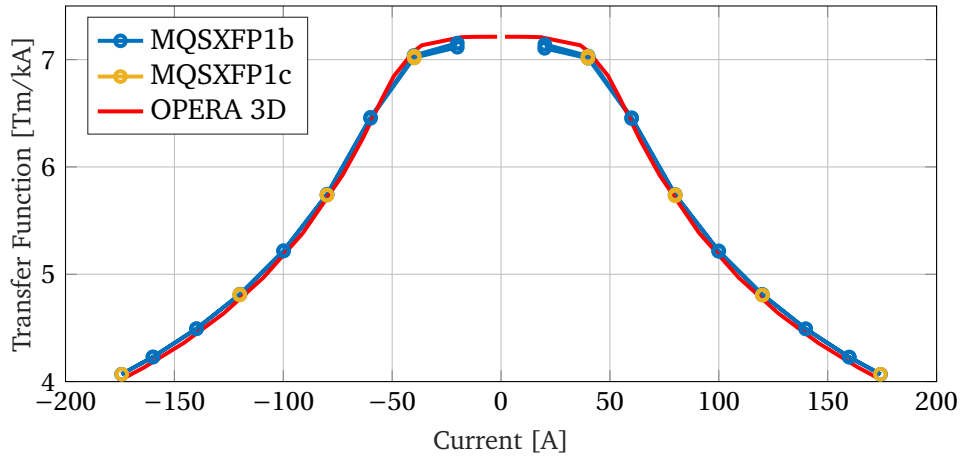

Figure 2.18: *Measured Transfer Function of MQSXFP1 compared to the simulation with OPERA. The shape is well reproduced.*

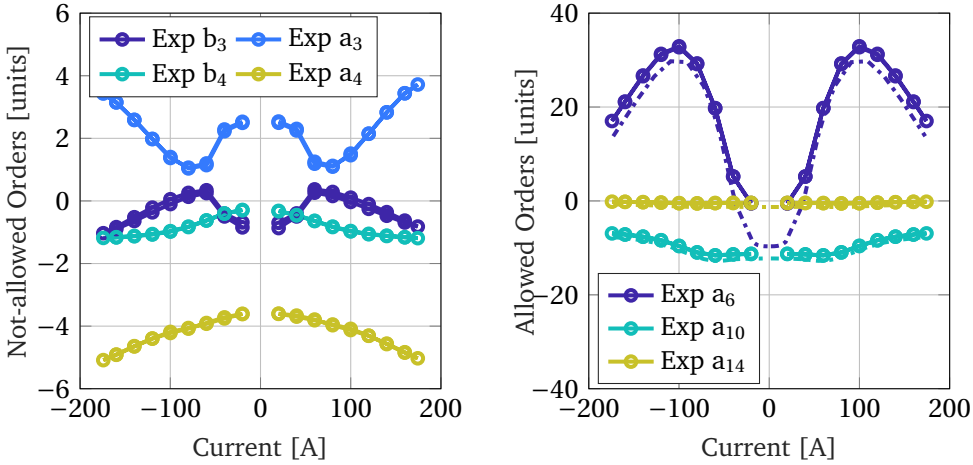

Figure 2.19: *The non allowed harmonics, (left), have a low order of rotational symmetry. Comparison between the allowed harmonics of MQSXFP1 and the calculated harmonic components using FEM simulations here reported in dash dotted line, (right).*

TABLE 2.6.
MAGNETIC FIELD QUALITY OF MQSXFP1

	MQSXFP1b I= ±20 A		MQSXFP1b I= ±174 A		MQSXFP1c I= ±197 A	
Order	b_n units	a_n units	b_n units	a_n units	b_n units	a_n units
3	-0.77	2.51	-0.93	3.57	-2.06	2.21
4	-0.31	-3.61	-1.19	-5.06	0.78	-5.33
5	0.78	1.20	1.17	2.03	-1.9	-0.59
6	-0.16	-0.50	0.37	17.02	0.29	10.71
7	0.12	-0.26	0.14	-0.18	0.08	-0.16
8	0.12	0.36	0.19	0.42	0.13	0.46
9	-0.04	-0.17	-0.13	-0.24	-0.20	-0.08
10	-0.50	-11.28	-0.31	-6.91	-0.32	-6.59
11	-0.07	-0.01	-0.02	-0.03	0.01	0.04
12	0.01	0.01	-0.01	0.01	0.02	0.03
13	0.00	0.01	0.02	0.00	-0.02	0.03
14	-0.03	-0.43	-0.01	-0.16	0.01	0.11

and normal harmonics showing that all of them satisfy the CERN requirements.

2.7.2 MCDXF01 MAGNET

Together with the skew quadrupole assembly 1c, the first of all the magnet series production has been fully characterized at LASA performing both the energization tests and the magnetic field quality measurements. The magnet has been stacked together with the skew quadrupole and positioned above it in the magnet mounting structure for the vertical cryostat tests. The rotating coil used is the same as the skew quadrupole but the two magnets have been powered separately to assure no cross-talking between them. Two magnetization pre-cycle have been performed up to nominal current to establish a well-defined magnetization loop and canceling residual effects coming from energization tests. A stair-step cycle with steps of 10 A has been performed to measure the magnetic field up to the ultimate current. The magnetic field measured at the nominal current of I_{nom} =92 A is equal to 38.9 Tmm which has to be compared with the simulated value of 38.7 Tmm. The magnetic field measured at the ultimate current of I_{ult} =106 A is equal to 42.0 Tmm, compared to the simulated value of 41.8 Tmm. In both cases, the discrepancy of

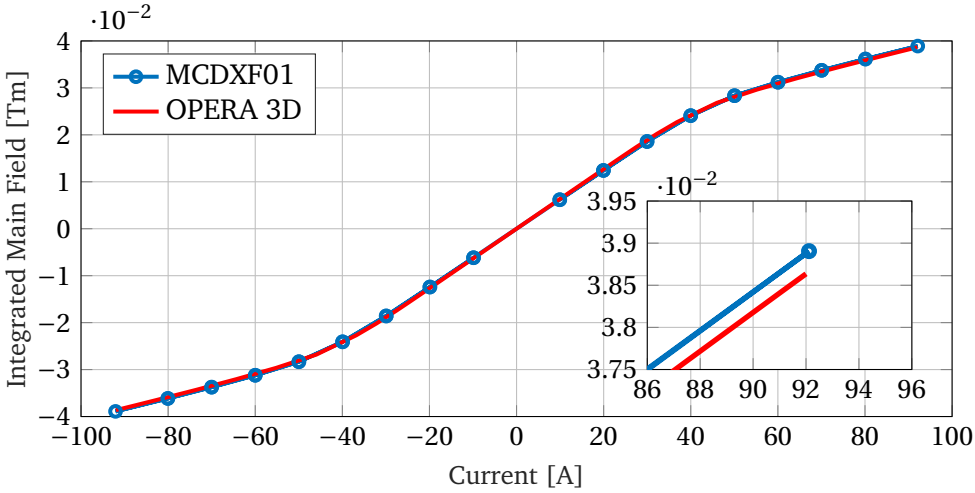

Figure 2.20: *Measured Integrated Main Field of the decapole MCDXF01 magnet. The measured field is higher than the simulated one for values of current below 50 A as happens for the MQSXFP1 magnet. The zoomed view is reported in the right corner to better visualize the integrated main field at the nominal current of 92 A.*

Δ =0.6% at nominal current and Δ =0.5% at ultimate current satisfies the 1% required to validate the quality of the magnet. The same behavior previously described for the integrated main field, or equivalent for the TF is observed for MCDXF01. The simulated values of the magnetic field are higher than the measured one for current values under 50 A with the opposite situation for higher values. In the TF of the magnet, see Fig. 2.21 on the left, we

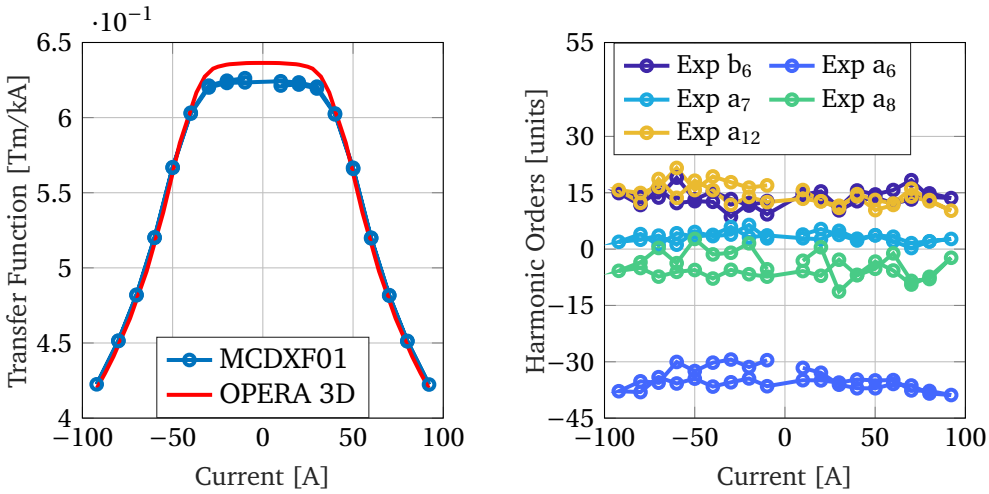

Figure 2.21: *Transfer function of the MCDXF01 obtained dividing the measured main component of the produced magnetic field by the operating current at which the measure is taken (left). Magnetic field quality of MCDXF01 measured in the entire range of magnet energization. Only the harmonics with values higher than 6 units are reported.*

TABLE 2.7.
MAGNETIC FIELD QUALITY OF MCDXF01 @ I_{nom}=±92 A

Order	b_n units	a_n units	Order	b_n units	a_n units	Order	b_n units	a_n units
1	-3	1	6	12	-40	11	6	2
2	10	-1	7	-5	9	12	-6	14
3	1	-5	8	0	-10	13	6	-5
4	0	0	9	0	0	14	5	-2
5	1E4	0	10	-5	-2	15	1	-3

can observe that the plateau reached by the measured data is lower than the simulated one suggesting that the properties of the BH curve used for the simulation are not enough accurate if a precise description of the magnet behavior is desired. Even if the two magnets have not been powered simultaneously, a possible solution to explain the high value of a_6 in the magnet, see Fig. 2.21 on the right, is to consider the residual magnetization of the skew quadrupole as a background dodecapole magnet contribution. Because the rotating shaft is composed of 5 long single coils, the contribution of the residual magnetization of the skew quadrupole cannot be separated in the harmonic analysis of the magnetic field produced by the dodecapole. This issue will be resolved with the new shaft which mounts dedicated PCB coils for each type of magnet in the stacking. In Table 2.7 we reported the complete magnetic field quality of

MCDXF01 evaluated at its nominal current. All the harmonics are beyond the maximum value of 100 units.

2.7.3 MCSXF01

The first batch of the magnet series production has been tested at LASA in the vertical cryostat and the produced magnetic field has been characterized only for the MCSXF01 and MCTXF01 due to the short length of the temporary rotating coil shaft. The measurements of the MCSXF01 magnet have been done with a stair-step cycle with a height of 10 A. The compensation scheme, as for the MCDXF01 magnet and MCTXF01 is done by sampling the two external coils (A and E) to compensate for the off-centering of the magnet or the rotating coil. The main integrated magnetic field, produced at nominal current I_{nom} =99 A is equal to 95.26 Tmm to be compared with the simulated value of 93.49 Tmm.

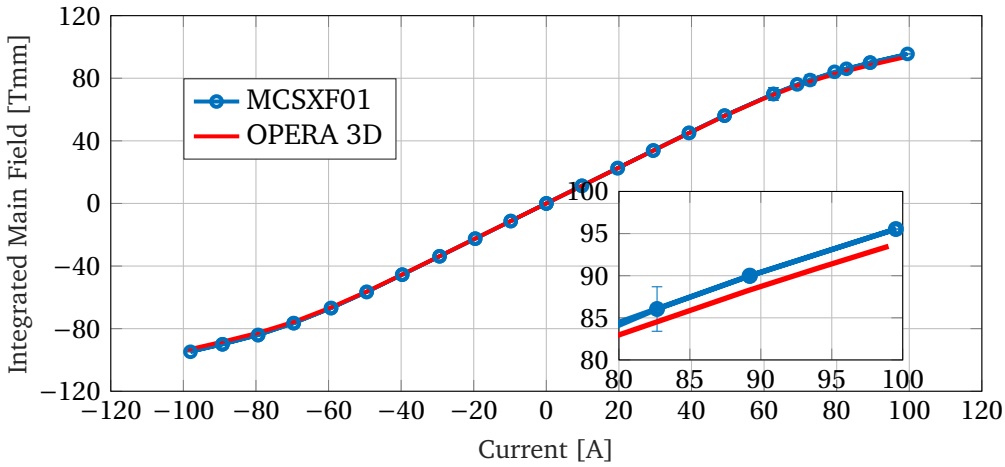

Figure 2.22: *Measured Integrated Main Field of MCSXF01. Precision of the measured data is reported through error bars sowing that the measurement at high values of current is stable.*

The measured value has been obtained through a linear approximation in the last step of the curve due to an offset of the current during the measurement at nominal energization. Indeed, the sampled current value is equal to 99.52 A and is due to the regulation of the power converter which cannot be precisely tuned. The integrated magnetic field measured at 111.6 A is equal to 101.6 Tmm and has to be compared with the simulated value at the same current equal to 100.2 Tmm. The difference between the simulated values and the measured one, Δ =1.8% at nominal current and Δ =1.4% near the ultimate current, are comparable with the results obtained on the other tested HO correctors and satisfy the CERN requirements. All the multipoles of the magnetic

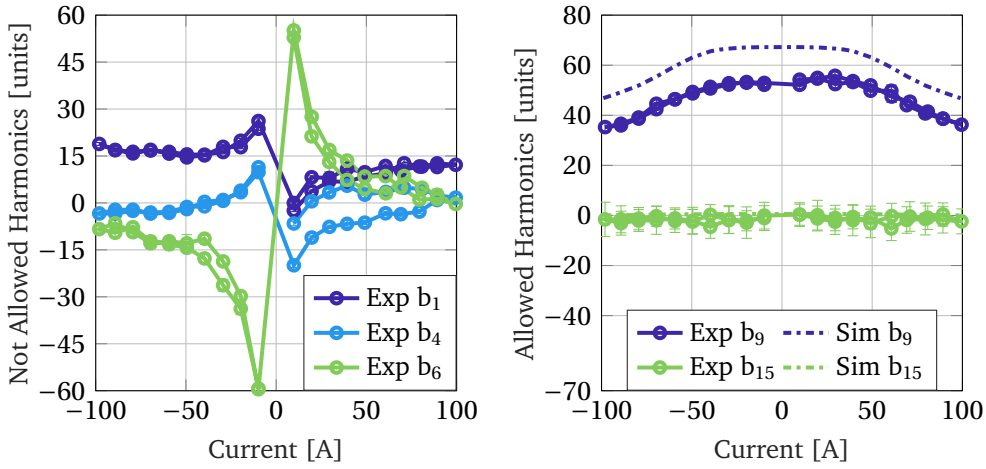

Figure 2.23: *Magnetic field quality of MCSXF01. The not allowed harmonics are reported (left) showing their particular shape which diverges for low current values. The allowed harmonics are reported on the (right) and compared to simulations made with OPERA 3D.*

field produced are within the specifications. Non allowed harmonics up to 30/45 units are considered induced by the residual magnetic field of the other magnet stacked in the mounting system and sampled by the single rotating coil shaft. The allowed harmonics b_9 and b_15, reported in Fig. 2.23 on the right, show an offset, as obtained for MQSXFP1 if compared to simulated values. A possible explanation for this difference could be a rotation of the coils to the magnet reference system.

2.7.4 MCTXF01

The stair-step cycle used for MCTXF01 is the same as MCSXF01 due to the close nominal current of the two magnet types. The integrated main field component is reported in Fig. 2.24 where the saturation of the iron is visible. The measured value at the nominal current I_{nom} =85 A is equal to 86.31 Tmm while the simulated value is equal to 86.13 Tmm. The same difference is obtained also at the ultimate current I_{ult} =97 A with the measured value equal to 93.1 Tmm and the simulated one equal to 92.9 Tmm. The difference, Δ =0.2%, is well within the required specifications and shows a consistent behavior of all the HO corrector magnets. The magnetic field quality produced, as can be seen in the divergence of the harmonics with low current values, is affected by the same residual magnetization effect sampled by the rotating coil used and produced by the other HO corrector magnets stacked in the vertical cryostat. However, all the magnetic field harmonics have a range within 20 units. The

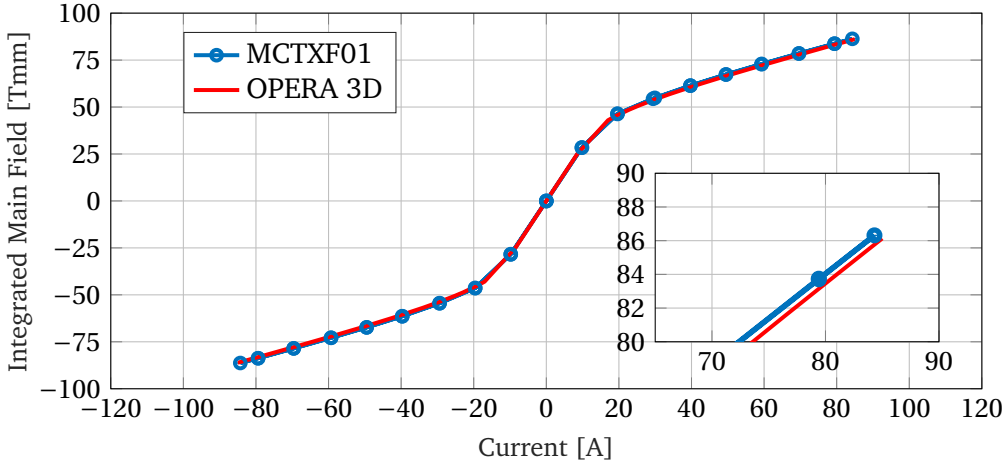

Figure 2.24: *Measured Integrated Main Field of MCTXF01. A zoomed view is reported in the corner to better visualize the nominal magnetic field produced.*

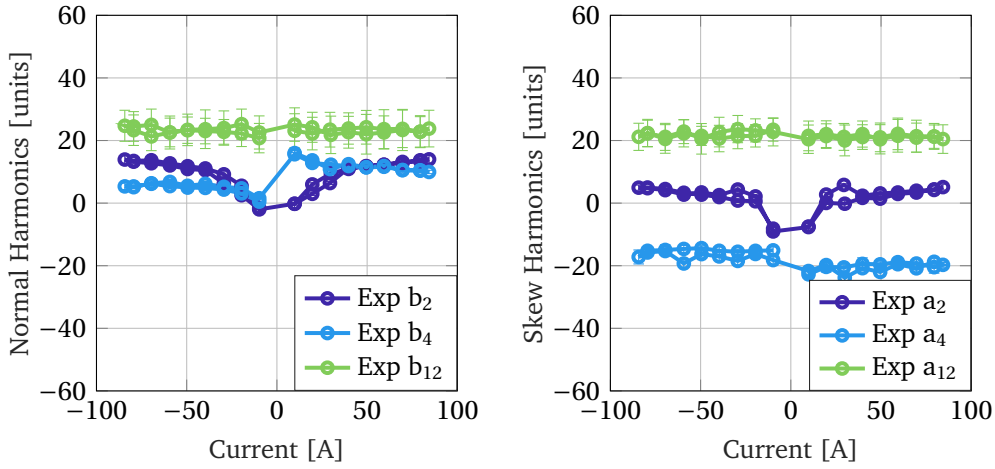

Figure 2.25: *Magnetic field quality of the MCTXF01 magnet. The normal (left) and skew (right) harmonics are reported in this figure.*

first allowed magnetic field harmonic b_{18}, calculated with simulations, cannot be measured by the used rotating coil due to the loss of accuracy with higher orders analyzed.

2.8 Conclusions

In this chapter, we presented the design and performances of the High Order Corrector magnets that INFN has been in charged to produce and test for the

High Luminosity LHC upgrade of the Interaction Region. The electromagnetic and mechanical design has been described focusing on the advantages that the superferric configuration offers to satisfy the constraints and requirements imposed by the IR machine lattice. A description of the study of the HO corrector magnets design stability has been reported showing that the magnetic field quality produced is not strongly affected by the mechanical tolerances of the construction and assembly processes. The new magnetic measurement system installed at LASA for the characterization of the HO corrector magnet series has been described together with the study of the cross-talking between neighboring magnets. The study has been performed mainly with OPERA 3D magnetostatic simulations to evaluate the variations of the performances of a single magnet due to the interaction with the others. Two main configurations have been studied: normal sextupole and skew one or the interaction between the skew quadrupole and the normal dodecapole. In both cases the variations of the integrated main field are negligible and the eventually induced magnetic field harmonics, which are not allowed by the symmetry of the considered magnet, are compatible with the variations in the field quality produced by the mechanical tolerances or electromagnetic properties variation such as the BH curve of the iron. The magnetic measurement system has been validated using a temporary shaft provided by CERN which has characterized the magnetic field quality of MQSXFP1, MCDXF01, MCSXF01, and MCTXF01. The produced main field harmonics have been compared with simulated data showing a very good agreement. The small gap between the experimental curve and the simulated performance is similar for each single analyzed magnet suggesting a common explanation for the different shapes of the calculated and measured main magnetic field. A possible explanation for the main integrated magnetic field shape is the saturation levels of the used BH curve provided by CERN which could be slightly different from the properties of the ARMCO iron used for the construction process. However, at nominal current, all the integrated main magnetic field component is compatible with simulated data and satisfy the CERN requirements. Also, the single magnetic field quality of each magnet has been compared to simulations finding a very good agreement in the shape of the allowed magnetic field harmonics. The not allowed magnetic field harmonics, measured for every single magnet, are principally due to the limitation of the temporary shaft which measure also the residual magnetic field of the neighboring magnets. This issue is already been solved using the new dedicated rotating coil shaft which will measure the second half of the first produced magnets batch and all the future magnets of the series. However, all the field harmonics are well within the CERN requirements of 100 units showing very good performances of all the produced magnets.

Chapter 3
Quench Protection Study

3.1 Superconductivity in Particle Accelerators

In 1911, thanks to the Dutch physicist Heike Kamerlingh Onnes who firstly achieved the liquefaction of Helium at 4.2 K, a new state of the matter at cryogenic temperature, where the electrical resistance drops to zero, was discovered. He observed the first evidence of this new state, which he called superconductivity, in a sample of mercury brought to temperatures below few Kelvin. The study of the matter properties at cryogenic temperatures was a very discussed argument at that time and two main theories were supported by scientists. The first theory predicted that assuming the proportional relationship between the resistivity and the temperature due to the motion of the lattice nuclei, the resistivity would have dropped to zero with the decreasing of temperature and the stop of the lattice motion. This idea, a few years later, was abandoned thanks to quantum mechanic studies of the particle to particle interactions and between electrons and the lattice of the nuclei. The other theory, based on the motion of electrons inside the lattice which would stop at zero temperature, stated that the resistivity would diverge. Onnes observed that none of these theories explained the quick drop of the mercury resistivity to zero and identified a temperature at which the transition to the superconductivity occurs. Since then, many additional studies have been done on the properties of superconducting materials. These studied showed that superconductors expel the magnetic field inside the material (called "*Meissner Effect*"). Many different theories have been developed to explain the superconducting state starting from quantum properties of the material, like the *BCS* (Bardeen, Cooper, and Schrieffer) theory, or inferring the superconducting properties from thermodynamic considerations and empiric formulas. This discovery, and later the observation of the superconductivity in many other elements and composite materials, allowed the development of many practical applications like levitating magnets or high power transfer lines and many others. As we described in Section 1.3, superconducting materials are nowadays mainly used for particle accelerators which require high values of the magnetic field for high energy physics experiments. The transition to the superconducting state is a function of three main parameters: the magnetic field in the material area, the temperature, and the electrical current which flows in the

material cross-section. The two phases (superconducting and normal conducting) are therefore separated by the "*Critical Surface*" and its shape is dictated only by the properties of the superconducting material. The critical surface can be described, for any superconductor material, by the crossing of this surface with the axis of the three parameters space: *Critical Temperature* T_0, *Critical Magnetic Field* B_{c0} and *Critical Current Density* J_c. Common superconductor materials, used in the previously described practical applications, can be classified into two main groups according to their critical surface. Superconductors of the first group are called *Type-I Superconductors* and they show only a single critical surface typically identified by a single value of the magnetic critical field. This value divides the superconducting state, where the Meissner effect is complete, from the normal conducting state and is typically very low if compared to the magnetic field necessary for particle accelerator applications. The second group is formed from the *Type-II Superconductors* and they show two different critical surfaces with two values of the magnetic critical field, H_{c1} and H_{c2}. If the superconducting material operates at magnetic field values below the first critical magnetic field strength, the material shows the same properties of a Type-I superconductor. Between the first and second critical magnetic fields, the external magnetic field can penetrate inside the superconductor but high values of current density can flow in the material lattice without any electrical resistance. If the external magnetic field is higher than the second critical field, the superconducting state is not sustainable and a transition to the normal conducting state is observed. Generally, in the main superconductor materials used in particle accelerators, the second critical magnetic field is much higher than the first critical magnetic field allowing for the construction of superconducting coils for magnets of the accelerator. The most used superconductor for particle accelerator is the NbTi, Niobium-Titanium. Thanks to

TABLE 3.1.
CRITICAL PARAMETERS OF THE NBTI AND NB_3SN MATERIALS.

Material	T_{c0}	J_{c0}	H_{c1}	H_{c2}
NbTi	9.2 K	~10^6 A/mm^2	0.1 T	10 T
Nb_3Sn	18.3 K	~10^6 A/mm^2	0.5 T	25 T

its mechanical properties, like its flexibility and strength when mechanically stressed, and its electromagnetic properties, see Table 3.1, this material is very suitable for particle accelerator magnets coils which operate at the boiling helium temperature equal to 4.2 K. All the LHC dipoles, as we already said, use NbTi coils to generate 8.33 T in the bore diameter and they are cooled down with superfluid helium which reaches a temperature of 1.9 K. Even if the 8.33 T of produced magnetic field is far from the 10 T of the second critical field

of the material, the superconducting coils carry also a huge amount of electrical current density in its cross-section bringing the working point of these superconducting magnets very close to the critical surface. To generate higher magnetic fields, required for future accelerators, the NbTi cannot be a feasible solution and other superconductors have to be considered. Even if the NbTi is still used in many of the planned superconducting magnets for the IR upgrade of the HL-LHC project, which do not require very high magnetic fields, the 11 T dipole and the main triplet quadrupole magnets are made of Nb_3Sn coils. This new superconducting material has been already studied in the last few years for the development of new superconducting and more powerful magnets to be used in future particle accelerators. Even if the superconducting properties of the Nb_3Sn are better than the NbTi, see Fig. 3.1, its mechanical properties have created problems and challenges in the construction of superconducting coils. As opposed to niobium titanium, the filaments of this new superconductor material, are very fragile and can crack with mechanical deformations. Even with low values of strain around 0.2%, the filaments deformations cause the reduction of the critical current density and limit the superconductor performances. To overcome the possible degradation of the wires during the superconducting coil assembling, two types of coil production technologies have been created. In the *wind-and-react* process, the wires used are not made of already reacted Nb_3Sn but of the basic components, which are ductile materials, that make them up during the reaction process. This method simplifies the winding of the superconducting coils but requires high-temperature heat treatment of the wound coil and the use of compatible materials with this process. The *react-and-wind* process, instead, uses already reacted Nb_3Sn wires or cables for the construction of large bending radius coils to prevent high values of strain and huge values of coil degradation.

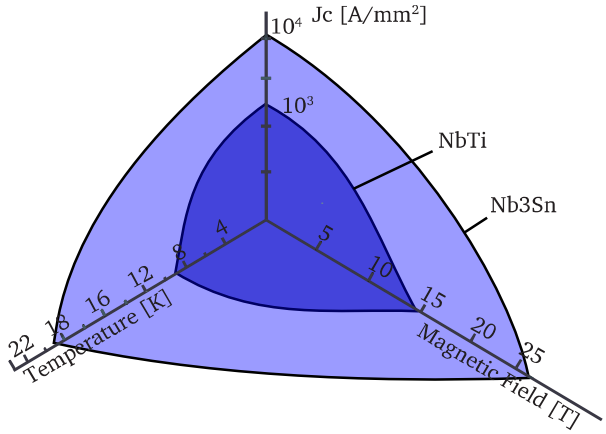

Figure 3.1: *NbTi and Nb_3Sncritical current densities as function of the temperature and magnetic field inside the superconductor strand.*

3.2 Causes of Quench

The "*Quench*" of a superconductor is the transition from the superconductive to the normal-conductive state and the generation of heat due to the not-null resistivity of the material. This process continues as long as there is current density in the material cross-section and can take place when one or more of the three parameters (J, B, T) exceeds the critical values changing the working point of the superconductor over the critical surface. In superconducting magnets, used for particle accelerators, high values of current density have to be used to generate an intense magnetic field for steering and focusing particle beams. When the material leaves the superconducting state and reaches the normal conducting one, the high values of current density can generate a huge amount of heat. The total amount of heat, that could be possibly generated, can be calculated by studying the overall electromagnetic stored energy in the magnet. This energy, dissipated in the material of the superconducting coils, may cause the materials which compose the magnet to melt or even to be permanently damaged. To prevent this catastrophic event, the different causes of the superconducting material transition have been extensively studied and analyzed.

3.2.1 Training and Degradation

All superconducting coils have to be carefully designed and built to be able to control and limit the heat that is generated during the quench of the superconductor wires or cables. One of the main parameters to evaluate the performance of a superconducting coil is the ability to limit or even prevent the quench transition during the energizing of the magnet. In the construction process of a superconducting coil, defects of the cable or the impregnation process could cause the transition of the superconductor and permanently limit the maximum current density value and therefore the maximum magnetic field produced by the magnet. During the energizing of the magnet, the superconducting material in the coil has to support high values of stress due to the Lorentz Forces acting on every single cable or wire. These forces may cause deformation or relative microscopic movements between the wires of the coil producing friction and heat in the superconducting material which then causes the quench of the magnet. After the quench, the reorganized configuration of the wires is more stable than before and can support higher values of forces making it available to power the magnet to higher values of current until another part of the winding moves, creating another quench of the material until a final stable configuration is reached. This process of powering and quench of the magnet due to microscopic movements is called "*Training*" and affects the

energizing test of all superconducting magnets. The performance of superconducting magnets is measured by the higher value of operation current reached during the powering test as a fraction of the critical current value, called "Short sample limit", which is calculated on a short piece of the wire or cable used for the coil. The microscopic deformation of the wires in the coil could also cause the "Degradation" of the material decreasing the local current carrying capability in the superconductor filaments and limiting the magnet performance to some percentage of the critical value. With high values of coil degradation, the stable condition of the magnet could also never be reached and consecutive quench of the magnets could happen to lower and lower values of electrical current density used during the powering. Usually, during the R&D phase of a magnet development, the performances of the scaled magnet prototype and demonstrator can be considered acceptable if the stable zone is reached, in the range of the critical current, with few energizing processes without evidence of superconducting coil degradation. More in general, for the full-scale model of a magnet for a particle accelerator, acceptable performances are considered if a fraction of around 85% of the SSL is achieved during the powering test or, during the series production phase, the requirements are met.

3.2.2 Sources of quench events

The transition of the superconducting material inside the coil is always due to a release of energy within the lattice. The energy released in the material, which operates at a fixed value of the magnetic field and current density, is absorbed in the lattice increasing the operating temperature of the superconductor. Usually, the increase of temperature can be localized in a single spot along the coil length and limited in a finite time interval. Because the temperature of this limited amount of superconductor is not the same as the rest of the coil, the critical level of current that can flow in the coil decreases according to the relationship of the critical surface and the operating temperature of the superconductor. When the value of the critical current, which can flow in the material at the fixed magnetic field and the increased temperature, is equal to the operating current in the coil of the magnet, the material starts the transition to the normal conducting state raising more heat in the coil. To quantify the amount of initial heat that can bring to the superconductor transition we can classify the possible disturbances into two main categories: point and distribute. Each of these categories can also be subdivided, according to the amount of time required to produce the heat in the superconductor, into continuous or transient disturbances. The continuous disturbances are the most common and easy source of quench which affects the superconducting magnets. They are easy to be detected and do not affect the training of the magnet but only its overall degradation. Examples of this type of quench source are steady power

losses in the cables or hysteresis magnetization effects which happen in the superconducting filaments and among neighboring wires during the powering of the magnet. Most of all quench event sources are grouped in the transient disturbances category. They generally affect both the training of a magnet and its overall degradation making very difficult their identification and compensation. One of the most common of these transient disturbances, like for example conductor motion or epoxy cracks, is the "*Flux Jump*". The magnetic field inside the material can penetrate the superconductor lattice due to eddy currents on the surface induced by external magnetic field variation. The current density, involved in this process, increases the net amount of current flowing in the superconductor which can therefore exceed the critical current density threshold and produce heat in the material. In most distributed disturbances, the total volume of the normal conducting zone of the material can be studied neglecting the heat conduction across the external surface or the heat exchange with the superfluid liquid helium at the coil boundaries. The release of heat in the superconductor can be considered, as a first approximation ("*Adiabatic Approximation*"), completely absorbed by the material and ruled by the thermal capacity of the composite conductor. Indeed, the temperature profile of the normal conducting zone is ruled by the heat capacity of all the materials that compose the wire and the insulation of the coil between every single wire or cable. Considering the total heat, Q, generated in the volume V, the final temperature will be described by the following equation:

$$Q = \Delta H = \int_V \int_{\theta_1}^{\theta_2} \gamma C_p d\theta d\tau \tag{3.1}$$

where we considered the variation of enthalpy, ΔH, of the total superconducting volume which absorbs the generated heat. If the superconductor operates exactly at the critical level of current, because the critical surface decrease with the rising of the temperature, it would start the transition even with the smallest amount of heat release. If the heat generation during the disturbance is localized in a small volume of the superconductor, the heat propagation along the coil and exchanged with the cryogenic system cannot be neglected. Considering the scale of time of the localized disturbances, the fraction of the heat exchanged with the cryogenic system can be neglected before the start of the quench and only considered during the quench propagation along the superconducting coil. Considering the balance between the heat generation and the evacuation along the materials which compose the superconducting wires, we can use the Eq. 3.2 to calculate the temperature gradient created in a 1D simplified model.

$$2kA(\theta_c - \theta_0)/l = J_c^2 A\rho l \tag{3.2}$$

The amount of heat generated in the superconductor wire can be described by multiplying the overall current density J_c squared, the average resistivity ρ of the material at the initial temperature of generation, and the volume of the single considered wire Al where A is the wire cross-section and l the averaged length of the normal conducting zone. Both the electrical resistivity and the thermal conductivity k have to be averaged on all the material properties of the wire which compose the wire and evaluated at the operating temperature θ_0 of the rest of the coil which is not already become normal conducting. By knowing the generation temperature θ_c at which the superconductor starts the transition and the material properties of the coil, the previous equation can be also used to evaluate the minimum amount of coil volume which has to be affected by the local disturbance to start the continuous generation of the heat inside the coil. Considering always the 1D model, the length of the so called "*Minimum Propagating Zone*" can be described by the equation:

$$l = \left(\frac{2k(\theta_c - \theta_0)}{J_c^2 \rho} \right)^{\frac{1}{2}} \tag{3.3}$$

If the punctual disturbance affects a total length of the superconductor smaller than the MPZ, the total heat generated heat can be absorbed by the material and evacuated through conduction along the wire. The transition of the superconductor, therefore, will be reabsorbed and the normal conducting zone collapses restoring the superconducting state. To evaluate the magnitude order of the MPZ length, we could consider the thermal and electrical properties of the NbTi and the Nb_3Sn which we already introduced. Considering an electrical resistivity of the normal conducting NbTi at 4.2 K, ρ =2.4 $10^{-7} \Omega m$ and its thermal conductivity $k = 0.11\ W/mK$, the MPZ length is equal to 6.8 $10^{-7}\ m$. The same order of magnitude of the MPZ is obtained for pure Nb_3Sn wires. To obtain a longer length of the minimum propagating zone, composite materials have to be used inside superconducting wires and coils. The main stabilizer used in superconducting wires is copper for its high value of thermal conductivity and low electrical resistivity compared to other metallic elements. Superconducting wires have complex structures which help to distribute the heat in all the volume of the quenched zone. Very thin filaments of superconducting wires are grouped in a stabilizer matrix made of copper or a conductor with high thermal conductivity and specific heat. The stabilizer helps to keep the maximum temperature of the superconducting wire limited and helps to create larger volumes of the minimum propagating zone. The 1D model for the calculation of the MPZ is not suitable to perform a true study of the required specifications of the superconducting wires. A 3D analysis has to be carried on generalizing the MPZ length to a 3D ellipsoid elongated in the direction parallel to the wire (due to the high value of thermal conductivity

along the wire and low value across different wire section which comprehends also the insulation layer) [25].

3.2.3 MIITs and Hot Spot Temperature

During a quench of a superconducting magnet, the huge stored electromagnetic energy, has to be dissipated safely to discharge the magnet and prevent any damage. The amount of energy stored in a magnet can be calculated through the total magnetic energy $\frac{1}{2}LI^2$. Due to the high value of operating current, needed to generate huge magnetic fields in the magnet bore, if the quench propagation inside the superconducting coil is too slow, the total energy is dissipated in a very small quenched volume rising the temperature of the coil material up to magnet damage. To prevent this catastrophic event, the propagation of the quench in the superconducting magnet has to be increased and the maximum temperature reached by the material has to be kept as low as possible. Considering the expansion of the quenched volume inside a superconducting coil, the central region, where happened the perturbation and the transition to the normal resistive state, has the higher value of temperature in the whole area. To study the protection of a superconducting coil, the maximum temperature of this *Hot Spot* is an important parameter that evaluates the performances of the coil materials. Considering the volume of the quenched zone, the hot spot region can be locally considered as a single volume unit which, in a first approximation, does not exchange heat with the neighbor regions. In this adiabatic approximation, all the energy per unit volume generated through the joule effect is absorbed by the specific heat of the material. The temperature of the unit volume can be retrieved by the following equation:

$$J^2(t)\rho(T)dt = \gamma C(T)dT \tag{3.4}$$

where ρ is the overall electrical resistivity of the material, γ the average density, and C the specific heat as functions of the material temperature. Considering a finite time interval, the and isolating all the quantities which are function of the material temperature we obtain:

$$\int_0^t I^2(t)dt = \int_{T_0}^{T} \frac{\gamma C(T)}{A^2\rho(T)}dT \tag{3.5}$$

where we multiplied the current density for the cross-section area of the wire. The obtained quantity on the left, scaled by a factor of 10^6 to deal with the huge amount of energy produced by a superconducting magnet, is called MIITs (the name is an acronym of the physical quantities, I for the current and T for the time, used to construct this variable and the scaling factor adopted M).

$$MIITs(T) = \int_{T_0}^{T} \frac{\gamma C(T)}{A^2 \rho(T) 10^6} dT \tag{3.6}$$

This quantity, measured in MA^2s depends only on the material properties and the geometry of the superconducting wire and define uniquely the final temperature reached by the volume in a finite time interval. To calculate the value of the MIITs of a superconducting cable during a quench, the decay rate of the current has to be known to perform the integral on the left of Eq. 3.5. All superconducting magnets discharge during a quench can be described with an RL circuit model in which the stored magnetic energy of the inductance is dissipated on the total resistance of the circuit. This electrical resistance considers the internal electrical resistivity of the magnet superconducting coil region at the normal conducting state during the quench development, the electrical resistance of the circuit component, which in general can be neglected, and an external dumping resistance tuned to optimize the circuit performance and magnet discharge. After a quench detection, the external dumping resistance, higher than the internal resistance of the quenched zone of the superconducting coil, can be connected in series to the magnet to allow the stored electromagnetic energy of the magnet to be dissipated externally to the magnet material. If the value of the internal quenched zone resistance can be neglected compared to the external one, the decay rate of the current which flow in the superconducting coils of the magnet can be approximated to an exponential decay ruled by the equation:

$$I(t) = I_0 e^{-\frac{R_{dump}}{L} t} \tag{3.7}$$

Using this equation in Eq. 3.6, we obtain the following expression for t$\rightarrow \infty$:

$$\int_0^t I^2(t) dt = I_0^2 \frac{L}{2R_{dump}} \left(1 - e^{-2\frac{R_{dump}}{L} t}\right) = I_0^2 \frac{L}{2R_{dump}} \tag{3.8}$$

From this equation, the final temperature of a material, knowing the material properties of the composite structure, is only ruled by the initial current which flows in the superconducting magnet, its inductance, and the external resistance on which the load of the magnet is discharged. However, to protect a superconducting magnet, the detection of the transition of the material is a critical aspect for the safety of the coil. If the quench is not detected by the protection system the previous equation is not valid and the final maximum temperature is not more a function of the material properties. In this case, the power supply continues to inject a huge amount of electromagnetic energy, which is then converted to heat in the quenched zone, damaging the superconducting material and bringing to the fault of the coil. Generally, superconducting magnets operate near the critical surface of the superconductor

to have the highest efficiency possible. Therefore, the detection of any disturbance which causes the superconductor transition must happen as fast as possible. To detect the superconducting transition, a voltage threshold can be set on the ends of the superconducting coil. Supposing that the quench protection system is triggered at t_d, *detection time*, the MIITs accumulated in the superconductor can be described by the expression:

$$MIITs = I_0^2 t_d + \int_{t_d}^{t} I_0^2 e^{-2\frac{R}{L}t} dt \tag{3.9}$$

The added contribution to the MIITs coming from the detection time of the quench is a function of the material properties of the superconducting coil. Indeed, faster quench propagation velocities produce a short detection time and therefore lower values of maximum temperature reached by the magnet. The second contribution to the total MIITs value is a function of the external dumping resistance and the magnet inductance. For a fixed configuration of the magnet, the free parameter for the quench protection system is the external dumping resistance. The MIITs dependence by the external dumping resistance is an inverse proportion, therefore, higher values correspond to lower maximum temperature reached and faster decay rate of the magnet. However, the external resistance value is limited by the total voltage $V = RI_0$, at the end of the superconducting coil, which is reached at the starting of the magnet discharge. Also, the decay rate of the current cannot be as high as possible because of the high values of turn to turn voltages $V = L\dot{I}$ that will be created during the magnet discharge. For powerful superconducting magnets with high values of inductance and operational current, additional techniques are used for the quench protection system. The main additional system used for particle accelerator magnets is composed of the *quench heaters*. This particular device is composed of resistive strips, usually of a metallic element with high thermal conductivity, placed in direct thermal contact with the superconducting coils along the entire length of the magnet. The main purpose of this system is to create a uniform, faster, and more controlled transition of the entire superconducting coil. When the quench is detected, the quench heaters strips are fired and high values of current flow in this device material. The high values of current generate heat which is immediately exchanged with the superconducting coil material helping to spread the quenched volume decreasing the average temperature of the coil and preventing high values of the hot spot temperature. Considering the reaction time of the quench heaters and the delay due to the heat propagation across the interface between the quench heaters and the superconducting coil, the MIITs can be described by the equation:

$$MIITs = I_0^2 t_d + \int_{t_d}^{t_{QH}} I_0^2 e^{-2\frac{R}{L}t} dt + \int_{t_{QH}}^{t} I^2(t) dt \tag{3.10}$$

Another technology to active internal discharge the magnet stored energy in the superconducting coil material and prevent high values of the hot spot temperature which would cause the magnet fault, is CLIQ [26]. This new technology relies on the generation of high coupling loss in the superconductor material directly producing heat in the conductor itself. The losses in the conductor material are created by directly impose a forced oscillation in the magnet current discharge which enhances the variation of the coupled magnetic field in the conductor and create additional eddy currents. Comparing the diffusion time, requested in the quench heater technology, with this new one, the CLIQ method results to be much faster for the quench protection of a superconducting magnet. Also, by coupling the CLIQ technology with the quench heater devices, like for example reported in [27], lower values of hot spot temperatures can be achieved allowing to develop a more robust and redundant quench protection system. Thanks to the faster intervention time and the reliability of the system, this new technology is currently studied to be used with standard quench protection methods, see [28], for the protection of future Nb_3Sn superconducting magnets for particle accelerators like the Future Circular Collider project.

3.3 Prototype Design and Protection

3.3.1 Material Properties

As we have already seen in Chapter 2, the High Order corrector magnets for the High Luminosity LHC upgrade project have all NbTi racetrack superconducting coils which allow simplified procedures for the winding, impregnation, and assembly process. The wire used for all the prototypes and series production coils is a NbTi wire produced by the Bruker industry and developed for both superconducting magnet accelerators and fusion reactor applications. The single-strand cable has a ratio, between copper and superconductor fractions, of 2.3. The RRR value of the wire has to be higher than 100, typically between 160 and 200, to assure low values of resistivity in case of a transition to the normal conducting state. The wire has a high number of filaments of 3282 to reduce the magnetization level of the superconductor during operation. Two different superconductor wires from the same batch are used for the HO corrector magnets. For the shorter corrector magnets and the normal dodecapole (MCTXF), the NbTi wire has a diameter of 0.5 mm with single filaments diameter of 5 μm. Instead, the skew quadrupole, due to the high value of stored

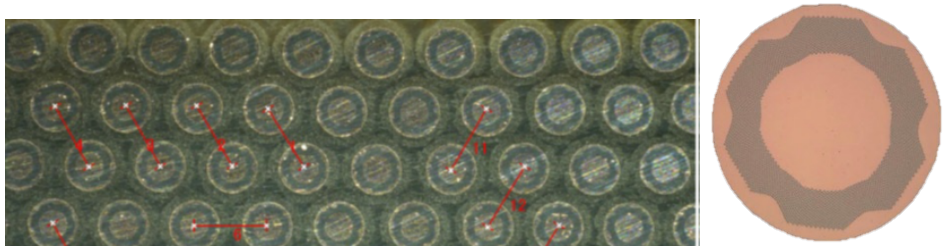

Figure 3.2: *Cross section of a superconducting coil produced for the MCBXF magnet and analyzed to evaluate the stacking factor of the wires during the winding process,(left) [29]. Cross section of a single wire. The central core, made of copper is surrounded by the thin NbTi filaments which are then isolated with a second layer of copper (right), courtesy of M. Statera,INFN.*

electromagnetic energy, has a wire diameter of 0.7 mm with filaments diameter equal to 7 μm. Both two wires have an external insulation layer of S2 glass with a thickness of 0.07 mm. Because the HO corrector magnets have several turns going from 200 up to 450, the total length of the cable for the prototype development has been 16 km and more than 100 km for the series production. The superconducting coils are wound through a winding machine that applies constant and controlled traction to prevent any overlapping between the single strand cables or defects that can cause deformations after the impregnation. The winding is impregnated with CTD-101K epoxy resin to provide radiation damage resistance at the coil and fix the relative position of the cables. All the coils have the same design for the ground insulation layer. Each racetrack coil is wound around a unique BTS2 sheet of 0.15 mm thickness mounted on the mandrel of the winding machine. Different laminations and layers on the top and bottom of the straight part of the coils are assembled during the winding process in the impregnation mold together with the superconducting wires winding. The end spacers laminations, which cover the end

Figure 3.3: *Cross-section of a superconducting coil of the MCTXF magnet to evaluate the stacking factor of the wires in the winding (left). The coils are produced in series and have to satisfy the geometrical quality criteria to be used for the assembling in the magnet(right)*

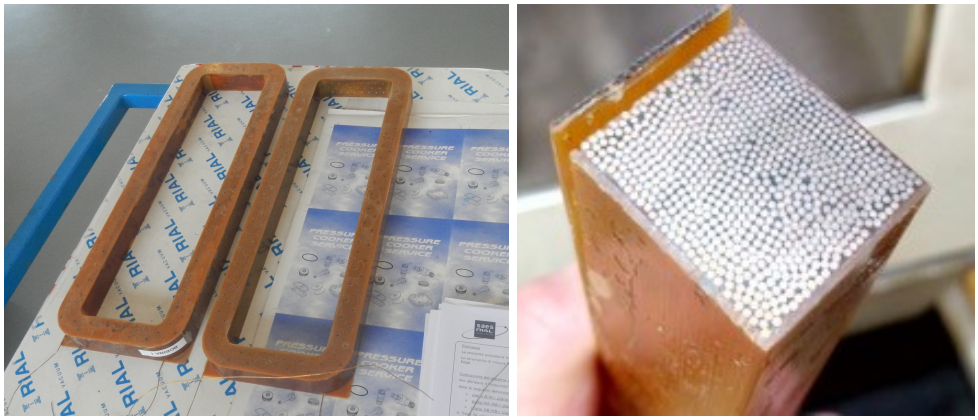

Figure 3.4: *Superconducting coils for the MQSXF magnet ready for the installation, (left). Cross section of a superconducting coil of the skew quadrupolar MQSXF magnet to evaluate the stacking factor and identify possible undesired residual deposit of epoxy resin (right).*

caps of each superconducting coil, have been designed to prevent any resin excess in the coil and are machined from a single block of BTS2. The production of the superconducting coils has been carried on by LASA during the R&D development phase and for the sextupole, octupole, and decapole prototypes construction process. Due to the huge length of the quadrupole and normal dodecapole magnets, see Fig. 3.3 and Fig. 3.4 the development of the superconducting coil for the two prototypes has been performed in the SRV industry which has also been in charged to develop all the superconducting coils for the magnet series. To evaluate the electric and thermal properties of the coils for the quench protection study, both the NbTi and Copper properties have been obtained from the MATPRO database [30], developed at LASA, INFN. To describe the thermal and electrical properties of the CTD-101K epoxy resin and the S2 glass insulation layer, an approximation to the one of the G10 has been used as done in literature, [31]. By knowing the material properties of each material, the thermal and electrical properties of all coil have been retrieved averaging on the amount of material fraction inside the elementary cell of the coil cross-section. The total MIITs, as a function of the temperature in the adiabatic approximation, have been obtained for both the two NbTi wires used for the magnets. The CRYOCOMP database [32] has been also used to evaluate the possible difference of the copper electrical resistivity, as a function of the RRR, and evaluate the influence on the model used for the quench propagation analysis.

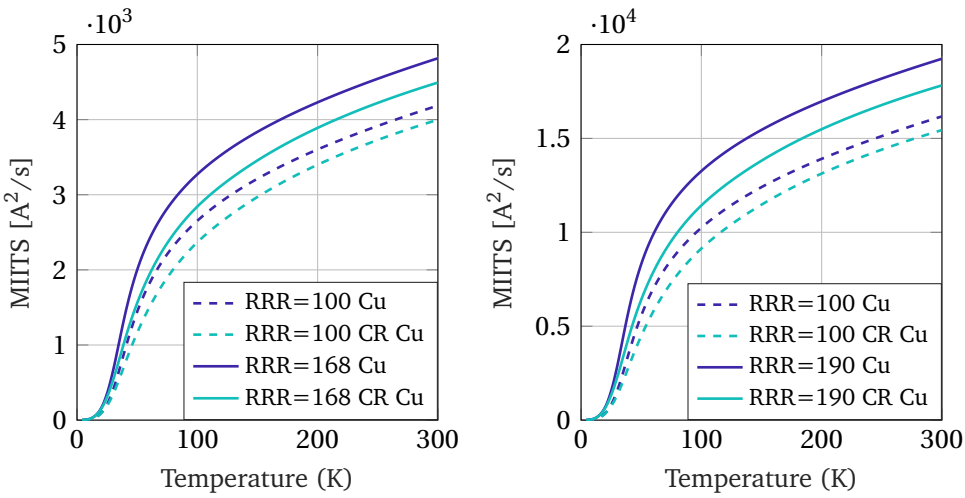

Figure 3.5: *Graphic representation of the MIITs of the two NbTi wires used for the HO corrector magnets. The values are calculated for the measured RRR=168 of the 0.5 diameter wire and RRR=190 of the 0.7 diameter wire, reported by S.R.V. industry, and also for the minimum nominal value RRR=100 as in the magnet technical requirements.*

3.3.2 Protection System

All the High Order corrector magnets, will be installed in the same horizontal cryostat in the LHC lattice of the Interaction Region. The powering of all the 9 magnets string will be separated for each single magnet type and installation configuration (i.e. normal or skew). The quench protection system which will be used during operation in the machine lattice is designed to operate in a current variation measurement mode. To establish the development of the quench inside the superconducting coils, the power supply is designed to disconnect the magnet if the flowing current is different from the designed value. An internal clock time in the QDS system analyzes, with a fixed sampling frequency which period can be set from 20 ms up to 60 ms, the value of the current used to power every single magnet and compare it with the designed value. The power supply tries to restore the designed current value for 3 consecutively attempts and, if it fails, switches off automatically letting discharge the magnet on itself without the using of an external dump resistance or the fire of quench heaters. According to the CERN specification of the new power supply of the magnet in the machine lattice, the provided current is stable until a 10 V resistive voltage appears at the ends of the magnet power lines and then starts to derive according to the load applied. Due to this evaluation time, the maximum time response of the QDS system is 180 ms from the start of the quench growing. The LASA QDS is based on a different approach. The resistive voltage of the magnet is constantly monitored using the two halves of the

magnet subtracting the signals. In the subtraction, the inductive component of the magnet voltage is canceled and only the resistive voltage appears. A fixed voltage threshold of 200 mV is used to detect the quench propagation and development. Thanks to the use of fast digital switches, the circuit of the power supply applied on the magnet is opened in a couple of milliseconds and the magnet is connected to a 0.5 Ω dumping resistance to extract energy from the magnet and speed up the current discharge. Because the magnet prototypes have been tested at LASA in the vertical cryostat, to simulate the CERN configuration and QDS performances, we decided to use, as time response for the quench detection, the value of 180 ms evaluating the worst case for the magnet protection. The voltage threshold that has to be overcome to establish the detection of the quench has been set to 10 V approximating the delay time in which the current provided by the CERN power supply remains constant, letting the quench develop in the magnet's coil. This proposed QDS system configuration is used for the protection of all the corrector magnets except for the Skew Quadrupole. Indeed, the huge value of the electromagnetic stored energy that has to be evacuated from the coil, requires the use of an external dumping resistance protecting the superconducting wires from damages.

3.3.3 Magnets Parameters

The first design of all the High Order corrector magnets prototypes has been changed in 2018 following a better estimation of the main Nb_3Sn quadrupoles magnetic field quality produced (CERN, EDMS internal report 1865591). To better compensate the undesired harmonics produced by the main quadrupoles, a new iteration on the needed performances of the HO corrector magnets has been done. The integrated gradients of the magnets have been increased by changing the length of every single corrector to be 50% higher than the previous value. This modification did not affect the design of the normal and skew dodecapole while the design of the skew quadrupole prototype reported here is already the updated version. The first sextupole, octupole, and decapole prototype had been already built and tested before the design modification, see [14], [33]. All the three magnet prototypes performed very well showing few quenches during the training process up to the ultimate current. The magnets have been pushed beyond the ultimate current and up to the short sample limit of the superconductor wire showing very good performances of the chosen design and construction process. A first rough protection study of the old design has been performed at LASA during the development of the prototype design but no detailed analysis had been done, see [34]. To study the performances of all the HO corrector magnets prototype and evaluate the upgraded design protection, a new complete analysis has been performed comparing the two different configurations of the magnets, except for the dodecapole and the

skew quadrupole. The main tool used for the analysis of the quench propagation inside the superconducting coil is the QLASA software developed at LASA, INFN. This program is a semi-analytical simulating tool firstly developed for the description of quench propagation inside superconducting solenoids and adapted for different geometries. The quench development and propagation are always simulated and calculated in a solenoidal approximation of the superconducting coil to speed the simulation time and simplify the processing. The accuracy of this simulation tool has been verified with many different superconducting magnets. All the magnets quench developments have been simulated from the ultimate current I_{ult}=113.4 A except for the skew quadrupole, simulated at I_{ult}=197 A. All the prototypes, except for the skew quadrupole, are self-protected which means that the external dumping resistance is null and the total detection time for the trigger of the QDS is set to 180 ms. The dimensions of the superconducting coil and their performances change between the different magnet types according to the required integrated main field and the total length of the magnet. In Table 3.2 some of the coil and prototype parameters needed for the simulations are summarized. Inside QLASA, the superconducting coil is not modeled with the original geometric shape but has to be converted to a single solenoid which must have the same total volume, for the calculation of the thermal capacity, the same total length in the wire direction, and the same differential inductance. Considering that all the superconducting coils are connected in series, the mutual inductance matrix, needed to solve the mutual interactions and calculate the total voltage of the magnet, can be diagonalized. In the simulations, the worst-case scenario of one single quenched coil is simulated while all the other coils have only an induced voltage equal for all of them. The number of solenoids that have to be created in the simulation can be simplified considering one solenoid for the quenched coil and one equivalent solenoid with the total volume of all the other coils and the sum of all the remaining differential self-inductance. This method, used for the decapole and dodecapole magnets, allows overcoming the limitation of 10 maximum solenoids that can be handled by the program in the same equivalent circuit. The self-inductance of the quenched coil created in the simulation is equal to the total magnet inductance divided by the total number of the coils. The magnet differential inductance variation, as a function of the energizing current of the magnet, is approximated by the program with a saturation levels curve. The approximation is composed of two different constant values for currents lower than the first saturation current threshold and higher the second one. The range between the two saturation current values is described by a straight line to approximate the magnet iron saturation variation. The values of the simulated differential inductance approximation are reported in Table 3.3. To describe the values of the inductance at the two saturation levels, the inductance value at low current is used as an input parameter and a

TABLE 3.2.
PARAMETERS OF THE DIFFERENT HO CORRECTOR MAGNETS PROTOTYPES

Parameter	Units	MQSXFP	MCSXFP	MCOXFP$_{old}$	MCOXFP
I$_{nom}$	[A]	182	105	105	105
I$_{ult}$	[A]	197	113.4	113.4	113.4
Turns		754	276	372	372
Layers		26	12	12	12
Bare Wire Diameter	[mm]	0.7	0.5	0.5	0.5
Insulated Wire Diameter	[mm]	0.84	0.64	0.64	0.64
Mechanical Length	[mm]	538	235	183	233
L @ I$_{ult}$	[mH]	1505	199.4	166.6	287
Parameter	Units	MCDXFP$_{old}$	MCDXFP	MCTXFP	MCSTXFP
I$_{nom}$	[A]	105	105	105	105
I$_{ult}$	[A]	113.4	113.4	113.4	113.4
Turns		228	228	436	436
Layers		12	12	12	12
Bare Wire Diameter	[mm]	0.5	0.5	0.5	0.5
Insulated Wire Diameter	[mm]	0.64	0.64	0.64	0.64
Mechanical Length	[mm]	183	233	575	200
L @ I$_{ult}$	[mH]	81.2	139	910.6	173.8

scaling factor γ is used to evaluate the second value at high current. The magnetic field map, used in the simulations to evaluate the quench propagation velocities and the working point of the materials, has been obtained through 3D OPERA FEM simulations of both the old and new design of the prototypes. The total magnetic field map cannot be transported inside the simulation program as a matrix in the 3D space over the coil volume. The only input parameters accepted by QLASA are the values of the magnetic field at the corners of the coil cross-section (A, B, C, D coordinates). This rough approximation is needed to simulate the magnetic field on the equivalent cross-section of the solenoid simulated by the program. With this approximation, also the magnetic field variation along the magnet rotational axis is neglected affecting the quench propagation velocities along the coil length. The values used in the

TABLE 3.3.
PARAMETERS FOR THE APPROXIMATION OF THE DIFFERENTIAL INDUCTANCES OF HO PROTOTYPES

Position	Units	MQSXFP	MCSXFP	MCOXFP$_{old}$	MCOXFP
Saturation Current 1	[A]	28	35	18	18
Saturation Current 2	[A]	95	100	90	90
γ		0.295	0.412	0.305	0.361
L$_{coil}$ @ Low Current	[mH]	1275	80.7	68	99.4
Position	Units	MCDXFP$_{old}$	MCDXFP	MCTXFP	MCSTXFP
Saturation Current 1	[A]	20	20	8	5
Saturation Current 2	[A]	100	100	30	23
γ		0.37	0.37	0.1704	0.1532
L$_{coil}$ @ Low Current	[mH]	21.95	32.65	445	94.6

TABLE 3.4.
MAGNETIC FIELD MAP EXTRACTED BY 3D OPERA SIMULATIONS PERFORMED AT THE ULTIMATE CURRENT.

Position	Units	MQSXFP	MCSXFP	MCOXFP$_{old}$	MCOXFP
A(r_{int};-h/2)	[T]	3.95	1.82	2.09	2.27
B(r_{int};+h/2)	[T]	1.7	1.0	1	1.4
C(r_{ext};-h/2)	[T]	2.83	1.2	1.4	1.8
D(r_{ext};+h/2)	[T]	0.1	0.17	0.01	0.01
Position	Units	MCDXFP$_{old}$	MCDXFP	MCTXFP	MCSTXFP
A(r_{int};-h/2)	[T]	1.79	1.82	1.85	1.826
B(r_{int};+h/2)	[T]	0.8	1.0	1.34	1.32
C(r_{ext};-h/2)	[T]	1.1	1.2	1.6	1.55
D(r_{ext};+h/2)	[T]	0.16	0.17	0.01	0.01

simulations are reported in Table 3.4

3.3.4 Simulations results

The results of the performed simulations using QLASA and the magnet parameters already described are presented below. For the decapole and octupole upgraded design, the increasing of the integrated main field component and store electromagnetic energy imply that the maximum temperature and voltage reached by the magnet during the discharge is higher than the old design. Because the skew quadrupole cannot be protected using the internal developed resistance as dumping resistance of the equivalent circuit, a detailed analysis of the best value for the external resistance has been performed focusing on the optimization of the maximum voltage-to-ground and internal voltage developed during the magnet discharge. For all the magnets prototypes, the simulations have been performed with two configurations of the scaling factor applied to the quench propagation velocities. The first configuration does not apply any scaling factor leaving the QLASA program to calculate the propagation velocities from the thermal properties of the materials during the discharge and as a function of the temperature profile. In the second configuration considered, a 30% reduction factor of the nominal speed, calculated by QLASA, is applied to simulate a conservative case for the quench protection. The simulations show that for all the different cases, the maximum temperature, reached by the superconducting quenched coil at the end of the magnet discharge, is lower than the maximum allowed value of 250 K. This result has been obtained considering that QLASA performs an adiabatic approximation of the quenched hot spot volume which is a conservative assumption compared to the real case. The main problem which affects the skew quadrupole discharge is the maximum voltage obtained at the ends of the quenched coil during the transition.

By changing the value of the dumping resistance, the decay rate of the magnet current is modified managing to limit the maximum voltage of the quenched coil. A limit value of the maximum voltage in the magnet has been imposed for safety reasons to keep the probability of short between the coils and ground under control. However, the maximum voltage reached by each of the HO corrector magnets during a quench is also used as a parameter to define the withstand voltage levels during the reception tests, the magnets qualification, installation, and commissioning in the LHC tunnel. As reported in the acceptance criteria required from CERN for the magnet qualification [35], the Hi-Pot voltage is applied to the magnets for a minimum time interval of 30 seconds. The magnets are considered to conform to the requirements if the leakage current measurement results under 10 μA. The Hi-Pot test is performed at different levels of applied voltage in several magnet conditions. According to the electrical design criteria for the High Order corrector magnets, [36], the tests are performed at normal operating conditions of 1.9 K superfluid helium, in the cold mass of the cryostat, and a warm temperature (equivalent

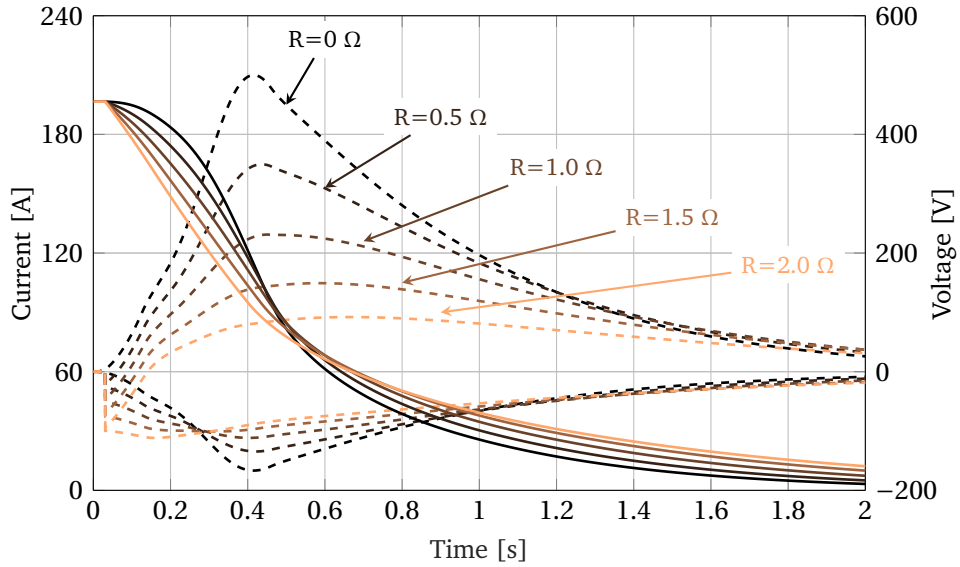

Figure 3.6: *Evaluation of the quenched coil total voltage, upper dashed lines, and single inductive coil total voltage, lower dashed lines during the discharge of the MQSXFP magnet (right y-axis). The decay of current from the ultimate current of 197 A is also reported in figure (left y-axis). The two different voltages and the current decay are simulated as function of the external dumping resistance used for the protection.*

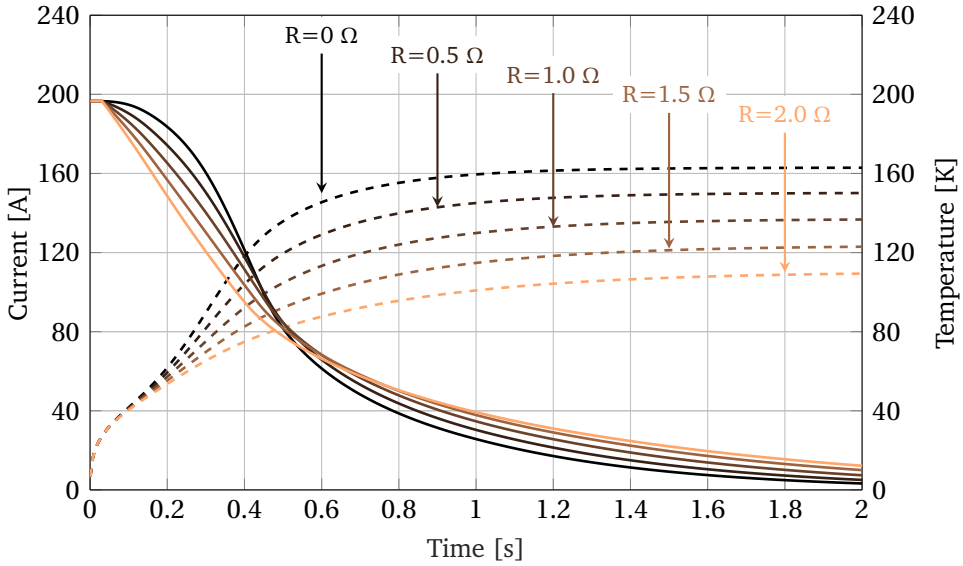

Figure 3.7: *Profiles of the different hot spot temperatures, dashed lines, reached by the quenched coil during the magnet discharge as function of the external dumping reistance (right y-axis). The current discharge is also reported for clarity (left y-axis)*

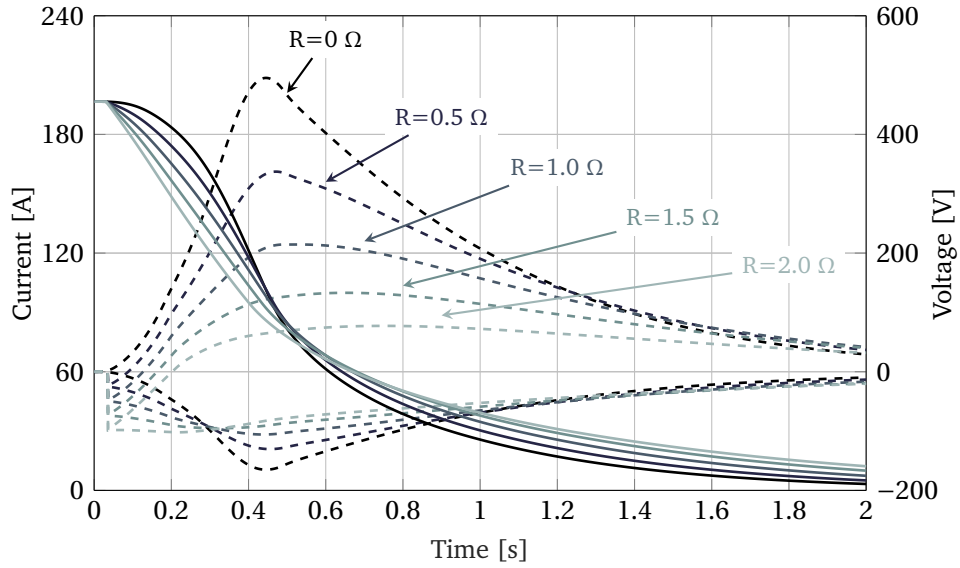

Figure 3.8: *Evaluation of the quenched coil total voltage, upper dashed lines, and single inductive coil total voltage, lower dashed lines during the discharge of the MQSXFP magnet (right y-axis). The current decay is also reported (left y-axis). As for Fig. 3.6 the profiles are shown as function of the external dumping resistance. All the simulations have been performed with the scaled quench propagation velocities (0.7 scaling factor).*

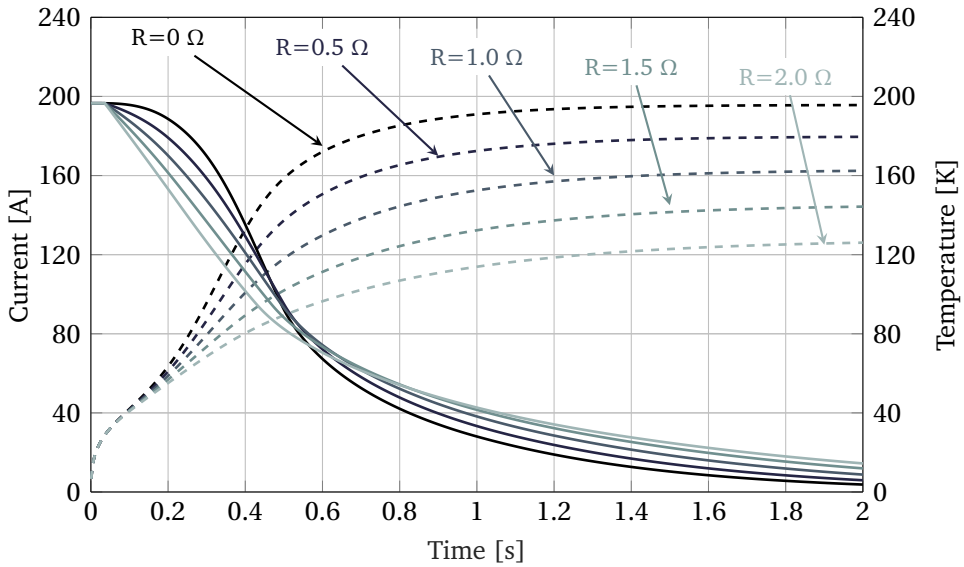

Figure 3.9: *Profiles of the different hot spot temperatures, dashed lines (right y-axis), and current decay (left y-axis) reported as function of the external dumping resistance as in Fig. 3.7. The profiles are referred to simulations with the scaled quench propagation velocities (0.7 scaling factor).*

to room temperature air of T=20±3°C and humidity lower than 60%). Two unique voltage levels, used for the Hi-pot tests of the HO corrector magnets, and in particular, the configuration at warm temperature before the powering tests, have been used to validate all the magnets. The produced magnets are tested up to 1.5 kV except for the skew quadrupole and normal dodecapole which are tested up to 2 kV.

In the case of a quench event during the skew quadrupole powering test, not all the values of external dumping resistance are suitable for the protection of the magnet. Indeed, considering the ground of the equivalent circuit positioned at the end of the series between the magnet and the external dumping resistance, the maximum voltage to ground reached by the magnet is equivalent to the total voltage at the magnet ends equal to $V = R_{dump}I$. This value is

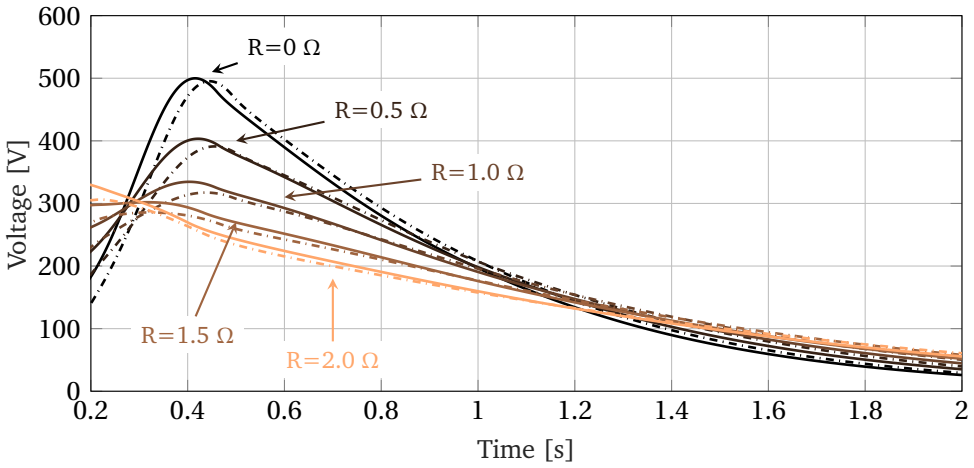

Figure 3.10: *Maximum voltage simulated at the end of the quadrupole MQSXF prototype as a function of the discharge time and evaluated for different values of external dumping resistance. The ground of the protection circuit is fixed at one side of the external dumping resistance.*

reported in Fig. 3.10 for all the time intervals of the magnet discharge starting from the aperture of the power supply circuit and the magnet ends closure on the external dumping resistance. We can observe that for every value of the external dumping resistance, the maximum voltage to ground, which is reached at the ends of the magnet, is higher than 300 V exceeding the limit imposed for magnet safety. To solve this problem and reduce the maximum voltage, we can change the ground position in the equivalent circuit. The best configuration found is to insert the ground in the middle of the external dumping resistance. To create this configuration, inside the LASA power supply system, the equivalent total external resistance is split using two equal resistance, with half of the reference value, inserting the ground in the middle. With this configuration,

the maximum voltage to ground is shifted by the quantity $V = -R/2I$ compared to the previous reference. The maximum voltage to the ground in this new configuration is obtained for the worst-case scenario with the first (or last) coil of the magnet like the one which is quenched. The value of the maximum voltage is equal to the sum of the voltage across the quenched coil and the voltage at the ends of half of the dumping resistance which is opposite in direction. The simulated values for the different dumping resistance are reported in Fig. 3.11.

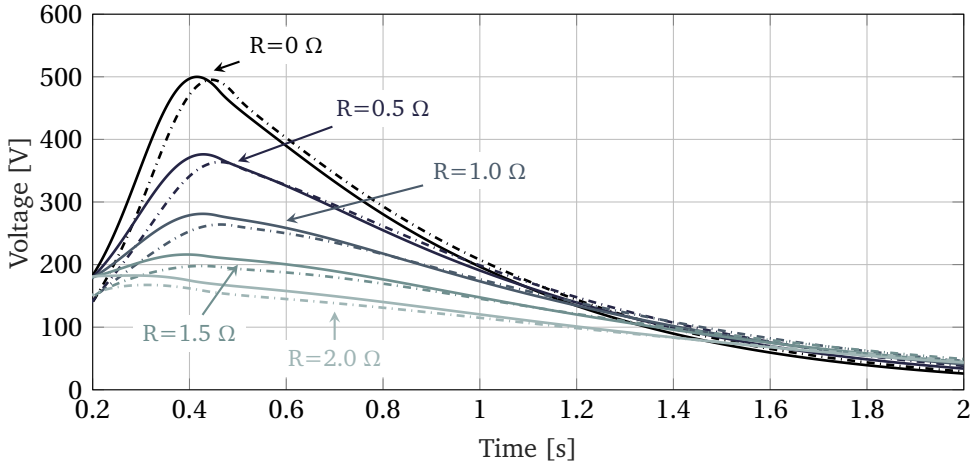

Figure 3.11: *Maximum Voltage towards ground simulated in the protection circuit of the quadrupole MQSXF prototype during a quench event and magnet discharge. The ground of the protection circuit is fixed in the middle of the external dumping resistance lowering the maximum voltage to the ground during the magnet discharge in case of a quench event.*

The best configuration obtained to limit the maximum voltage to ground is the use of an external dumping resistance of 1.5Ω. The results of all these simulations, performed with both the quenched propagation velocity scaled configuration and the nominal one, are reported in Table 3.5 together will all the simulated results of maximum voltage and temperature reached by all the HO corrector prototypes. All the magnets prototypes have been simulated to evaluate their performance during a quench development at their ultimate current. All the magnets, including the skew quadrupole with the new QDS configuration which is different from all the other magnets, are safely protected and do not reach the limit values of the maximum acceptable voltage and temperature of the hot spot region.

TABLE 3.5.
RESULTS OF QUENCH PROTECTION SIMULATIONS FOR THE HO CORRECTOR PROTOTYPES

Magnet	S	Maximum Temperature [K]	Maximum Voltage [V]
MQSXFP	1	122.96	216
	0.7	144.29	197.3
MCSXFP	1	119.75	70
	0.7	141.1	72
$MCOXFP_{old}$	1	117.47	57.7
	0.7	137.5	58.1
MCOXFP	1	140.15	104.4
	0.7	164.2	104.3
$MCDXFP_{old}$	1	123.34	40.7
	0.7	144.93	42
MCDXFP	1	126.53	57.2
	0.7	148.87	57.5
MCTXFP	1	143.6	267
	0.7	174.6	269.7
MCSTXFP	1	125.6	64.7
	0.7	150.7	65.9

3.3.5 EXPERIMENTAL VALIDATION

The electromagnetic and thermal model of the superconducting coils and HO corrector magnet, used for the study of the quench protection of the prototypes, has been validated reproducing experimental discharges of the built prototypes. In particular, two different quenches, provoked after the training of the MCDXFP1 and MCOXFP1, before the iteration on the electromagnetic design, have been reproduced using the old model of the magnets. The training tests have been performed at LASA at 4.2 K in the liquid helium and also at 2.17 K. The protection of the magnets has been verified both with the LASA QDS configuration and the CERN operational QDS system configuration. The LASA configuration used for these tests has a 0.5Ω of dumping resistance which is used to extract the energy from the magnet and the voltage threshold on the resistive signal is set to 200 mV. The CERN QDS system is the same explained in Section 3.3.2 and is replicated at LASA assuming a 180 ms of delay time from the quench detection, see Fig. 3.12. The difference between the experimental current decay and the simulated one is only a few percent for both the two types of provoked discharge of the magnet. The same agreement is obtained also in the total voltage of the magnet and the internal resistive

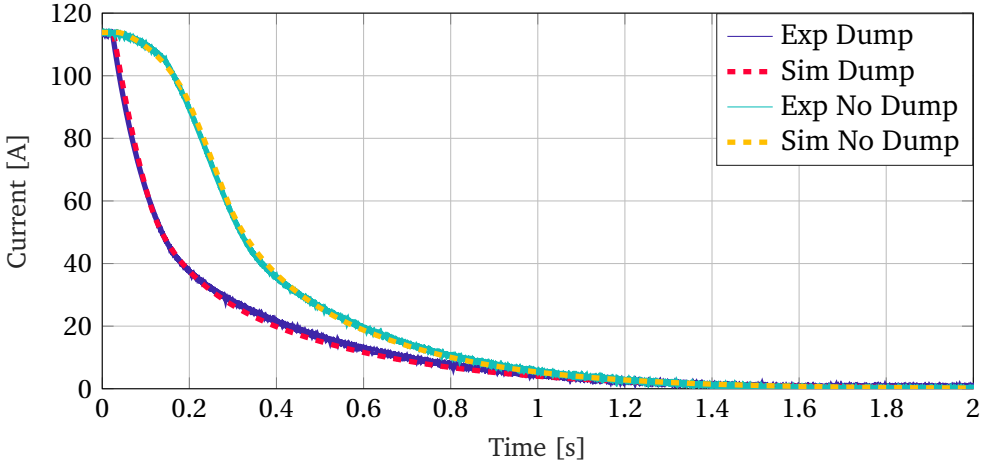

Figure 3.12: *Comparison between the two experimental current decay, obtained during provoked quenches inside the MCDXFP1 magnet test at LASA, with QLASA simulations of quench development*

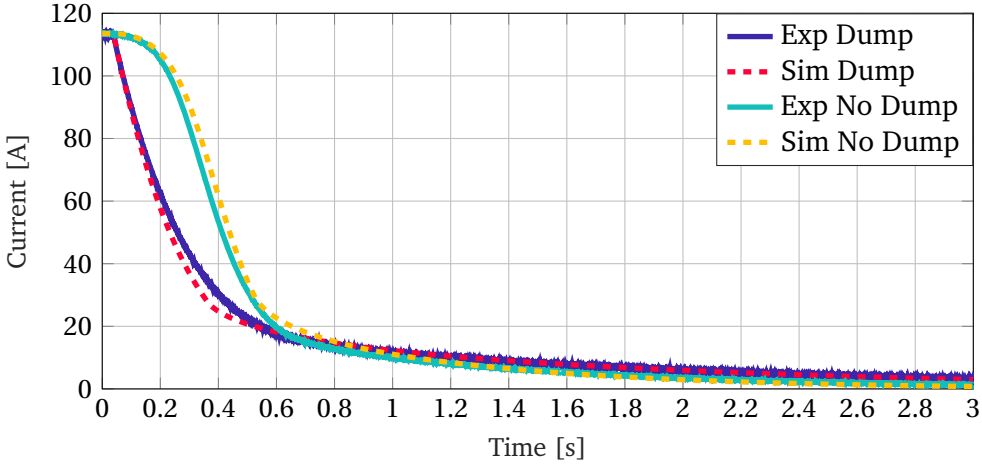

Figure 3.13: *Comparison between the two experimental current decay, obtained during provoked quenches at the ultimate current of the normal dodecapole MCTXFP1 magnet tested at LASA and the QLASA simulation of the quench development in the superconducting coils.*

voltage profile. The simulations reported here have been obtained with nominal quench propagation velocity inside the simulation software suggesting that the thermal end electric properties of the material considered can be used as a good model for the average properties of the superconducting coils. The same analysis has been performed on the provoked discharge of the MCOXFP1 and of other superconducting produced magnets like the first MCTXFP1 magnet

prototype, [37]. For this particular case, the best agreement with the experimental data has been obtained for quench transition velocities at 75% of the nominal calculated values by QLASA during the discharge. The decay rates of the current for the two different configurations of the protection with or without the external dumping resistance are reported in Fig. 3.13. The initial quench development and discharge of the current are very well reproduced by simulations. The fastest part of the simulated current decay is slightly different from the experimental data shape. Considering the possible source of errors in the simulation model and the approximation used in QLASA to model the quench propagation and magnet discharge, the saturation levels model of the inductance variation is the most cause of the simulations difference with the experimental data studied.

3.4 Simulation Model upgrade and Series Protection

All the High Order corrector magnets have been designed and engineered at LASA following a common superferric design optimized for every single type of magnet order. The contribution of the iron to the magnetic field of the corrector is predominant for the generation of the right magnetic field quality and the enhancement of the superconducting coil field contribution in the magnet bore. Due to the different geometries and shapes of the superconducting coils used for the HO corrector magnets, the variation of the differential inductance as a function of the operating current in the magnet cannot be analytically calculated or predicted for the quench protection study. The previously described

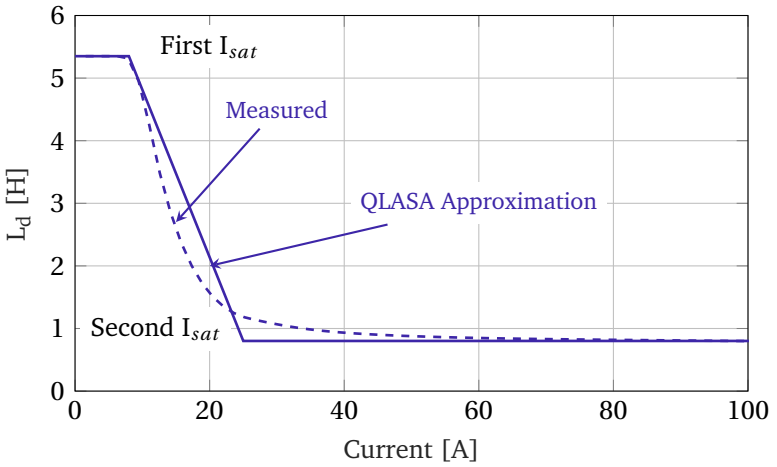

Figure 3.14: *Approximation of QLASA differential inductance of a magnet as a function of the current in the superconducting coil. The two different saturation levels are visible and are related by the γ factor previously described in Table 3.3.*

model used in QLASA is based on an approximation of the differential inductance variation considering two regimes at low current (typically below 30 A) and at high current values, see Fig. 3.14. In these two regimes, where the experimental differential inductance reaches a plateau due to the well-defined relative permeability of the iron laminations, the value simulated is kept constant as a function of the current. In the intermediate region, a linear transition from one regime to the other is supposed to simplify the simulations. However, to better describe the shape of the current decay, and calculate the real maximum voltage developed inside the superconducting magnets during the quench development, a new simulation model has been developed. To overcome the approximation on the simulated inductance of QLASA, we decided to externalize the calculation of the voltages of the coils and more in general the magnet equivalent circuit solution. The program LTSpice has been used to solve the circuit equation and coupled with QLASA software to evaluate the thermal properties of the superconducting coils which rule the temperature rising inside the magnet. The two software have been coupled using the STEAM co-simulation network frame [2] to evaluate at the same time the influence of the temperature rising in the quenched coil, and therefore the internal resistance developed by the magnet, on the current variation in the equivalent circuit. A precision model of the power supply circuit has been developed by Dr. Marco Prioli in LTSpice to evaluate the response time of the system and calibrating the model on real data acquired at the LASA test station.

3.4.1 Differential Inductance Model

The LTSpice circuit used for the simulations is composed of the external power converter coupled to the magnet, which is modeled as an equivalent quench resistance and the current dependent differential inductance, a crowbar, used to protect the power converter from the high voltages, and the external dumping resistance with the switch. Two different circuit configurations have been modeled: the first one is used to simulate the QDS of MQSXF which is closed on the external dumping resistance during the discharge. The second circuit is used to model all the quench development and QDS of all the other corrector magnets which are discharged on their internal resistance. The value of the internal resistance of the magnet is controlled by the simulation in QLASA of the quench development during the magnet discharge. The equivalent magnet differential inductance is modeled as a lumped inductive element which value is regulated by the current of the QDS system circuit. The characterization of all HO corrector differential inductance has been performed by analyzing the electromagnetic energy produced by every single magnet and simulated with 3D FEM OPERA models. The design configuration of all the HO corrector magnets, reproduced in these simulations, is the final one for the magnet series

production which details can be found in Table 3.6. By knowing the standard

TABLE 3.6.
HL-LHC HO CORRECTOR MAGNET SERIES PARAMETERS

Magnet	N Poles	Integrated Field [Tmm] R_{ref} =50 mm	I_{nom} [A]	I_{ult} [A]	E [kJ] @ I_{nom}
MQSXF	4	0.700	174	197	30.8
MCSXF	6	0.095	99	112	1.72
MCOXF	8	0.069	102	115	1.55
MCDXF	10	0.037	92	106	0.67
MCTXF	12	0.086	85	97	3.63
MCTSXF	12	0.017	84	94	0.73

definition of the differential inductance and its relationship with the magnetic flux $\Phi(B)$ linked to a single coil with an operating current I, we can write the equation:

$$V = -L_d(I)\frac{dI}{dt} \quad where \quad L_d(I) = \frac{\partial \Phi(B)}{\partial I} \tag{3.11}$$

The differential inductance takes into account the variation of the single static inductance as a function of the current due to the changing of the iron saturation of the poles of the magnet and, more in general, nonlinear dependence of the linked magnetic field flux from the current. The differential inductance can be retrieved directly from the 3D static simulations of the magnetic field of the magnet using the Eq. 3.12 if we neglect the residual iron magnetization and transient magnetization effects of the superconductor.

$$L_d(I) = \frac{1}{I}\frac{\partial E(I)}{\partial I} \tag{3.12}$$

However, the energy accuracy of the OPERA 3D model for very low values of current is not sufficient for the calculation of the differential inductance leading to oscillations and instabilities in the function. To overcome these calculation issues we can define the energy equivalent inductance as:

$$L_w(i) = \frac{2E(i)}{i^2} \tag{3.13}$$

Using this equation and replacing it in the definition of the differential inductance we obtain a simplified model which prevents the divergence of the

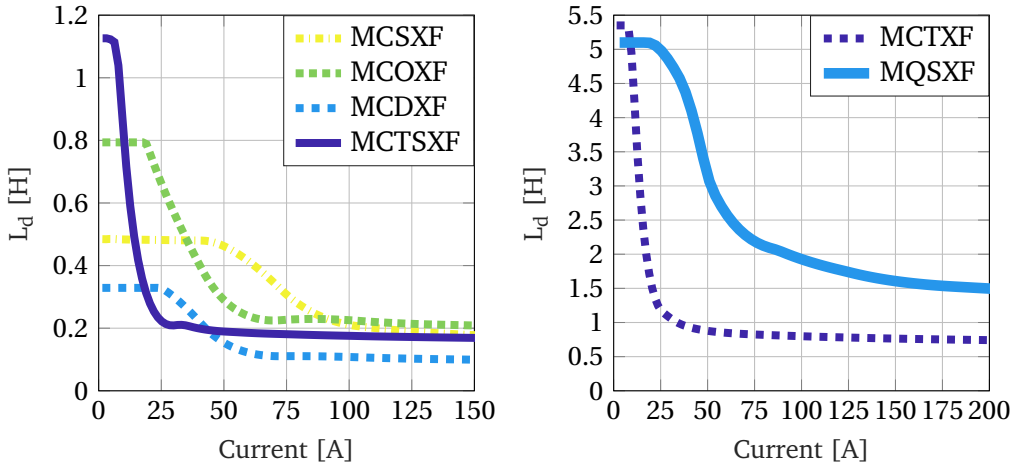

Figure 3.15: *Calculated values of the Differential Inductance of all the HL-LHC HO corrector magnets. The differential inductance of MQSXF and MCTXF (right) are greater than the short corrector magnets ones (left) due to their high values of stored electromagnetic energy and integrated magnetic field produced.*

function for low values of current.

$$L_d(i) = L_w(i) + \frac{1}{2}\frac{\partial L_w}{\partial i} i \tag{3.14}$$

The energy simulated for every single magnet by OPERA can be approximate, with very good accuracy, to a squared function of the current for low values of this parameter. As a consequence, the derivative of the energy equivalent inductance goes to zero for low values of current keeping the differential inductance fixed to a finite value. The shape of the differential inductance for all the magnets types is reported in Fig. 3.15. These values have been fitted to produce a "look at table" function inside LTSpice for the regulation of the equivalent inductance in the electrical circuit of the QDS.

3.4.2 Experimental Validation and Results

An example of the accuracy of the used model in the description of the real differential inductance of the magnet has been obtained from the test at LASA of the first skew quadrupole magnet produced in the industry. The measured differential inductance has been obtained both during the energizing test up to the ultimate current and the measured coil signals during the 14 spontaneous quench events of the magnet in the powering test [23]. The voltage applied to the total magnet during the slow ramp up and ramp down of the

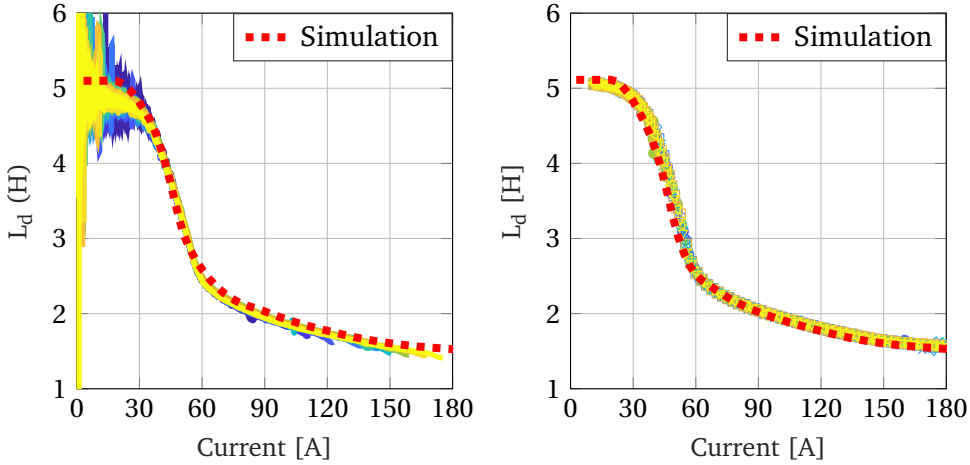

Figure 3.16: *Comparison between the simulated value of the differential inductance of MQSXF and measured data taken from LASA energizing test of the first magnet of this type. The comparison has been made with data retrieved by magnet discharge during quench propagation (left) and slow ramp up and ramp down of the magnet during energizing test (right).*

magnet can be considered not affected by high magnitude transient magnetization effect while the signal obtained during the quench development is more sensitive to dynamic effects produced by the superconducting coils. As we can see from Fig. 3.16, a very good agreement between the simulation and the experimental data has been found. However, in both the two measured data, the simulation of the differential inductance at low values of current is slightly overestimated and is probably due to the BH curve used for the magnets. Also, the consequences of possible transient magnetization effects on the superconducting coils can be seen in the measured data during the quench development. These effects, however, affect only the values of the inductance for a high range of current when the decay is faster during the quench development and can, therefore, be neglected as a first approximation in the simulation. The thermal and electrical properties of the magnet prototype previously described have been used to model also the magnet series design for the new co-simulations. The main scope of these simulations, as the quench protection analysis performed on magnet prototypes, is the evaluation of the magnet performances in case of quench events in the accelerator lattice. To evaluate the performances of the upgraded model and analyze the accuracy of the co-simulations, a reconstruction of the quench event of the previously described prototype MCTXF model, see Paragraph 3.3.5, has been performed. The results of the simulations and the comparison with the experimental data have been also reported in [38]. The agreement with simulation data is very

good and both the resistive voltage and the inductive voltage of the quenched and not quenched coils are reproduced by the simulations, see Fig. 3.17 and Fig. 3.18. This agreement with measured data has been also obtained in the description of the power converter behavior before and after the closure of the circuit on the external dumping resistance, for the skew quadrupole, and on the power supply crowbar for all the other magnets. The validated model has been used to evaluate the performances of the final design of the HO corrector magnets both at the nominal and ultimate current. The simulations of the short magnets and the normal dodecapole have been performed with a validation time of 180 ms and a voltage threshold of 200 mV. Instead, for the dedicated QDS for the skew quadrupole, the voltage threshold used has been kept fixed to 200 mV, and the validation time set to 20 ms, in agreement with CERN, to manage and assure the protection of the magnet in the accelerator lattice. The parameters of the model have been fixed to the nominal values

TABLE 3.7.
QUENCH PROTECTION RESULTS OF THE HL-LHC
HO CORRECTOR MAGNETS FINAL DESIGN

Magnet	N Poles	Nominal Current		Ultimate Current	
		T_{max} [K]	V_{gnd}^{max} [V]	T_{max} [K]	V_{gnd}^{max} [V]
MQSXF	4	101	232	116*	355*
MCSXF	6	110	49	122	63
MCOXF	8	109	51	121	73
MCDXF	10	88	21	99	33
MCTXF	12	98	101	112	145
MCTSXF	12	93	27	98	33

Notes:(*) Even if the results at nominal current are used for the evaluation of the magnet safety, the results at the ultimate current, have been obtained with the same nominal conservative configuration of RRR=100 and high packing factor of the strands in the coil cross section. From experimental data analysis, the measured value of the RRR is higher than 200 which results in values of the maximum voltage lower than the acceptable limits.

to evaluate the expected averaged performances of all the magnets that will be produced. The values of the maximum hot spot temperature and the maximum voltage to the ground are reported in Table 3.7. All the magnets' final maximum temperatures, obtained in the adiabatic approximation, are around a safe value of 100 K, compared to the maximum allowed value of 250 K, assuring no damages of the coils during a quench event. The maximum voltage to ground, at nominal current, reached by the HO corrector magnets has been

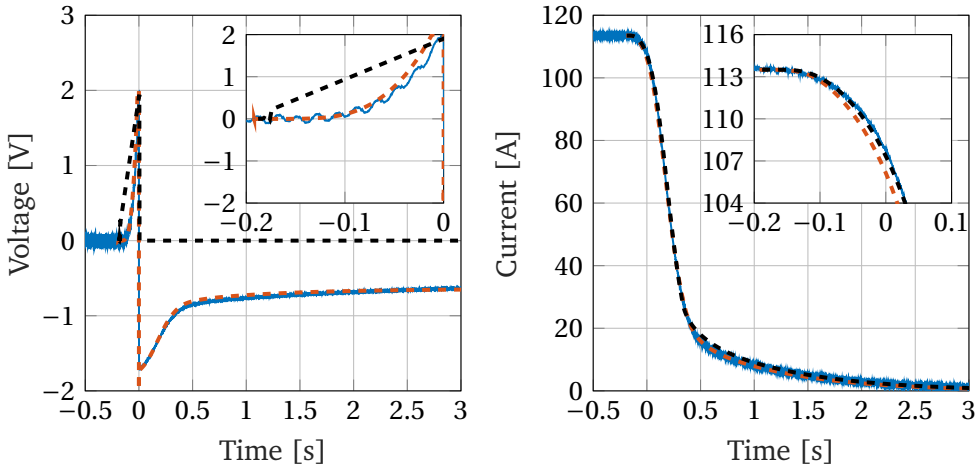

Figure 3.17: *Comparison of the experimental and simulated data of the dodecapole MCTXFP1 magnet discharge during a quench event. The behavior of the power supply total voltage (left) is reproduced very well by the simulations with the STEAM framework (red dashed line) compared to the standalone QLASA simulation (black dashed line). The current discharge (right) is instead reproduce well from both the two types of simulations.*

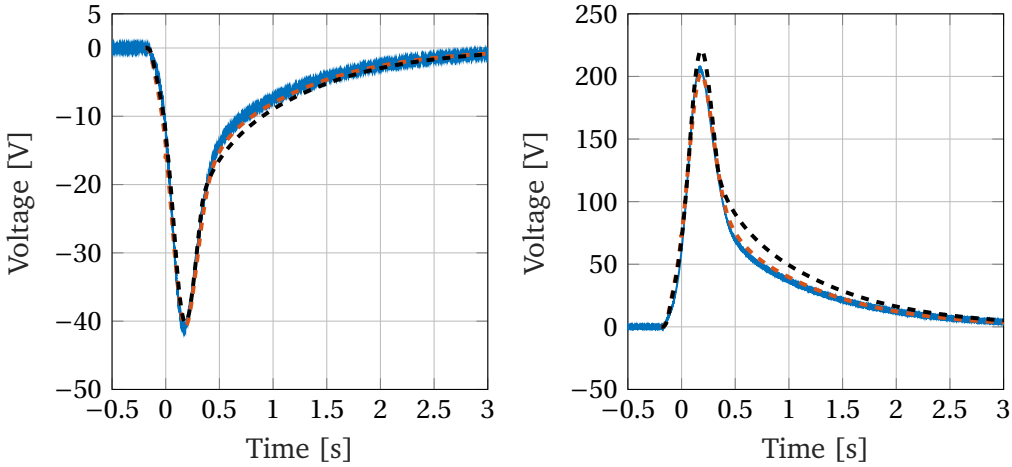

Figure 3.18: *Comparison of the experimental and simulated data of the dodecapole MCTXFP1 magnet discharge during a quench event. The behavior of the inductive voltage (left) and the quenched coil voltage (right) is reproduced very well by the simulations with the STEAM framework (red dashed line) compared to the standalone QLASA simulated data (black dashed line).*

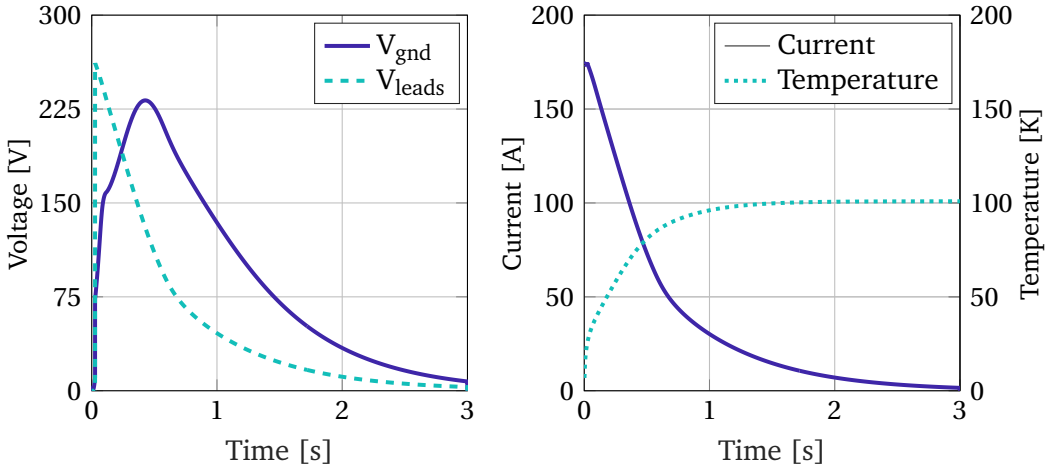

Figure 3.19: *Simulation of the skew quadrupole MQSXF maximum voltage to ground compared to the voltage between the two current leads during a quench event at nominal operation current (left). The maximum hot spot temperature and the current discharge during the same quench event are reported as function of time from quench detection (right).*

obtained for the skew quadrupole and is equal to 232 V. However, the maximum voltage inside the magnet is reached between the ends of the magnet and is equal to 261 V, see Fig. 3.19. This difference has been possible due to the balance of the grounding point which has been fixed in the middle of the external dumping resistance.

3.5 Conclusions

In this chapter, the study of the quench protection of the High Order superconducting corrector magnets has been presented. A brief introduction to superconductivity and quench propagation inside superconducting material is reported to introduce fundamentals parameters like the critical temperature or the critical current which are mandatory to explain the performances of a superconducting coil in case of a quench event. The principal methods to protect a magnet from damage during a quench development are presented and discussed focusing on the performance of the maximum temperature reached by the superconducting coil. The material properties used to model, both the prototypes and final design of the HO corrector magnets have are reported together with the description of the two different quench detection systems that are already used at LASA and that will be implemented during the installation at CERN for the protection of the magnets. A first quench protection study has

been performed on the prototype design of the magnets using the QLASA software and calculating the electromagnetic parameters of the magnets, like the differential inductance, the magnetic field map, and the total electromagnetic energy, from 3D FEM simulations performed with OPERA. Both the thermal and electromagnetic models of the superconducting magnets have been validated reproducing provoked experimental quench events in the first built prototypes of the decapole and normal dodecapole magnets. The result of the simulations, performed at the ultimate current to evaluate the maximum hot spot temperature and the maximum voltage reached during the magnet discharge, satisfies all the CERN requirements for the protection. The maximum temperature obtained from the simulations is below the allowed limit of 250 K and the maximum voltage is well below the limit of 300 V imposed to avoid shorts in the magnet. To overcome the main limitations of the QLASA software, which approximation of the magnet differential inductance variation as a function of the current is not enough to model the behavior of the magnet during a quench event, the calculation of this parameter has been externalized simulating the equivalent magnet circuit in LTSpice. The two simulation softwares have been linked together in a co-simulation using the STEAM framework developed at CERN to assure the stability of the simulation and manage the feedback of one software to the other. The differential inductance, given in LTSpice as an input parameter has been calculated with OPERA 3D simulations. The differential inductance has been also compared with data obtained from real measurements of the inductive voltage of the dodecapole MCTXF prototype coils both during quench events and during the slow ramp up and ramp down of the energizing test of the magnet. The comparison of the data with the simulated curve shows a very good agreement with some little differences in the value of the differential inductance at low current values, probably due to different magnetic properties of the iron used in the simulation from the real one adopted for the construction. The co-simulation between QLASA and LTSpice has been validated on measured data of the quench events of the prototype of the normal configuration. The co-simulations have been performed for all the High Order corrector magnets series configuration and the results have been reported. All the magnets satisfy the quench protection requirements to be protected during the operation in the LHC lattice.

Chapter 4

Quench Localization through Magnetic Measurements

4.1 Introduction

In this chapter, a novel type of superconducting magnet quench localization study has been carried on based on the measurement of the magnetic field produced immediately after a magnet discharge, due to the quench development and propagation. Thanks to this newly developed method we can locate the position of the quenched coil inside an n-order magnet by analyzing the influence of the superconducting coil magnetization on the magnetic field quality in the bore area. The problem of the quench localization inside superconducting magnets has become, in the last few years, one of the main aspects that have to be solved for the construction of a superconducting magnet. Many different measurement methods have been developed, in the last 30 years to evaluate the position and precisely determine the starting time of a quench event in a superconducting coil. The basic method to evaluate the position of the quench event in a superconducting magnet is the use of voltage taps connected to different points of the coils. By performing a differential measurement on the signals of identical superconducting coils, the main resistive voltage can be isolated and the corresponding quenched coil can be pointed out. However, the spatial resolution of this method is fixed with the position of each single voltage taps and the differential measurement signal has often to be compensated to account for possible intrinsic differences in the coil geometries and performances. During the prototype development phase of a superconducting magnet, the number of voltage taps instrumented on a single superconducting coil is as high as possible to allow detailed analysis of the quench development inside the material. For the construction and test of series magnets this approach is not suitable and other methods, to identify the location of the quench inside superconducting coils, have been developed. The number of voltage taps required for the quench protection system, during the energizing tests and final operation of the High Order corrector series magnets, has been fixed to 3 (2 at the ends of the magnet and one in the middle) to have the total voltage and the signals of every single half of the magnet. The reduction of the number of voltage taps has not affected the possibility to

detect the quench development in the magnet through the differential analysis of the two magnet halves signals. However, it can no longer be detected which coil has quenched inside the magnet. One of the most sensitive methods for the quench detection and localization inside superconducting magnets is the use of "*Quench Antenna*". This particular device is composed of different pickup coils optimized to evaluate and detect any field perturbation inside the bore of a magnet. The quench antenna is principally used to detect the perturbation generated by current redistribution inside the superconducting cable of the coil. Analyzing the variation of the signal induced on the quench antenna with high-frequency sampling rates, the detection and the localization of the quench front propagation is possible. The main problem that has to be solved in quench antenna is the suppression of the noise of the signal induced in the pickup coils which can be created by external sources of error, like ripples in the magnet power supply. To compensate for the source of errors and improve the accuracy of the measurements, usually, a combination of different pickup coil is used. Usually, the configuration of the different pickup coils, used mainly to study superconducting dipoles and quadrupoles, has a higher order of rotational symmetry compared to the magnet order to not be affected by the fluctuations of the magnet current. To restore the possibility of quench localization inside the HL-LHC High order corrector magnet series, the development of a dedicated quench antenna is not suitable. The different orders of the produced magnets, from 2 to 6, would require the development of dedicated designs of quench antennas with optimized and very high rotational symmetry orders, losing efficiency and increasing the complexity of the device. The here proposed solution to this problem involves the same magnetic field measurement system used for the characterization of the magnetic field quality which has been already presented in Chapter 2 and specifically developed for the HO corrector magnets.

4.1.1 Chapter Structure

The first experimental evidence of the superconducting magnetization influence, of the not quenched coils in the magnet, has been observed in the shape of the residual magnetic field sampled by the rotating coil in the magnet. We observed that the shape of the residual magnetic field, as a function of the rotation angle and produced at zero current, is different if the magnet is brought to rest with a slow ramp down or a quench event provokes the magnet fast discharge. This difference is caused by the superconducting not quenched coil magnetization which becomes the main contribution to the residual magnetic field at the magnet rest. Only the quenched coil in the magnet has no residual

magnetization and therefore introduces an asymmetry of the produced residual magnetic field in the magnet bore. From the analysis of the residual magnetic field shape, we can identify the quenched coil inside the magnet. Firstly, to reproduce the experimental residual magnetic field sampled by the rotating coil system after a quench event, an analytical model has been developed based on the calculation of the coil magnetization. This model is used to evaluate if the difference between the residual magnetic field obtained after a quench event and after a slow ramp-down to zero current is due to a single quenched coil or not. Secondly, a FEM 2D model has been used to evaluate how the coil magnetization contribution in the residual magnetic field is affected by the iron lamination permeability. The simulated residual flux has a shape close to the experimental data obtained after a quench event. However, to fit the amplitude of the measured signal, the iron contribution of the model needs to be scaled giving evidence that its contribution depends on the current discharge rate. This particular behavior of the iron residual magnetization has not been found specifically in literature, see [39], and only the losses induced in the material are always studied as a function of the current discharge rate, [40]. To verify this behavior and reproduce the experimental signals, an analysis of the iron magnetic properties has been performed finding two different configurations of the model whose results are in agreement with the data after a quench event and after a slow ramp down to zero current. Even if the obtained results have been very promising, an improved analysis method to immediately identify the quenched coil inside the magnet has been developed, see Sect. 4.5, based on the harmonics of the residual magnetic field flux sampled by the rotating coil. In this second developed method, the non-allowed harmonics are measured and compared with simulated values as a direct effect of the quenched coil inside the magnet. Analyzing the phase of the non-allowed harmonics and combining the different orders created, the position of the quenched coil can be resumed and its portion in the corresponding half of the magnet can be compared with the QDS detection system voltages. The comparison on different quench events that occurred in the first tested HO corrector series magnets is reported observing that the new method is very accurate and can increase the diagnostic of the test station system developed at LASA.

4.2 Experimental Data

The first hint of the possibility to detect the superconductor magnetization effect in the residual field after a quench event has been observed with the magnetic characterization of the quadrupole MQSXFP1b assembly performed at LASA in the vertical cryostat. During the magnetic field quality analysis of the magnet, the residual magnetic field produced at zero current has been sampled and analyzed with the temporary rotating coil. In particular, the main

observed anomaly in the acquired data has been obtained by the comparison between the magnetic field produced at rest during the powering cycle and the residual magnetic field after a magnet fast discharge due to the quench development. The main experimental data which has been investigated is the incremental magnetic field flux produced at the external radius of the PCB coils shaft during the rotation. The incremental field flux is retrieved by measuring the induced voltage on the external coil (coil-A) of the shaft which is then sampled in N_{index} =512 steps/turn by the motor unit encoder board. The sampling process can be written as follows:

$$\Delta\Phi_i = \int_{t_i}^{t_i+dt} -V\,dt = \int_{t_i}^{t_i+dt} \frac{d\Phi}{dt}\,dt \tag{4.1}$$

Each of the indexed flux differences is calculated in a fixed time step which can be converted to a fixed angular step using a constant angular velocity in the shaft rotation, which in our case is equal to 1 Hz. We can rewrite the Eq. 4.1 as:

$$\Delta\Phi_i = \int_{t_i}^{t_i+dt} \frac{d\Phi}{d\phi}\frac{d\phi}{dt} = \int_{\phi_i}^{\phi_i+d\phi} \frac{d\Phi}{d\phi}\,d\phi \tag{4.2}$$

Using the definition of the magnetic field flux and considering that the rotating shaft can only sample the azimuthal flux produced in the magnet bore we can describe the flux as:

$$\Phi = \int_{R_1}^{R_2}\int_{L} B_\phi\,dr\,dl\,N_{turn} \tag{4.3}$$

where L is the length of the rectangular coil invested by the magnetic field, R_1 =37 mm and R_2 =47 mm the positions respect the rotating axis of the external coil sides and N_{turn} the turn number of the coil placed at the average radius R_{av} =42 mm. We can substitute the Eq. 4.3 into the integration and use the solenoidal behavior of the magnetic vector field to modify the angular derivative of the tangential magnetic field component.

$$\Delta\Phi_i = \int_{\phi_i}^{\phi_i+d\phi}\int_{R_1}^{R_2}\int_{L} \frac{dB_\phi}{d\phi}\,dr\,dl\,N_{turn}\,d\phi \tag{4.4}$$

$$\text{Using } \nabla\cdot B = 0 \rightarrow \frac{d(rB_r)}{dr} + \frac{d(B_\phi)}{d\phi} + \frac{d(B_z)}{dz}$$

Considering that the integration along the rotational axis is performed over the whole magnet length and the symmetry of the magnetic field compared to the xy plane, we can cancel the z-derivative and consider only the radial and tangential component obtaining the following equation:

$$\Delta\Phi_i = \int_{\phi_i}^{\phi_i+d\phi} \int_{R_1}^{R_2} \int_L -\frac{d(rB_r)}{dr} dr dl N_{turn} d\phi \tag{4.5}$$

Solving the integration along the radial direction of the magnet we obtain:

$$\Delta\Phi_i = \int_{\phi_i}^{\phi_i+d\phi} \int_L (R_1 B_r(R_1) - R_2 B_r(R_2)) dl N_{turn} d\phi \tag{4.6}$$

The integration of the radial component of the magnetic field is performed over all the coil length L_{Coil} but the geometric length of the magnet, equal to 540.4 mm, is less than the real shaft coil length and the magnetic field decreases towards the end of the magnet. Therefore, to compare the 3D measured flux with the 2D FEM simulations we can use the definition of the magnetic length and rewrite the Eq. 4.6 with the radial magnetic field calculated in the magnet cross-section, which is assumed constant compared to the z-axis, multiplied by the magnetic length L_{magn}.

$$\Delta\Phi_i = \int_{\phi_i}^{\phi_i+d\phi} (R_1 B_r(R_1) - R_2 B_r(R_2)) L_{magn} N_{turn} d\phi \tag{4.7}$$

The length of the angular step can be calculated as $\Delta\phi = 2\pi / N_{index}$. Assuming a linear approximation with the angle of the integral argument in each angular step, we can use the trapezoidal integration method and obtain the flux difference as:

$$\Delta\Phi_i = (R_1 B_{r_i}(R_1) - R_2 B_{r_i}(R_2)) L_{magn} N_{turn} \Delta\phi \tag{4.8}$$

Where each B_{r_i} is calculated at the averaged angle of each i-indexed angular step. The calibrated parameters of the shaft are the radial position of each coil side and the effective area of each coil of the PCB which are linked to the number of turn of the coil by the following equation:

$$A_{eff} = L_{coil} N_{turn} \Delta R \tag{4.9}$$

Using the Eq. 4.9 we can define the final incremental field flux equation as a function of the calibrated parameters of the coil and simulated values of the magnetic field.

$$\Delta\Phi_i = (R_1 B_{r_i}(R_1) - R_2 B_{r_i}(R_2)) \frac{L_{magn}}{L_{coil}} \frac{A_{eff}}{\Delta R} \Delta\phi \tag{4.10}$$

The comparison between the measured incremental field flux, obtained after a quench event, and the one obtained at zero current at the end of different powering pathways of the magnet is reported in Fig. 4.1. All these signals have to be filtered accounting for the presence of the residual earth dipole magnetic

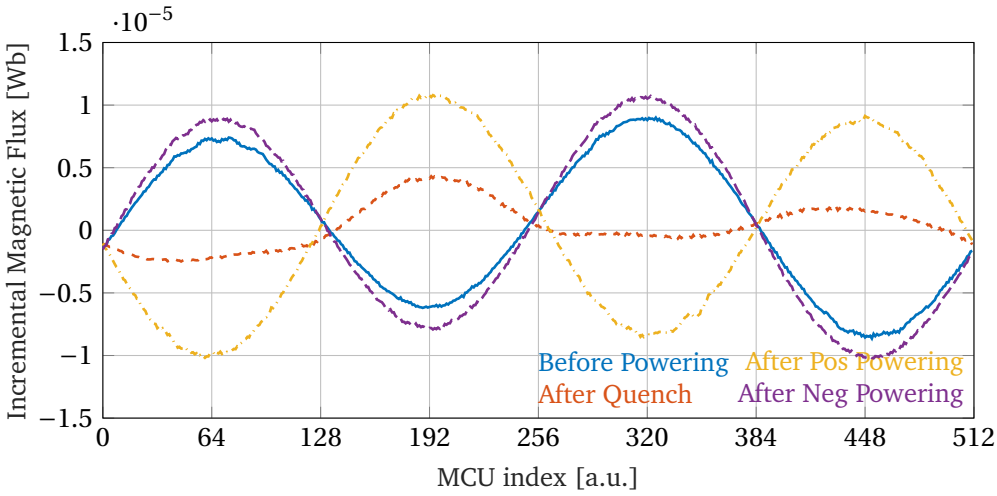

Figure 4.1: *Measured signals obtained by the external PCB on the coil shaft at different conditions during the quadrupole prototype powering test. On the x-axis, we reported the angular index of the Motor Control Unit (MCU) used to divide 360° rotation along the rotational axis of the magnet.*

field, measured in the portion of the shaft outside the magnet, and a possible centering error of the measuring PCB shaft in the prototype magnetic axis. These two contributions have been calculated by subtracting the residual incremental magnet flux produced at zero current at the two opposite points of

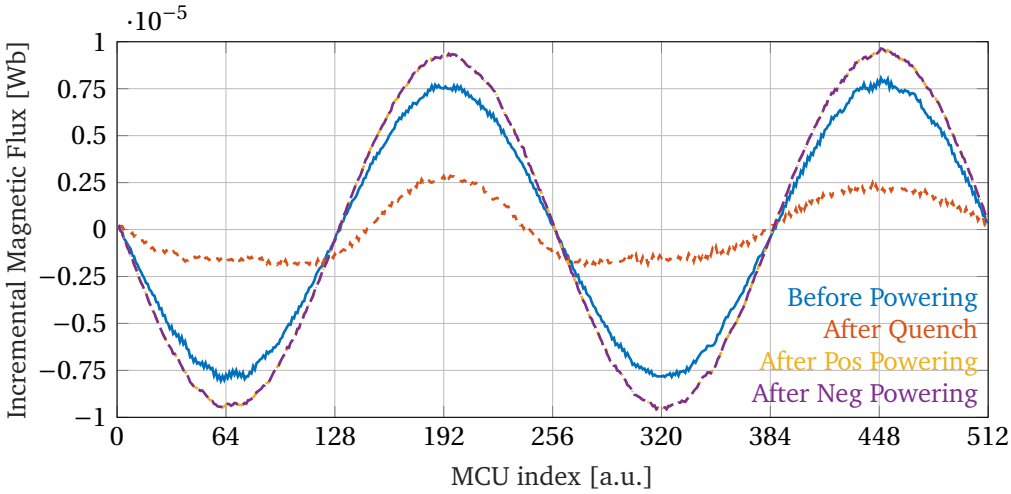

Figure 4.2: *The filtered signals have been obtained after the evaluation of the earth dipole contribution to the measured flux of the PCB shaft. All the measured signals, except for the one, measured after magnet quench, show a quadrupole symmetry.*

the magnetic measurement powering cycle. The field produced by the magnet in the two cases changes its sign but all other contributions remain equal. The calculated filtered signals are reported in Fig. 4.2. The residual magnetic field has been evaluated, first of all, before the magnet cool-down in the fourth run of the MQXFP1b test session and this signal has been also compared with the residual magnetic field produced at 4.2 K. No evidence of field enhancement is seen in the comparison between these two conditions suggesting that thermal contractions of the iron do not affect the intensity of the residual magnetic field in the bore. The measure taken before the magnet powering has been compared to the amount of flux produced after the slow ramp-up from -I_{ult} to zero during the magnetic measurement cycle. Both these signals have been reflected in the y-direction to be compared with the signal taken after the ramp-down from the positive current. The incremental flux measured after the slow ramp is slightly higher than the first measurement before powering and the difference has been considered as the effect of the combination of the iron magnetization, during the slow ramp, and the residual superconducting wire magnetization contribution. In the analysis, the incremental flux produced after a quench transition of the magnet, the red dotted line in Fig. 4.2, has been also compared to the flux produced at zero current after the slow ramp down during the magnetic measurement cycle. These two signals have completely different shapes and the amplitude of the first one is less than half of the second one. Possible explanations of this difference have to be found in the hysteresis magnetization process of the iron and the residual superconductor magnetization of the non-quenched coils. Thanks to additional measurements of the relative positioning of the shaft in the magnet system frame, we managed to identify the quenched coil position and calculate the initial angular position of the shaft in the magnet reference frame. The amplitude difference, visible between the different signals, has been studied trying to reproduce the magnetization contribution of the superconducting material and evaluate how the shape of the residual incremental magnetic field flux is affected by the quench of one of the coils.

4.3 Superconducting Coil Magnetization Contribution

4.3.1 Analytical Model

As the first step, we tried to reproduce analytically this type of contribution, to study its behavior and the compatibility with the measurements previously described. As a first approximation, the superconducting magnetization contributions of every single coil have been described by two equivalent magnetic dipoles, one for each coil side in the cross-section of the magnet. We assigned the direction of this dipolar magnetization according to the one of the average

magnetic field induction produced on the whole coil area at low current. The superconductor strand magnetization is calculated considering the scalar Bean model [41] based on the following equation:

$$M = \frac{2}{3\pi} J_c d_f \lambda \lambda_c \qquad \text{or equivalent} \qquad M = \frac{2}{3\pi} J_c D_w \frac{\lambda^{3/2}}{\sqrt{N_f}} \lambda_c \tag{4.11}$$

where J_c is the critical current density, d_f the wire filament diameter, λ is the superconductor to strand volume ratio, λ_c the ratio between the area of all strands and the whole coil area, N_f the number of filaments in the strands and D_w the wire diameter. The critical current density has been fitted on measured data using the Kim-Anderson model [42], [43] described by the equation:

$$J_c(B) = \frac{J_0 B_0}{B + B_0} + A_0 + A_1 \cdot B \tag{4.12}$$

The parameters of the model, used in all the simulations presented in this report and which better describe the experimental data measured on a NbTi wire sample, can be found in Table 4.1. This magnetization value, with its

TABLE 4.1.
KIM-ANDERSON MODEL PARAMETERS

Parameter	J_0	B_0	A_0	A_1
Unit	A/mm^2	T	A/mm^2	A/Tmm^2
Value	2.92E+04	0.1203	5.97E+03	-7.0E+02

dependence on the magnetic field B, has been integrated into the coil area and scaled to take into account the presence of insulation. The averaged magnetization value is then used to calculate the module of the equivalent dipole used to describe each coil side in the model. To reproduce the residual measured incremental flux after the positive powering, we considered the experimental signal obtained before the powering (i.e. the iron contribution only), the blue line in Fig. 4.3, and added the analytically calculated magnetized coils contribution.

Comparing the result with the measured signal, we can observe that the obtained amplitude of the analytical simulation is lower than the experimental curve obtained after the magnet energization. Indeed, the orientation of the magnetized dipoles along the quadrupolar magnetic field lines produces an overall negative contribution to the residual field which is opposed to the iron residual magnetization field flux. In the other different situation, to reproduce

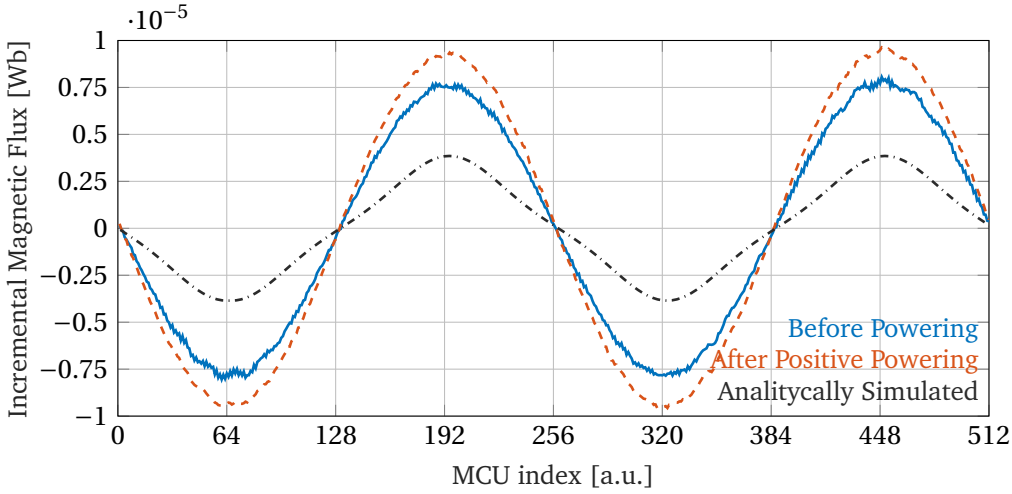

Figure 4.3: *Comparison between the measured signal of the incremental field flux after the ramp down at zero current with the analytical reconstruction of the supposed incremental flux produced by the superconducting magnetized coils.*

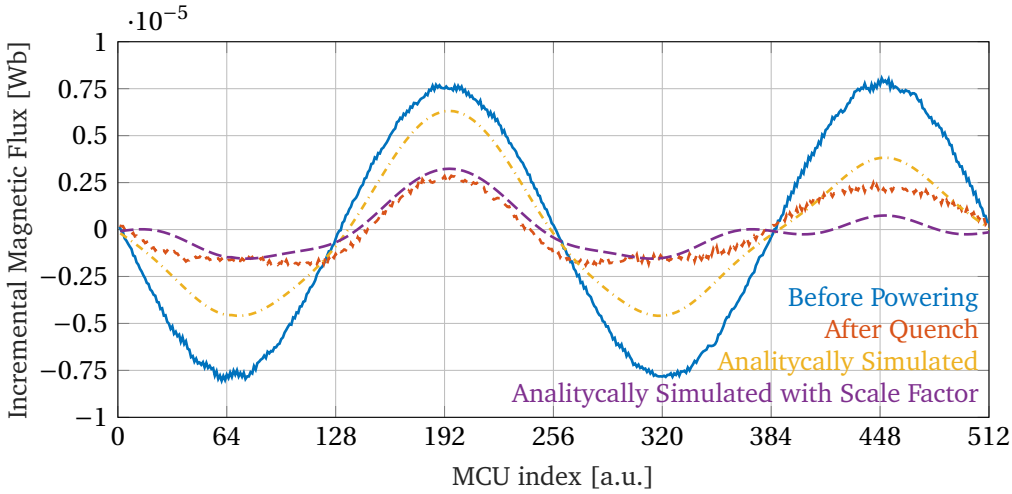

Figure 4.4: *Comparison between the measured signal of incremental flux after the magnet fast discharge, due to the quench development, and the analytical reconstruction of the supposed incremental flux. The additional analytically reconstructed shape with the reduced scale factor has a lower amplitude than the first analytically simulated one and is more compatible with the measured data.*

the measured data after the quench, we always considered as a starting point the measured flux before powering (dominated by the iron contribution) and neglected the magnetization of the first coil, adding to it only the contributions of the remaining three coils. The signal obtained is compared, see Fig. 4.4, with

the measured data after the quench event. Also, in this case, we observe that the magnetic incremental flux produced by the iron is reduced because we add the contribution of the magnetized coils: however, the strength of the magnetization is not enough to reach the level of the measured signal after the quench. We performed different attempts, in which the magnetization strength of the superconducting coils has been amplified by scale factors, but the amplitude of the residual incremental flux remained in disagreement with the experimental incremental flux obtained after the quench. Therefore, considering also the case after the positive powering, we tried to change the strength of the residual incremental flux produced by the iron applying a 30% scale factor to the measured signal before the powering. The new shape analytically calculated with this scale factor is reported in Fig. 4.4 and compared with the previous one. The amplitude of the calculated signal is more compatible than the previous one with the measured data but the shape of the two functions remains different. Because the effect of the iron permeability on the flux produced by the magnetized superconducting coil is not taken into account in this analytical analysis (the contribution of the magnetic coil dipoles is simply added to the problem but we know that the iron contribution may vary), we decided to simulate it using a 2D FEM model of the MQXFP1b magnet.

4.3.2 FEM Model

Focusing on the iron residual magnetization, to study the large differences between the analytically calculated residual incremental flux and the measured one after the positive powering of the magnet, we supposed that the residual magnetic incremental flux produced only by the iron is not equal if the transition from nominal current to zero is made up by a slow ramp down or by a fast discharge during the quench event. First of all, we decided to reproduce different levels of iron residual incremental flux using Opera2D FEM simulations instead of reusing the measured iron magnetization signal and add to it the superconducting coil magnetization. Starting from the classical cross-section configuration of the MQSXFP1b prototype, see Fig. 4.5 on the left, we replaced the superconducting coils (which in our analysis have zero current) with the cross-section of two closed loops, one perpendicular to the other and centered, which can be tuned to set the direction and strength of the equivalent dipole and describe the superconducting coil magnetization. The direction of the dipoles has been set according to the average magnetic field strength over the superconducting coil cross-section at low values of the operating current. Initially, to reproduce the iron contribution for the residual magnetization, a small current was set in MQSXFP1b FEM simulation to obtain the same amount of magnetic field incremental flux inside the magnet bore, as calculated according to Eq. 4.10 as the one measured by the rotating shaft

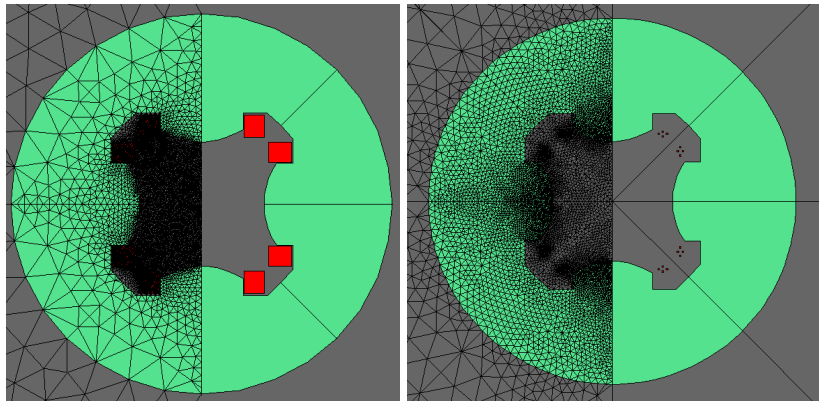

Figure 4.5: *Representation of the MQSXFP1b 2D Model used in Opera for the evaluation of the magnetization effect on the residual incremental flux produced at zero current.*

before the magnet energization. Finally, to reconstruct the measured magnetic field incremental flux produced after the fast discharge, the same technique of the analytically simulated model has been used. Consequently, the simulated incremental flux is made up of two parts: the magnetic field incremental flux produced by the magnetization dipoles simulated in the 2D FEM analysis, now with the non-linear effect of the iron permeability on it, and the experimental residual incremental flux produced before the magnet energization. Also for this approach, it turned out that the second contribution, used to describe the residual iron magnetization after the fast discharge, needs to be multiplied by a scaling factor equal to 0.3 to reach the same amplitude of the measured one after the quench. This scaling factor suggests, that the real contribution after the fast discharge is much lower than the one measured after the slow ramp at zero current or before the magnet powering and that a hysteretic behavior of the iron lamination has to be taken into account in the analysis. However, as we expected, all the iron hysteretic models in the literature, see for example [39], predict that the hysteretic loop width is proportional to the current decay rate which is in contrast with the observed behavior of the residual magnetic field produced. Only a few anomalous behaviors, in agreement with our observed one, have been found in literature, [40], and are strongly dependent on the properties of the material studied. The positioning and the dimensions of the magnetization dipoles, used to describe the superconducting coil behavior inside the model, have been translated and rotated to study the effect on the produced residual magnetic field incremental flux. However, the obtained results show that the dimension of the equivalent dipole coil does not affect the shape or intensity of the simulated incremental flux. Instead, changing the position of the dipole center introduces different rotational harmonics in the produced magnetic incremental flux, which however is not very significant to

improve the adherence with experimental data. An important parameter in the 2D FEM simulations resulted to be the magnetic permeability of the iron lamination. The BH curve used to model the performance of the magnet for all its load lines, presents, at low values of magnetic field strength, a constant magnetic permeability equal to $\mu_r = 3939$ due to a linear extrapolation from the lowest point available in the BH table. However, real experimental data obtained from the first magnetization curve of tested ARMCO Pure Iron lamination for the HL-LHC upgrade project, as reported in [44], demonstrate that the magnetic permeability shows a narrow peak around 1700 for magnetic field strength of 300 A/m and may decrease to the unit for lower values. Also, using the raw values reported in [45], we compared the behavior of the BH curves used for the simulations with the ones obtained experimentally, see Fig. 4.6 and Fig. 4.7. Due to the absence of sampled data for very low magnetic field strength, which is the regime we expect for the characterization of the iron at zero current, we can suppose that the real value of the iron relative permeability at the very low field may vary considerably in a probable range between 1 and 300. Consequently, we decided to evaluate the sensitivity of the simulations considering different magnitudes of the relative permeability at zero current, starting from a minimum value of 1, kept constant in the simulation. Using again the magnetic incremental flux measured before the

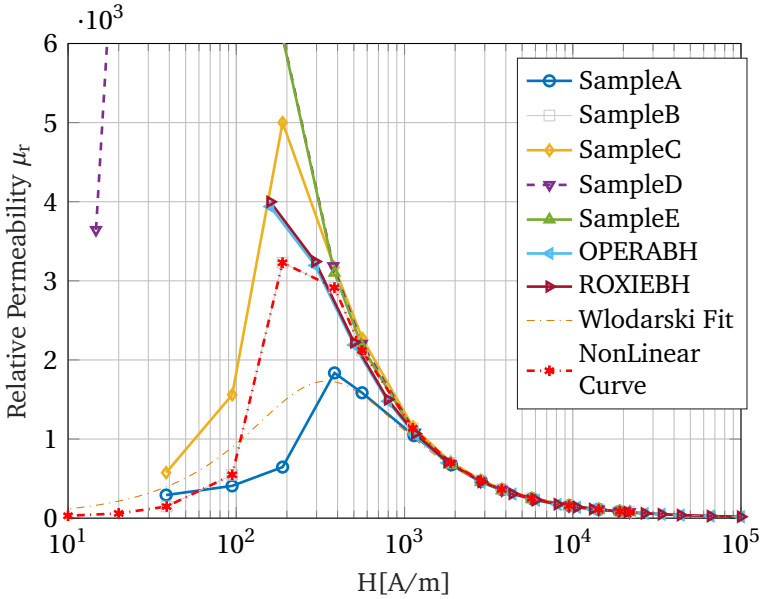

Figure 4.6: *Comparison between the measured BH curves of ARMCO Iron samples taken from the furniture for the HL-LHC upgrade project and the BH curves used in the 2D FEM model to describe the MQSXFP1b iron properties.*

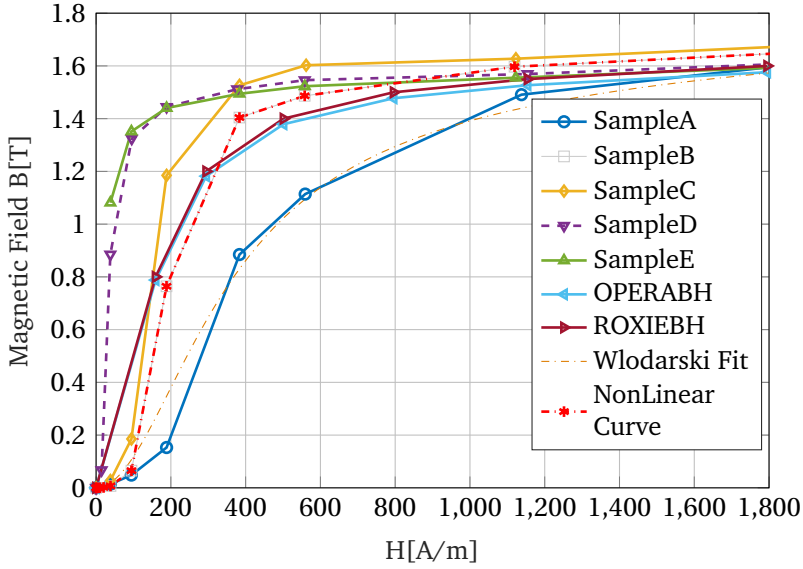

Figure 4.7: *Comparison between the measured BH curves of ARMCO Iron samples and BH curve used as input for FEM modeling. The comparison is performed on the relative permeability value, obtained from the BH curves, in which the behavior at low values of the magnetic field strength H [A/m] is visible.*

powering, scaled with the 0.3 factor, we added the contribution of the superconducting magnetization obtained from simulations with the different levels of magnetic permeability, to obtain the simulated residual magnetic incremental flux after the quench development. In the used model again the quench development has been considered limited to one superconducting coil which at the end of the magnet discharge results completely demagnetized. The results of the obtained simulations are reported in Fig. 4.8 and compared to the measured incremental flux. From the comparison, we can observe that the measured incremental flux after the fast discharge is compatible with a single quenched coil inside the magnet. This result is also in agreement with the measured voltages signals taken at the ends of each magnet coil for the quench protection system which always show a resistance development limited to one single superconducting coil, see Chapter 3. The calculated data, using low values of relative magnetic permeability, show a smaller amplitude of magnetic flux compared to the experimental curve but for values higher than 125, the amplitude starts to saturate and only small variations in the curve shape are visible. To increase the accuracy of the simulations, we created two different iron BH curves, using the experimental data and the Wlodarski Fit obtained in [45] and [44]. Simulations performed with the non-linear BH curve retrieved have the same amplitude as the curves obtained from simulations in

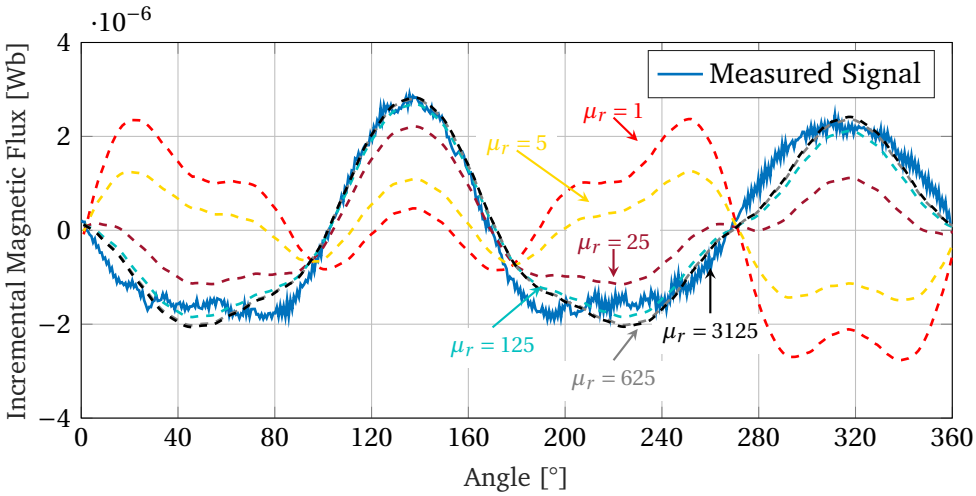

Figure 4.8: *The simulated residual magnetic incremental flux, obtained with a different constant relative permeability of iron, is compared to the experimental curve obtained after the quench propagation and magnet discharge. The comparison shows the compatibility of the simulation considering the quenched coil at an angle of 135° in the magnetic measurement system frame.*

which a high constant relative permeability value has been considered. Experimental data is compatible with the results, see Fig. 4.9, obtained from the

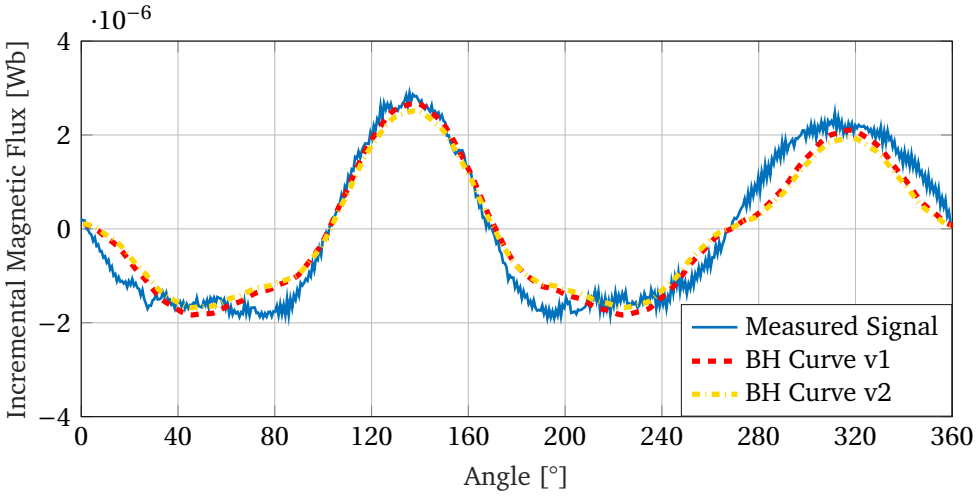

Figure 4.9: *The simulated residual magnetic incremental flux, obtained using the new BH non-linear curve, is reported and compared with the measured signal after the quench development and magnet discharge. The difference between the two BH curves is the value of the permeability at low magnetic field strength.*

simulations but the shape of the measured flux at the angular position opposite of the quenched coil (high values of angle from the zero position) is more flat compared to the one obtained from Opera2D. Additional simulations have been performed keeping the new BH curve to evaluate the influence of the superconducting magnetization on the calculated flux shape. Curves obtained from different simulations, performed by applying a scaling factor to the amplitude of the superconducting magnetization, are reported in Fig. 4.10. The value of M_0 is used for the superconducting magnetization obtained from

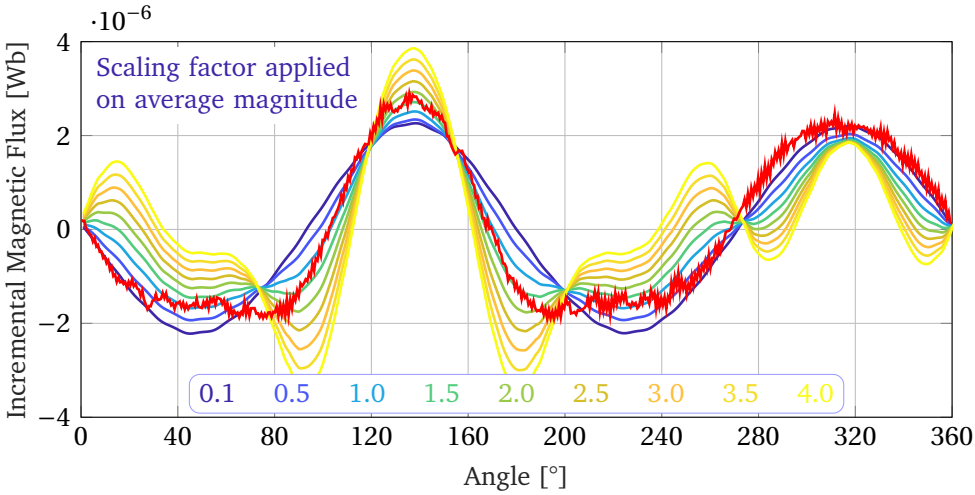

Figure 4.10: *Different simulations of the residual magnetic incremental flux obtained using a non-linear BH curve and scale factors applied to the average magnetization level of the superconducting coil to evaluate the possible effect in the shape of the incremental flux. The simulation is then compared with the measured signal after the quench development and magnet discharge but no general improvement has been obtained from the single simulations with the non-linear BH curve.*

Eq. 4.12 with the J_c fit obtained by the Anderson curve whose parameters are reported in Table 4.1. We can observe that the amplitude of the flux calculated at angles around 135° increases with higher values of magnetization and the shape of the peak becomes sharper. With the scaling of the averaged magnetization, higher-order of harmonics and oscillations appear in the calculated incremental flux spectrum which is not compatible with the measured curve. Also, the flat shape obtained in the measured curve for high angles cannot be reproduced obtaining a sharper and lower amplitude peak for higher values of magnetization. Considering the two different entities, the superconducting magnetization and the experimental incremental flux, measured before the magnet powering, which combine to form the reported calculated flux curves, we decided to improve the description of the second contribution searching for

a possible explanation of the 0.3 scaling factor used previously for the modeling of the iron residual magnetization behavior.

4.4 Residual Iron Magnetization Contribution

During the magnetic measurements of the MQSXFP1b, a residual quadrupolar magnetic field at zero current has been observed in the measured data. From the analysis of the two rest conditions described in the previous section, the first one obtained from a fast discharge due to a quench event and the second obtained at the end of a slow ramp-down of the magnet, the residual magnetic field of the iron seems to vary with the decay rate of magnet current from the operating value. We tried to reproduce the iron residual magnetization setting a permanent magnet in the 2D simulation already described. Considering a closed magnetic flux loop around two cross-sections of near coils and imposing the conservation of the magnetic flux we can calculate the load line of the permanent magnet fixing its height and width. We considered different permanent magnet configurations, see Fig. 4.11, and evaluated the shape of the flux produced in the magnet bore with zero current flow in the superconducting coils. The best configuration obtained has been created with 4 identical slabs in the cross-section of the iron poles whose direction of magnetization resembles the lines of a quadrupole magnetic vector field and the 4 iron yoke return path which have been converted to the permanent magnet material, see Fig. 4.11 cross-section on the right. By fixing the height and width of the magnetized slabs, we considered different BH curves to fit the magnetic flux measured before the magnet power. These curves have been produced using the Wlodarski equation for magnetization hysteresis loops [46] with the same parameters used in [44] for the fitting of the first BH magnetization curve.

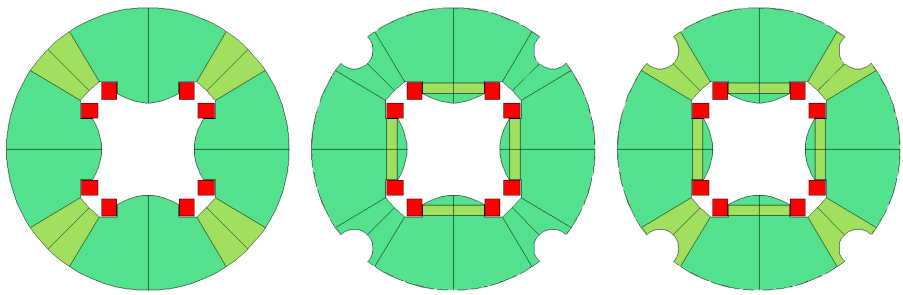

Figure 4.11: *Different configurations used to model the residual iron magnetization. Parameters of the different permanent magnet configurations are tuned to replicate the magnetic flux measured before the magnet energization. Light green is used to highlight the position of the permanent magnets used in the simulation while dark green is used to describe the iron lamination of the magnet.*

The only free parameter, used to change the BH curve of the hysteresis loop, is the coercive magnetic field strength H_c, see Fig. 4.12. The superconducting

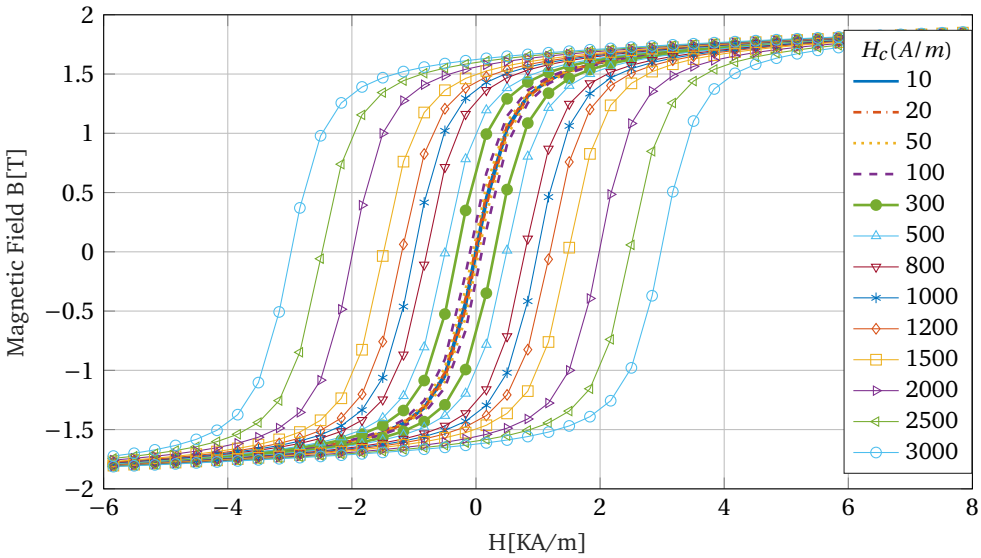

Figure 4.12: *Hysteretic BH curves obtained from the Wlodarski fit of the first magnetization curve and upgraded to the hysteretic model, see [46]. The values of the coercive field H_c [A/m] used for each curve are reported in the legend.*

coils have again been replaced by the equivalent dipoles in the 2D FEM simulations to reproduce also the superconducting coil magnetization effect. We considered the same configurations used in the previous analysis to reproduce both the measured flux produced before magnet powering and after the slow ramp-down using an H_c=800 A/m. The results of the simulations are reported in Fig. 4.13. We can observe that having tuned the coercive field of the magnetized slabs to reproduce the measured flux before the magnet power, the added contribution of the superconducting magnetization, dashed line in Fig. 4.13, does not reproduce the measured curve after the slow ramp rate at zero current which amplitude is higher than the simulated one. The following simulations, in which the magnetization of the superconducting coils has been increased by different scaling factors, see Fig. 4.14, have not shown further improvement suggesting that the disagreement between simulation data and measured one, as already seen in the analytical model of Section Sect. 4.3, has to be due to iron residual magnetization level. Indeed, using the same BH curve for the magnetized slabs and adding the superconducting magnetization to reproduce the quenched configuration, the amplitude of the incremental flux increases instead of scaling down to the same level as the measured one after the fast discharge. Focusing on the quenched configuration, we firstly

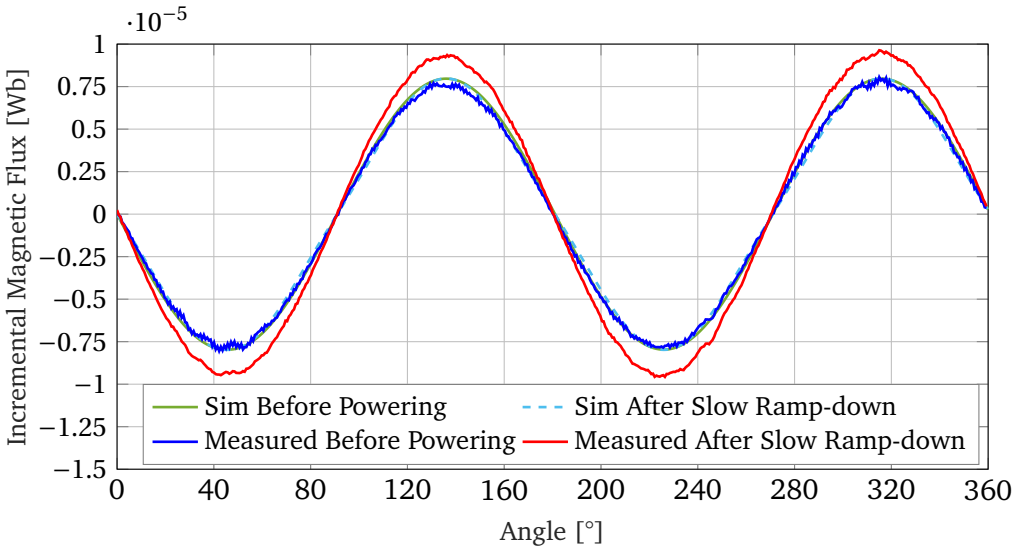

Figure 4.13: *Calculated incremental flux by complete 2D FEM simulations compared to the flux measured after the magnet slow ramp-down from the positive current state and before the magnet powering.*

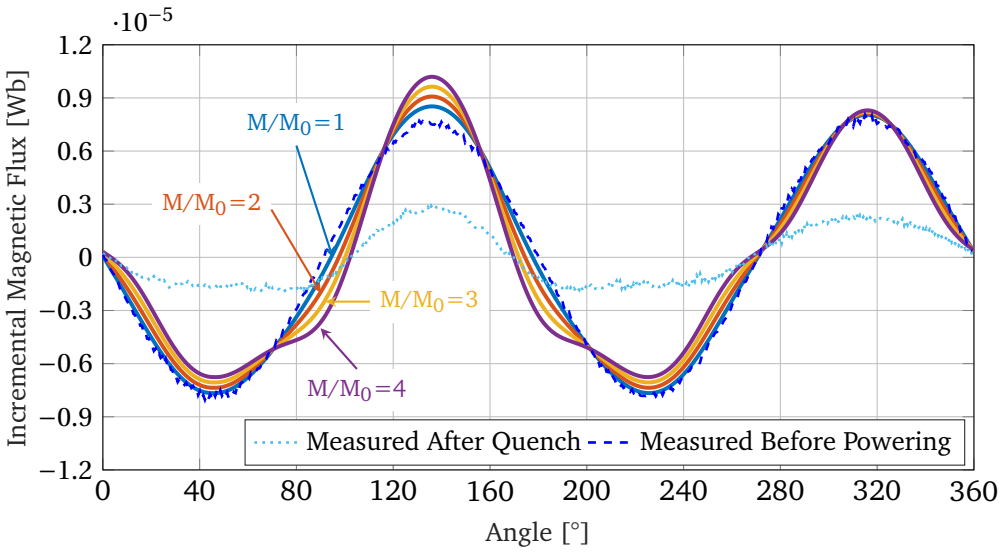

Figure 4.14: *Calculated flux by complete 2D FEM simulations compared to the flux measured after the magnet fast discharge due to the quench protection system. The quenched coil is highlighted and different levels of superconducting magnetization are exploited.*

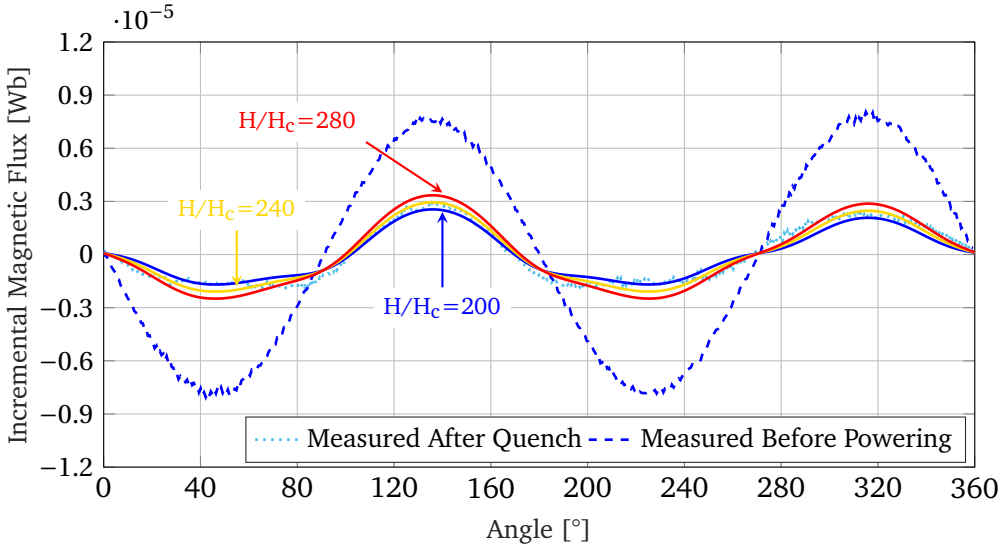

Figure 4.15: *Comparison between simulated flux curves for different values of the coercive magnetic field strength and the measured signal obtained after quench development in the magnet.*

performed a sensitivity analysis of the calculated incremental flux taking the coercive magnetic field strength H_c as a free parameter that has to be different from the one used for the not quenched configuration. In Fig. 4.15 we reported different values of H_c used to evaluate the best configuration of the quenched signal. We can observe that the best H_c value that fits the experimental data is equal to 220 A/m. This value for H_c has to be compared to the value H_c =800 A/m used to reproduce the experimental data measured at zero current before the magnet energization. The amplitude of the simulated signal is in good agreement with the data but remains some differences in the shape of the curve as a function of the rotation angle around the magnet symmetry rotational axis. The different values of the coercive field strength for the residual magnetic field after a quench event and after a slow ramp down to zero current is in agreement with the approximation done in the previous model where we scaled the iron magnetization contribution confirming the anomalous behavior observed by the iron material. An additional sensitivity analysis has been performed to evaluate the combination of three different parameters of the simulations: the value of H_c in the hysteretic curve, the value of the angle of the magnetization vector of the not quenched coil cross-section, and the magnitude of the averaged cross-section studied with different scaling factors. The results of the analysis are reported in the 3D surfaces of Fig. 4.16. The different surfaces have been obtained for different values of the scaling factor of the averaged coil superconductor magnetization. The wider variety of the

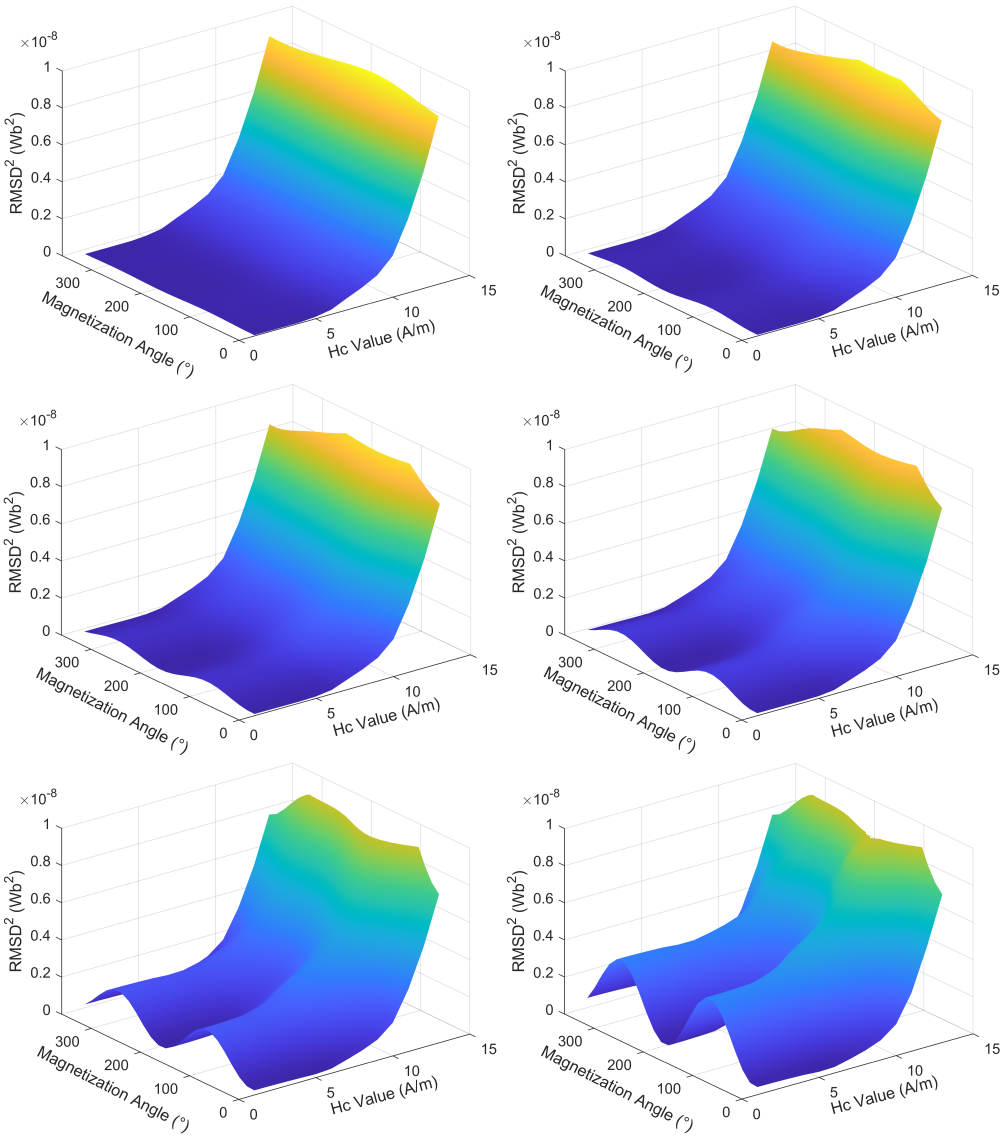

Figure 4.16: *Surfaces of the calculated deviation from the experimental data of the simulation results obtained from the sensitivity analysis. The free parameters used in this analysis are the coercive field of the hysteretic loop curve, the superconducting coil magnetization angle, and the averaged magnetization amplitude.*

simulated residual incremental flux has been obtained changing the value of the magnetization orientation of the not quenched superconducting coil suggesting that the parameters used in the simulation can be tuned to achieve compatibility with the experimental data. The sensitivity to this particular parameter is also a direct consequence of the dipolar approximation of the total averaged magnetization of the whole superconducting coil area which in reality is not uniform. To further improve the accuracy of the simulations, the direction of the equivalent dipoles in the 2D magnet cross-section has been set as a free parameter which however has to be compatible with the main direction of the magnetic field on the coil cross-section area. The simulations have been improved considering a possible asymmetric rotation of the dipoles, whose directions have been previously kept fixed according to the quadrupolar magnetic field induced on the superconductor area and symmetric for all the not quenched coils. The rotation angle α has been always defined from the x-axis of the 2D magnet cross-section to the direction of the equivalent dipolar magnetization of the first not quenched superconducting coil in the reference frame of the magnet. To create an asymmetric configuration of the direction of the magnetization in the different not quenched superconducting coils, we

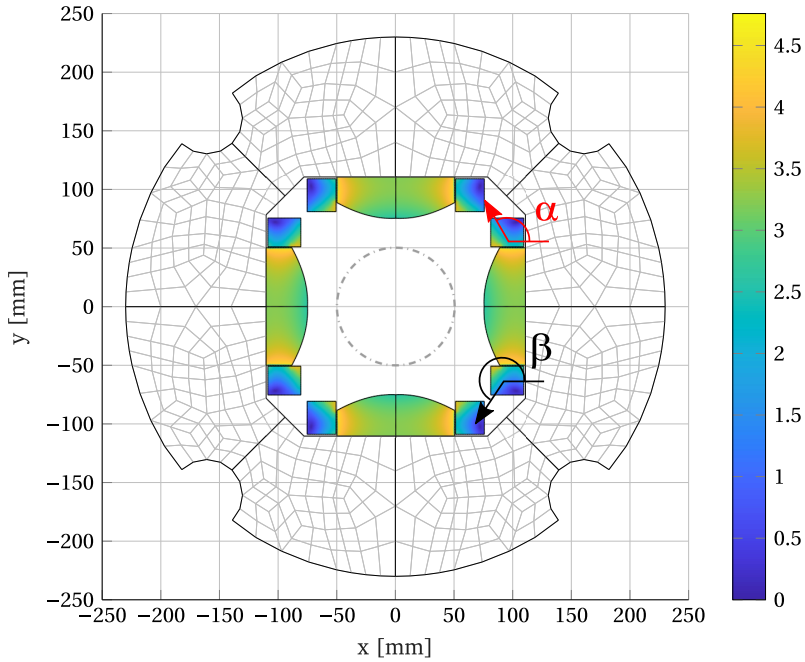

Figure 4.17: *Sketch of the angle between the two different types of averaged magnetization on the cross-section of the superconducting coil on the right and the x-axis of the MQSXFP1b assembly. The colormap used in this picture represents the value of the magnetic field produced by the magnet at the nominal current of 174 A.*

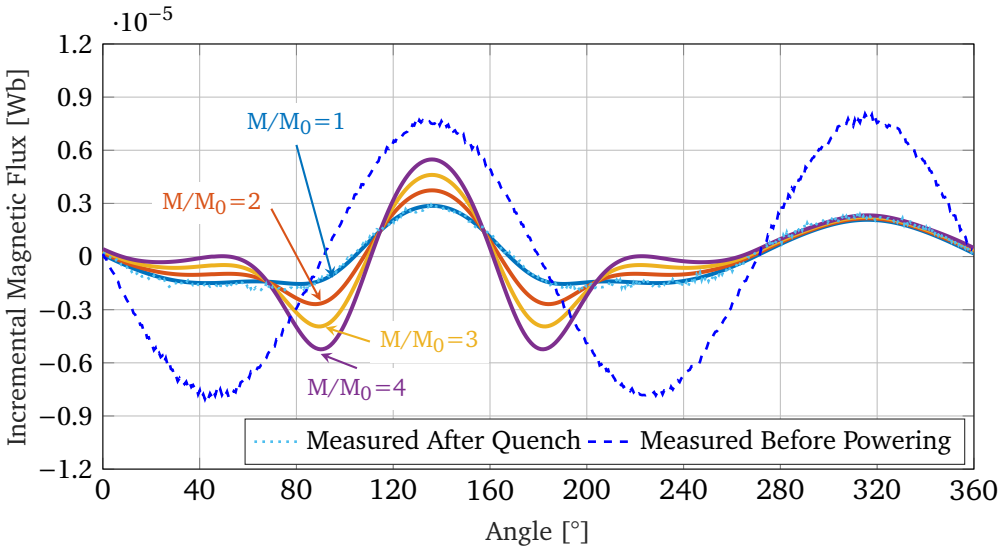

Figure 4.18: *Evaluation of the residual magnetic flux with an asymmetric rotated dipoles configuration. The experimental data have been also compared to simulations with different levels of amplified superconducting magnetization.*

firstly rotated the dipoles nearest to the quenched coil, the one highlighted in Fig. 4.17 and its symmetrical in the x-axis direction, by an α angle, and then rotated the other remaining 4 dipoles by a β angle. The best configuration obtained from the rotation of the dipoles has been reported in Fig. 4.18 and has been obtained with α=120° and β=225°. Considering that in the symmetrical configuration α=115° and β=245°, the upper dipoles in the 2D cross-section have been rotated in the anti-clockwise direction while the lower dipoles in the clockwise direction smoothing the residual magnetic flux signal for high values of the angular position. This variation has been considered realistic to explain the results of measured data because of the mutual interaction between every single magnetization of the not quenched coil which is rearranged in an asymmetric configuration if a quench event happens in the magnet. From the comparison between Fig. 4.15 and Fig. 4.18 we can see that both the amplitude and the shape of the simulated signal are now in agreement with the experimental data only in the asymmetric configuration of the dipole orientation. Here, in Fig. 4.19, we reported the comparison between experimental data and the best configurations obtained from the 2D FEM simulation of the residual magnetic field flux.

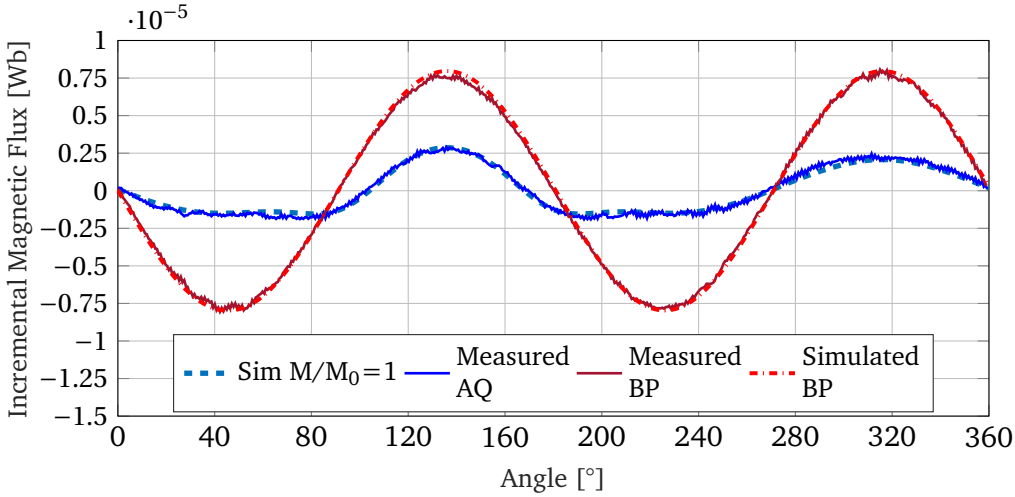

Figure 4.19: *Evaluation of the residual magnetic flux with an asymmetric rotated dipoles configuration and H_c=200 A/m for the reproduction of the experimental quenched one and the symmetric permanent magnet simulation, with H_c=800 A/m for the comparison with the residual flux obtained before magnet powering.*

4.5 Harmonic Model

In the previous section we have shown that, from the comparison of the residual magnetic incremental flux, obtained in the first case after a quench event in the magnet and the second case after a slow ramp down to rest, the localization of the quenched coil in the magnet can be reconstructed using an analytical and a FEM model of the not quenched coil magnetization effect on the shape of the magnetic field produced. However, this method cannot be further adopted for the analysis of quench events in magnets with higher multipole numbers. The number of the coils is directly proportional with the magnet order of rotational symmetry and the different quenched configurations that would have to be analyzed will increase in complexity limiting the accuracy of the study. To extend the model presented previously and understand the variation of the expected results with different magnet orders, we developed a 2D harmonic analysis of the residual incremental field flux produced by a quenched configuration of the coil inside the magnet. Considering a generic 2m-order magnet design we can evaluate the harmonic coefficients of all the not quenched coils of the magnet starting from the magnetic field produced by the single magnetization of a superconducting coil cross-section area located in the complex position **z**. As done in the previous section for the analytical and FEM model of the MQSXFP1b assembly, we can assume that the single-coil magnetization can be approximated by a loop of current with the normal

vector, perpendicular to its surface, oriented in the same direction of the magnetization angle. Considering the cross-section of this loop of "magnetization" current we can describe the complex harmonics generated in the bore area using the multipolar expansion of the magnetic field produced by a single current source, see [47].

$$\mathbf{C}_n = \frac{i\mu_0}{2\pi}\int \frac{J}{z^n} d\sigma \tag{4.13}$$

To simplify the calculations of the harmonics produced by an arbitrarily oriented magnetization dipole we can decompose the single associated loop into its projections on the magnet reference frame and calculate the two contributions separately, see Fig. 4.20. Considering the position in the complex plane of each single loop current cross section and including the polarity of the current we can describe the magnetic field harmonics coefficients as:

$$\mathbf{C}_n = \frac{i\mu_0}{2\pi}\int \left[\frac{J_1}{\left(z-\frac{idy}{2}\right)^n} - \frac{J_1}{\left(z+\frac{idy}{2}\right)^n} + \frac{J_2}{\left(z+\frac{dx}{2}\right)^n} - \frac{J_2}{\left(z-\frac{dx}{2}\right)^n} \right] d\sigma \tag{4.14}$$

The central position of the magnetization dipole can be collected simplifying the fraction in the Eq. 4.14.

$$\mathbf{C}_n = \frac{i\mu_0}{2\pi}\int \left[\frac{J_1}{z^n}\left[\frac{1}{\left(1-\frac{idy}{2z}\right)^n} - \frac{1}{\left(1+\frac{idy}{2z}\right)^n} \right] + \frac{J_2}{z^n}\left[\frac{1}{\left(1+\frac{dx}{2z}\right)^n} - \frac{1}{\left(1-\frac{dx}{2z}\right)^n} \right] \right] d\sigma \tag{4.15}$$

Since the transversal dimensions of the magnetization loop was chosen a priori

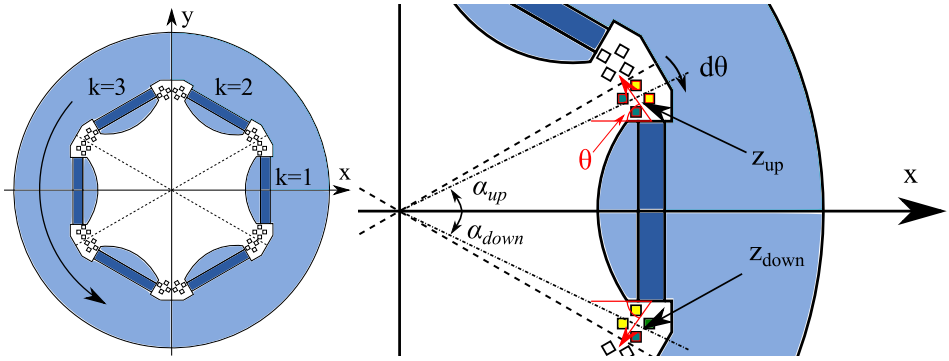

Figure 4.20: *Sketch of the superconducting coil magnetization modeled as an equivalent dipole and used for the calculation of the harmonic components of the residual magnetic field produced by the magnet after a quench.*

and its module is mush smaller of the total distance of the coil cross section from the center of the magnet, we can expand the fraction at the first order of the approximation obtaining the following equation:

$$\mathbf{C}_n = \frac{i\mu_0}{2\pi}\int\left[\frac{J_1}{z^n}\left[1+\frac{indy}{2z}-1+\frac{indy}{2z}\right]+\frac{J_2}{z^n}\left[1-\frac{ndx}{2z}-1-\frac{ndx}{2z}\right]\right]d\sigma \tag{4.16}$$

Simplifying the equation and reconstituting the definition of the magnetic dipole moment m we obtain the expression of the harmonic coefficients generated by half of the not quenched coil in the model.

$$\begin{aligned}\mathbf{C}_n &= \frac{i\mu_0 n}{2\pi}\int\left[\frac{J_1 dyi}{z^{n+1}}-\frac{J_2 dx}{z^{n+1}}\right]d\sigma \\ &= \frac{i\mu_0 n}{2\pi L_z}\left[\frac{m_x i - m_y}{z^{n+1}}\right] = -\frac{\mu_0 n}{2\pi L_z}\left[\frac{m_x + i m_y}{z^{n+1}}\right]\end{aligned} \tag{4.17}$$

where the m_x and m_y components of the magnetic dipole moment are calculated as projection on the magnet reference system frame and the L_z parameter defines the equivalent length of the coil in the rotational axis direction. To evaluate the contribution of the whole not quenched coil we can calculate the harmonic coefficients for the upper and the lower cross section changing the corresponding position $\mathbf{z}_{UP/DOWN}$ and taking note of the different angle of each magnetization angle. In this case we considered that, for a single coil, the two cross section in the 2D plane have a symmetrical magnetization distribution respect the coil axis eve if a small asymmetry can be expected as consequence of the single quenched coil in the magnet layout, see Fig. 4.20.

$$\mathbf{C}_{n-UP} = -\frac{\mu_0 n}{2\pi L_z}\left[\frac{m_x + i m_y}{z_{UP}^{n+1}}\right] \qquad \mathbf{C}_{n-DOWN} = -\frac{\mu_0 n}{2\pi L_z}\left[\frac{m_x - i m_y}{z_{DOWN}^{n+1}}\right] \tag{4.18}$$

The position of each coil cross section is defined by the distance from the magnet center ρ and the phase angle in the complex plane. We can therefore modify the previous equation of the two separate contributions obtaining the following set of equations:

$$\mathbf{C}_{n-UP} = -\frac{\mu_0 n}{2\pi L_z}\left[\frac{m_x + i m_y}{\rho^{n+1}}\right] e^{-i(n+1)\alpha_{up}} \tag{4.19}$$

$$\mathbf{C}_{n-DOWN} = -\frac{\mu_0 n}{2\pi L_z}\left[\frac{m_x - i m_y}{\rho^{n+1}}\right] e^{-i(n+1)\alpha_{down}} \tag{4.20}$$

where $\alpha_{up} = +\alpha$, $\alpha_{down} = -\alpha$ and $\alpha = \frac{\pi}{2m} - d\theta$. The parameter α represents the angular distance of the coil cross-section in the 2D plane from the pole axis of symmetry while the parameter $d\theta$ represents the distance from the

axis of symmetry between two consecutive iron poles in the magnet of order m. The two magnetic dipole moments can be rewritten in the complex form as $\mathbf{m}_{up} = m_x + i m_y$ and $\mathbf{m}_{down} = m_x - i m_y$. By adding the two contributions of Eq. 4.19 and Eq. 4.20 we obtain the magnetic field harmonic coefficients produced by the single coil on the middle plane for any order of the magnet.

$$\mathbf{C}_n^1 = -\frac{\mu_0 n}{2\pi L_z \rho^{n+1}} \left[\mathbf{m}_{up}\ e^{-i(n+1)\alpha_{up}} + \mathbf{m}_{down}\ e^{-i(n+1)\alpha_{down}} \right] \tag{4.21}$$

To describe the contribution to the harmonic coefficients of all the k_{th} superconducting coil magnetization in the magnet, we could generalize the Eq. 4.21 rotating the two magnetization dipole moments $\mathbf{m}_{up}$ and $\mathbf{m}_{down}$ by an angle $(k-1)\pi/m$ and transforming the two $\alpha_{up/down}$ angles with the following equations:

$$\begin{aligned} \mathbf{m}_{up} &\rightarrow \mathbf{m}'_{up} &&= (-1)^{k-1} \mathbf{m}_{up}\ e^{i(k-1)\frac{\pi}{m}} \\ \mathbf{m}_{down} &\rightarrow \mathbf{m}'_{down} &&= (-1)^{k-1} \mathbf{m}_{down}\ e^{i(k-1)\frac{\pi}{m}} \\ \alpha_{up} &\rightarrow \alpha'_{up} &&= (k-1)(\pi/m) + \alpha \\ \alpha_{down} &\rightarrow \alpha'_{down} &&= (k-1)(\pi/m) - \alpha \end{aligned} \tag{4.22}$$

with k spanning in the range between 1 and 2m. To account the polarity of each single coil, the magnetic dipoles are multiplied by the factor $(-1)^{k-1}$. Using the new expressions of Eq. 4.22 we can describe the harmonic coefficients produced by the k^{th} coil with the following equation:

$$\mathbf{C}_n(k) = -\frac{\mu_0 n (-1)^{k-1}}{2\pi L_z \rho^{n+1}} \left[\mathbf{m}_{up}\ e^{i(k-1)\frac{\pi}{m}} e^{-i(n+1)\alpha'_{up}} + \mathbf{m}_{down}\ e^{i(k-1)\frac{\pi}{m}} e^{-i(n+1)\alpha'_{down}} \right]$$

By simplifying the terms of the equation and substituting the definition of the two angles α'_{up} and α'_{down}, we obtain:

$$\mathbf{C}_n(k) = -\frac{\mu_0 n (-1)^{k-1}}{2\pi L_z \rho^{n+1}} \left[\mathbf{m}_{up}\ e^{-i(n+1)\alpha} e^{-in(k-1)\frac{\pi}{m}} + \mathbf{m}_{down}\ e^{i(n+1)\alpha} e^{-in(k-1)\frac{\pi}{m}} \right]$$

The scaling factor $(-1)^{k-1}$ could also be converted to the exponential form and grouped with the phase of the two added terms in the equation.

$$\mathbf{C}_n(k) = -\frac{\mu_0 n}{2\pi L_z \rho^{n+1}} \left[\mathbf{m}_{up}\ e^{-i(n+1)\alpha} + \mathbf{m}_{down}\ e^{i(n+1)\alpha} \right] e^{i\pi(k-1) - in(k-1)\frac{\pi}{m}}$$

By recalling the definitions of the two magnetic dipole moments, we can observe that $\mathbf{m}_{down}$ is the complex conjugate of $\mathbf{m}_{up}$. The two added contributions can be therefore rewritten as the real part of the first magnetic dipole

moment multiplied by the phase described by the α angle.

$$\mathbf{C}_n(k) = -\frac{\mu_0 n}{2\pi L_z \rho^{n+1}} Re\left[\mathbf{m}_{up}\ e^{-i(n+1)\alpha}\right] e^{-i\frac{n-m}{m}(k-1)\pi}$$

$$\mathbf{C}_n(k) = -\frac{\mu_0 n}{2\pi L_z \rho^{n+1}} \left[m_x\ \cos\left[(n+1)\alpha\right] + m_y\ \sin\left[(n+1)\alpha\right]\right] e^{-i\frac{n-m}{m}(k-1)\pi}$$

The expression of the m_x and m_y components of the magnetization dipole moment could also be written as function of the dipole moment magnitude and the angle θ between the magnetic dipole moment direction and the x-axis of the magnet reference frame. Using the relations $m_x = m\cos(\theta)$ and $m_y = m\sin(\theta)$ we obtain the expression:

$$\mathbf{C}_n(k) = -\frac{\mu_0\ n}{2\pi L_z \rho^{n+1}} m\left[\cos(\theta)\ \cos\left[(n+1)\alpha\right] + \sin(\theta)\ \sin\left[(n+1)\alpha\right]\right] e^{-i\frac{n-m}{m}(k-1)\pi}$$

The trigonometric piece expression can be simplified to obtain the final equation for the harmonic coefficients produced by the k^{th} coil in the superconducting magnet, reported in Eq. 4.23.

$$\mathbf{C}_n(k) = -\frac{\mu_0\ n}{2\pi L_z \rho^{n+1}} m\left[\cos(\theta - (n+1)\alpha)\right] e^{-i\frac{n-m}{m}(k-1)\pi} \tag{4.23}$$

We can observe that the amplitude of each magnetic field harmonic is proportional to the magnetization level of the superconducting coil cross-section and depends also on the magnetization orientation in the xy plane and the width of each superconducting coil, see parameters θ and α. To obtain the real magnetic field quality of the quenched magnet configuration, considering only one single quenched coil, we have to sum up over the k parameter all the $\mathbf{C}_n(k)$ and then subtract the quenched coil contribution, identified with the j parameter:

$$\mathbf{C}_n^j = \sum_{k=1}^{2m} \mathbf{C}_n(k) - \mathbf{C}_n(j) \tag{4.24}$$

By plotting each harmonic for a fixed 2m-poles magnet, we can observe that the initial phase of the n-order harmonic is dependent on the number of the k^{th} quenched coil. The first term of Eq. 4.24 has the same rotational symmetry of the 2m-poles magnet and does not produce non-allowed harmonics in the residual magnetic field. The not allowed harmonics are only created by the second contribution $\mathbf{C}_n(j)$ which takes into account only the quenched coil in the magnet and depends on its position in the magnet reference frame. The phase of the non-allowed harmonics is ruled by the fraction $((n-m)/m)(k-1)$ where the n parameter identifies the order of the considered harmonic, m is

the magnet order and k is the quenched coil number. If we consider the main harmonic of the magnet, setting n=m, for each k quenched coil we have the same initial phase and the position of the quenched coil could not be identified. If we set n=m±1, the different initial phases go from 0 to 2π without any repetitions allowing us to identify without any doubt which coil has quenched in the magnet. Also, if we consider n=m±2 or any other harmonic close to the magnet order, the different initial phase will span from 0 to a multiple of 2π with repetitions for the different quenched coils in separate positions. Therefore, from the analysis of the not allowed magnetic field harmonic coefficient initial phases, and in particular the harmonics with order closest to the magnet order, n=m±1, we can reconstruct exactly the position of the quenched coil of a magnet with any order.

4.6 FEM Model and Comparison with real quench events

4.6.1 Simulations

To verify the influence of the iron configuration and magnetic properties on the field harmonic coefficients after a quench event, we reused the same FEM model developed for the reconstruction of the MQSXFP1b residual magnetic field at zero current. The skew quadrupole model has been upgraded for the simulation of both normal and skew configurations of all the orders of the HL-LHC HO corrector magnets. In the model, for a 2m-poles magnet, all signals generated by the k^{th} quenched coil configuration have been analyzed and the corresponding harmonic coefficients have been retrieved calculating the parameters m and θ of the analytical model described in Eq. 4.23. These two parameters directly affect the value of the real and imaginary part of the harmonic coefficients fixing the initial phase value for any single coil quenched configuration. From the comparison between the analytical model and the FEM one, we observed that all the magnetic field harmonics initial phase are predicted in the same way suggesting that the iron configuration and shape do not affect the phase of every single harmonic coefficient but only the amplitude of the allowed harmonics of the magnet. Indeed, the FEM simulated amplitude of the harmonic coefficients is a function of the strength of the permanent magnet used to simulated the iron contribution to the residual magnetic field incremental flux. Here we report, in Fig. 4.21 and Fig. 4.22, the first simulated not allowed harmonics of a skew quadrupole and a normal sextupole as a function of the quenched coil inside the magnet together with the main component of the residual magnetic field produced. The amplitude of the simulated signals is only a function of the iron hysteresis loop used in the FEM model, the amplitude of the superconductor magnetization and the angle θ between the equivalent magnetic dipole moment and the magnet x-axis.

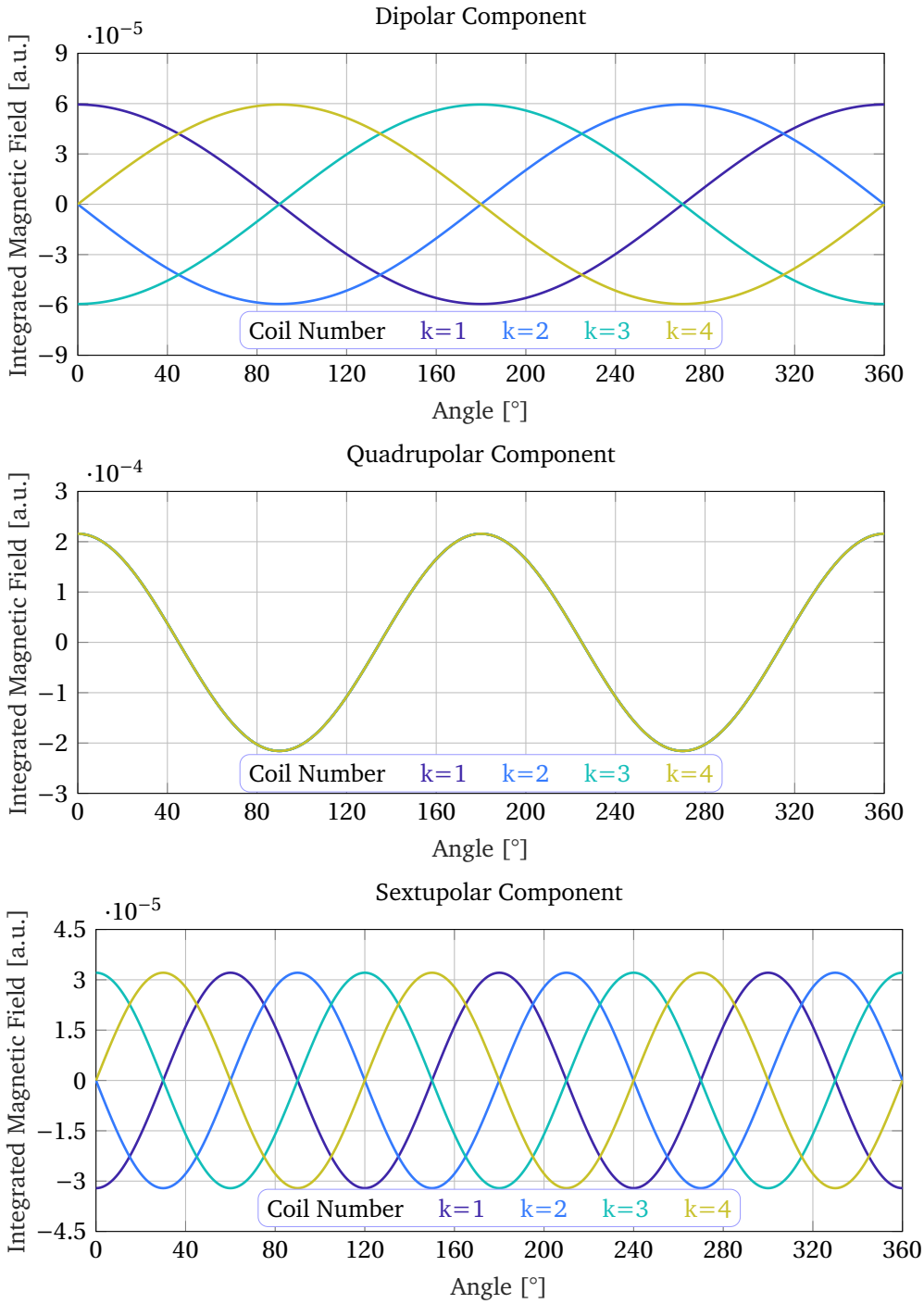

Figure 4.21: *First harmonics of the residual magnetic field simulated in the High Order Quadrupolar magnet design with different quenched coil configuration. The parameter reported in the legend corresponds to the configuration where only the k^{th} coil is quenched and therefore identifies its position in the magnet.*

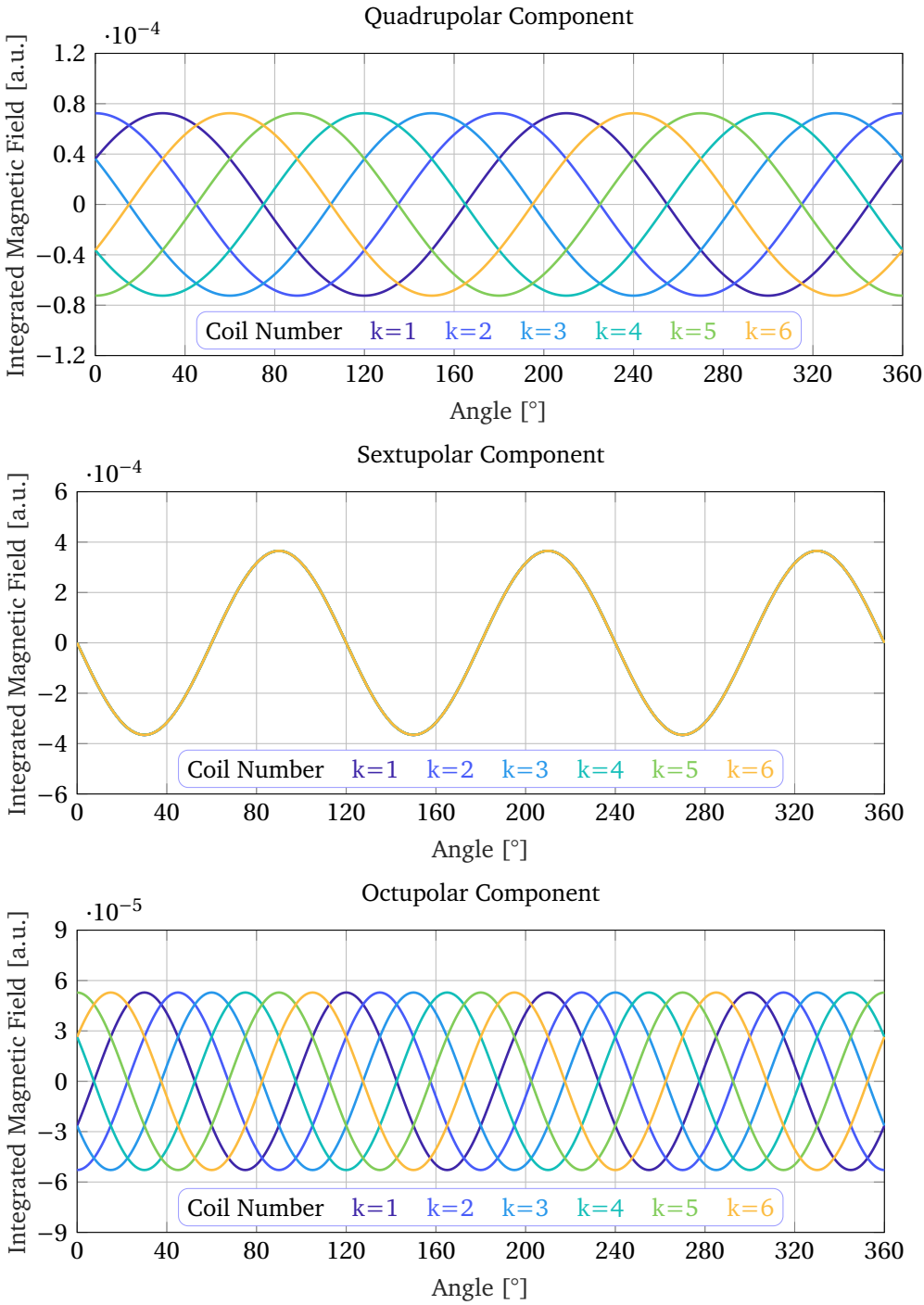

Figure 4.22: *Harmonics of the residual magnetic field simulated in the High Order Sextupole magnet design with different quenched coil configuration. The same k parameter of Fig. 4.21 is used here to point to the only k^{th} coil which has quenched in the magnet*

Instead, the single phase of the k^{th} quenched coil configuration is specifically dependent on the position of the coil and has the same periodicity of the magnet. From the FEM simulation of the harmonic coefficients, as we predicted in the analytical calculation of their values, we can observe that the m-1 and the m+1 harmonic coefficients of an m-order magnet present the bigger phase shift without repetitions between the different signals of the quenched coil configurations inside the magnet and therefore allow an easier localization of the quenched event. The reported simulations have been obtained for a quench from a positive energizing current in the magnet but the same behavior can be obtained for a quench at negative energizing current by changing only a global phase to all the calculated harmonics. To verify the accuracy of the proposed harmonic model and detect the location of the quenched coil inside the HO corrector magnets we analyzed the residual magnetic field produced after quench events of three magnets tested and characterized at LASA.

4.6.2 Skew Quadrupole MQSXFP1c Quench Localization

The first magnet analyzed is the MQSXFP1c assembly tested in October 2020 at LASA together with the MCDXF01 magnet. The MCDXF01 did not show any training so no results are shown for this magnet. During the training phase, the MQSXFP1c magnet had 7 different quenches before reaching the ultimate current. All the quench events have been analyzed studying the voltages of the two halves (A or B) of the magnet to determine where the quench occurred. Only the 4^{th} quench event, developed at I= 115 A, has been recorded as developed in the B side of the magnet while all the other quench have been recorded in the A-side. The residual magnetic field produced after each single quench event has been reported in Fig. 4.23. Analyzing the raw signal obtained from the incremental field flux, a similar shape of the curves with the already analyzed quench event of MQSXFP1b has been observed. All the signals have been filtered subtracting the residual magnetic field incremental flux produced before the first energization of the magnet. The filtered signals have been reported in Fig. 4.24 but the localization of the quenched coil for every single event has not been possible. Calculating the Fourier transform of the magnetic field total flux from every single curve, the single harmonic coefficients have been finally obtained. In the following figures, we reported the dipolar, quadrupolar, and sextupole harmonics of the analyzed magnetic field flux of the MQSXFP1c quench events comparing also the harmonics retrieved by the MQSXFP1b assembly quench event. As we expected, the quadrupolar harmonic, Fig. 4.26, of all the quench event residual flux have the same initial phase. The amplitude of the different signals decreases with higher values of the current at which the quench occurred confirming the same behavior we observed in the amplitude of the quench event of MQSXFP1b where the iron

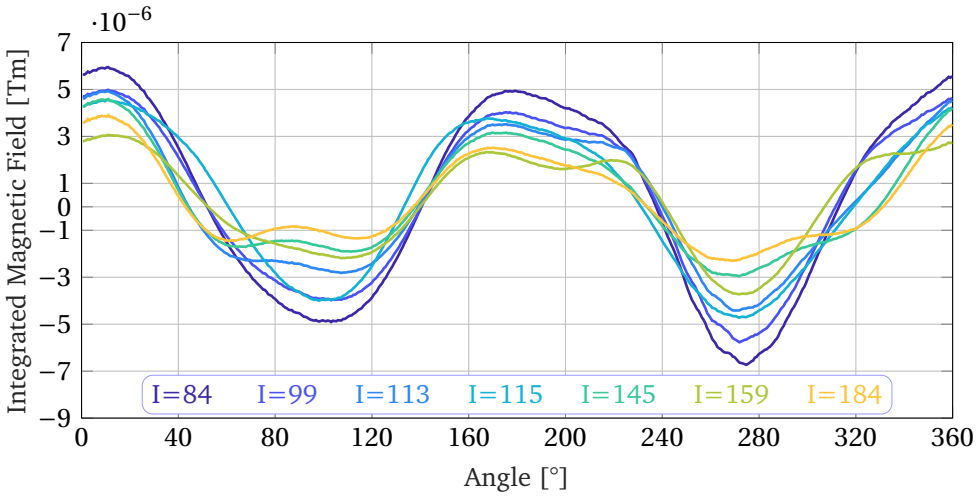

Figure 4.23: *Raw incremental flux measured after each single quench event of the MQSXFP1c assembly as function of the angular position of the encoder.*

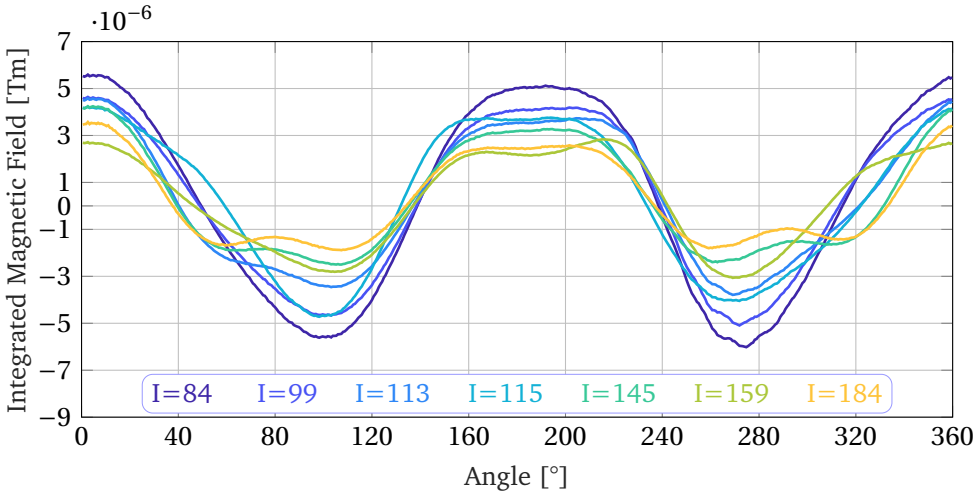

Figure 4.24: *Filtered incremental flux measured after each single quench event of the MQSXFP1c assembly. The filtered signals are more symmetric than the raw one but still have some additional oscillation.*

contribution to the field harmonic decreases with a faster decay rate of the current. From the analysis of both the dipole, Fig. 4.25, and sextupole, Fig. 4.27, components of the measured magnetic flux, we can identify four main groups in which divide the different events. In the first group, the quench events that happened at operating current I= 84 A, 99 A, and 159 A have the same initial

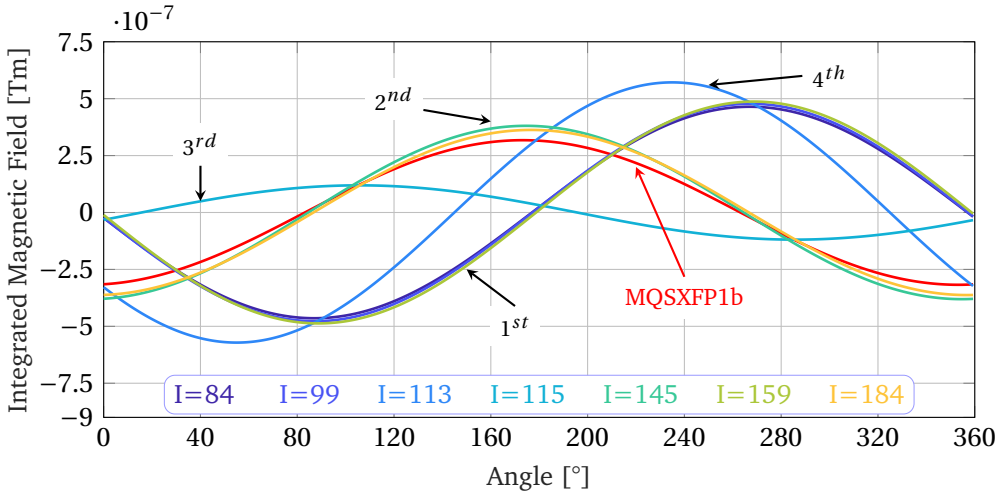

Figure 4.25: *Dipolar component of the magnetic field harmonics produced by the residual magnetic flux after the quench events of MQSXFP1c. The three defined groups with a compatible phase shift have a lower amplitude compared to the quench event at 113 A. The dipolar integrated magnetic field measured is one order of magnitude lower than the principal quadrupolar component of the measured flux*

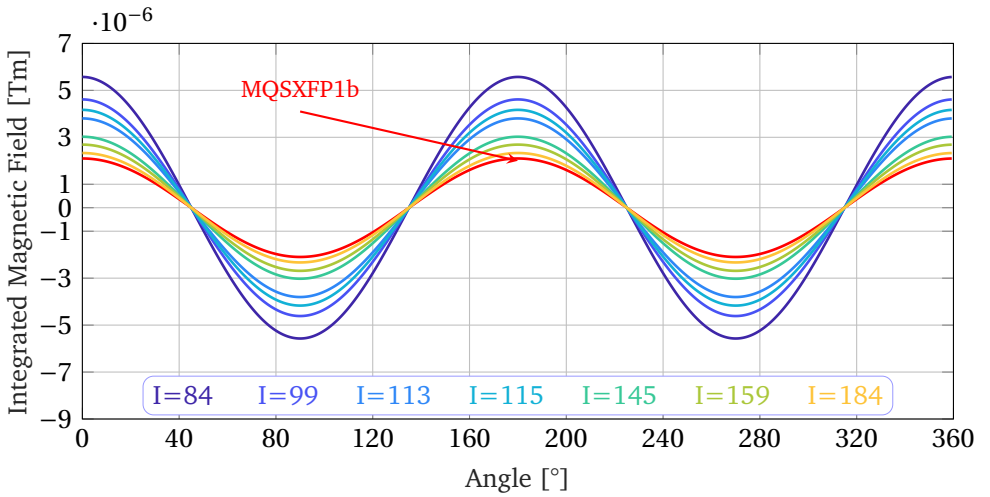

Figure 4.26: *Quadrupolar component of the magnetic field harmonics produced by the residual magnetic flux after the quench events of MQSXFP1c. All the signals have the same initial phase. From the signal, a small rotation of the quadrupolar field can be observed probably due to the accuracy of the alignment between the magnetic measurement system and the reference frame of the magnet.*

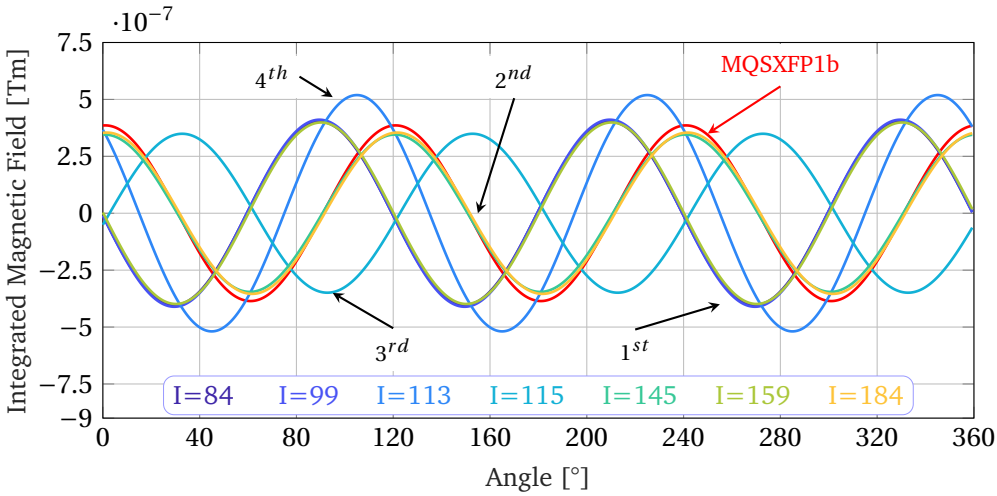

Figure 4.27: *Sextupolar component of the magnetic field harmonics produced by the residual magnetic flux after the quench events of MQSXFP1c. As observed for the dipolar component of the signal, the three defined groups have a lower amplitude compared to the quench event at 113 A. As for the dipole content, also the sextupolar measured integrated magnetic field is one order of magnitude lower than the quadrupolar main component.*

phase and amplitude. The second group contains the quench events that happened at I= 145 A and 184 A which is also compatible with the quench event that occurred in the MQSXFP1b assembly test. the third group contains only the quench event that happened at I=115 A. These three main groups have a corresponding phase equal to the one predicted by the simulations. In particular, the harmonic content of the first group has been calculated, from the harmonic model, as a consequence of the quench developed in the 2^{nd} coil of the assembly while the second group corresponds to the quench event in the 3^{rd} coil which both belongs to the A half of the magnet as correctly registered by the fast acquisition of the QDS. The third group, instead, is correctly registered from this harmonic model due to a quench event that happened in the fourth coil of the assembly which belongs to the B side of the magnet. The fourth group contains only the quench that occured at I=113 A. The harmonics of the residual flux, produced by this quench, have not a defined phase as predicted by the harmonic model both in the dipole and sextupole harmonic analysis. This quench event signal has an intermediate phase value between the one corresponding to the 2^{nd} and 3^{th} coil. Since both these coils belong to the half part of the magnet where the quench has been detected by the QDS system, the intermediate value of the phase suggests that also this quench event happened on the same A-side of the magnet. A possible hypothesis to explain this not predicted harmonic content is an asymmetry of the quench

propagation inside the superconducting coil, not considered in the analytical and FEM model, which would have caused an asymmetric distribution of the residual superconductor magnetization and therefore an intermediate value of the predicted phase.

4.6.3 Sextupole MCSXF01 Quench Localization

The second magnet which has been characterized with the magnetic measurement system is the first sextupole produced for the HO corrector series. The MCSXF01 magnet has been tested in the same vertical stack as the MCDXF02 magnet, the MCOXF01, and the MCTXF01 magnet. The rotating shaft used for this test is the temporary 1.5 m long carbon fiber rotating shaft which has measured the MQSXFP1c and MCDXF01 magnetic field quality in the previous test at LASA. The first sextupole of the production series shows only 5 quenches before reaching the ultimate current and satisfies the CERN requirements for the magnet performances. All the quench events happened during the energization phase while the last quench, recorded to develop at the current of 112 A, happened during the one-hour stability test where no quench are expected to develop unless intrinsic instabilities of the connections of the magnet or other external disturbance start the transition of the superconductive material. The same analysis previously described for MQSXFP1c has been performed also on the residual magnetic field incremental flux of the measured signals after the quench events. For the analysis of this magnet, the quadrupolar, sextupolar, and octupolar components of the magnetic field have been retrieved. The analysis of the main sextupolar harmonic, reported in Fig. 4.28 shows that all the signals have roughly the same amplitude and initial phase while the only curve which differs from the others is the one obtained for the quench event that happened at I=112 A during the one-hour stability test. By considering the value of the initial phase, the analysis of the main harmonic can be also used to cross-check the polarity of the magnet during the energization test. Indeed all the quench events happened during the positive energizing of the magnet while the one-hour stability test has been performed at -I_{ult} giving, therefore, an opposed initial phase in the main harmonic generated after the last quench of the magnet. The quadrupolar harmonic of the residual magnetic field produced after the quench events are reported in Fig. 4.29. From the observation of the different curves, we can point out that the signals obtained from quench happened at I=112 A and 98 A have the same phase while the quenched at I=66 A has the opposite initial phase. These two different initial phases are predicted by the analytical and FEM model of the magnet, see Fig. 4.22, and are associated to a quenched coil at ±90° from the zero of the measurement (2^{nd} and 5^{th} coil) if the magnet is in the normal configuration. Combining this information with the corresponding main harmonic component previously

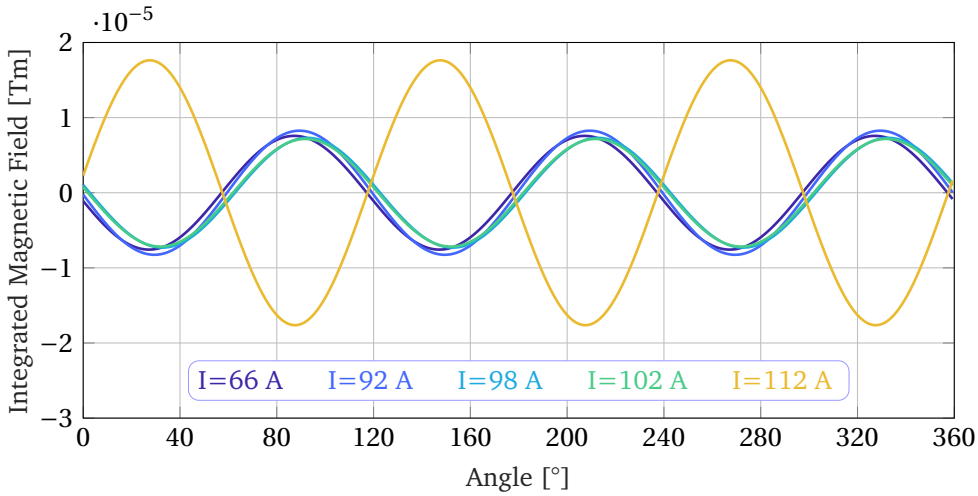

Figure 4.28: *Main harmonic produced in the signal of MCSXF01 after quench events at zero current. The initial phase of all the measured signals is compatible with the null value (or with half rotation for the I=112 A signal) within the error bar of the measurement.*

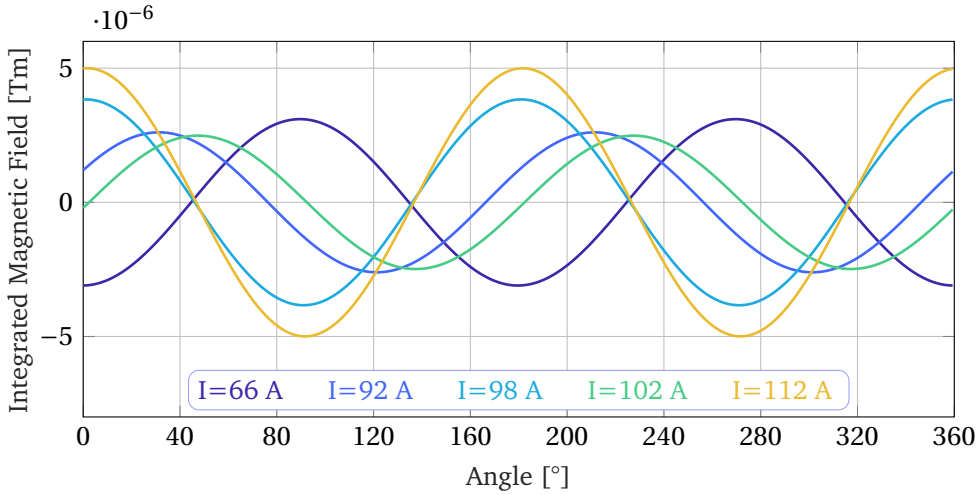

Figure 4.29: *Representation of the reconstructed quadrupolar component of the magnetic field harmonic measured in the residual signal of MCSXF01 after quench events. The maximum amplitude of the signal is lower than the main sextupolar harmonic generated by the magnet.*

described, we reconstructed that the quenched happened at I=66 A and 112 A are localized in the B side of the magnet and more precisely are due to the same superconducting coil in the middle of the B side, see Fig. 4.31, while the quench at I=98 A is localized in the A-side and is due to the superconducting

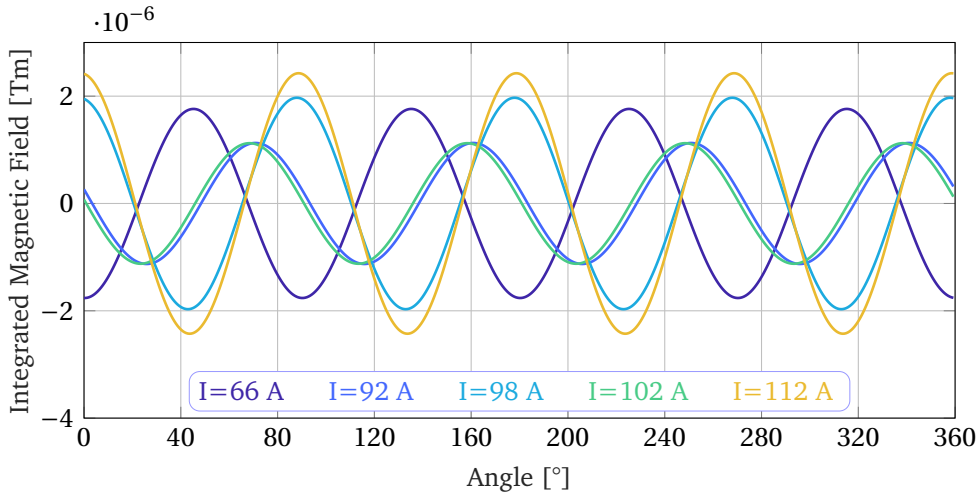

Figure 4.30: *Octupolar component of the harmonics produced by MCSXF01 after each quench event. The same grouping of signals as for the quadrupolar component of the harmonics is observed. The only exception is the quench at I=102 A which now can be grouped with the quench at I=92 A.*

coil in the middle. The quench event occurred at I=92 A has instead an initial phase corresponding to the first coil which is reconstructed by the model in the A-side of the magnet. The same reconstruction for all the quench events presented until now could also be performed observing the octupolar harmonic reported in Fig. 4.30. All the reconstructions of the quenched coil position are perfectly matched from the QDS system which, however, is able only to localize the quench in the A or B side of the magnet. The only quench event, which generated a quadrupolar harmonic not predicted by the model is the one that happened at I=102 A. From the analysis of the initial phase of this harmonic and the comparison between the harmonic model, the closest match for this event are the signals corresponding to the two consecutive superconducting coils immediately before and after the zero of the reference system (1^{st} and 6^{th} coils in Fig. 4.22 which are also corresponding to the position of the external connection of the magnet). To evaluate which one of the superconducting coil has quenched in the magnet we can observe the other calculated harmonic like for example the octupolar component of the magnetic field, reported in Fig. 4.30. The quenched occurred at I=102 A has produced an octupolar magnetic field harmonic predicted by the model which is also produced for the quench at I=92 A. From the observation of the harmonic model prediction, the quench position for these two events has been calculated to be in the first coil of the A-side of the magnet in perfect agreement with the QDS system.

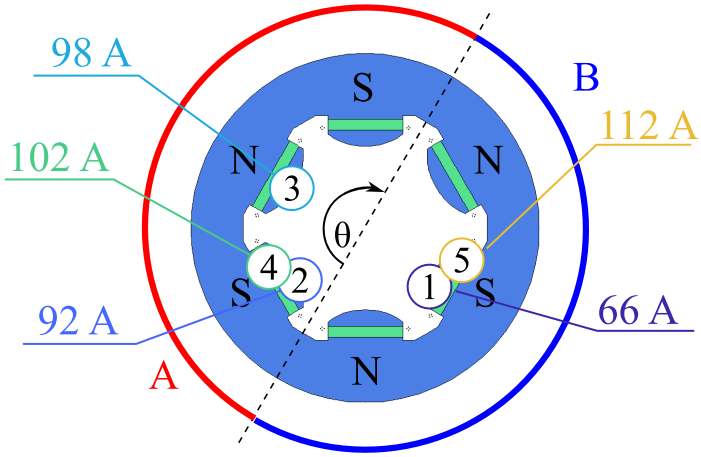

Figure 4.31: *Physical representation of the distribution of the quenched coil inside MCSXF01. The separation between the A and B sides of the magnet is represented and also the number of the quench event is also associated with the reconstructed quenched coil of the magnet.*

4.7 Conclusion

In this last chapter, the main innovative aspect of the thesis has been reported and discussed. The voltage taps, which are the most common method to localize the quench in a superconducting magnet, are suitable for the R&D phase of a magnet production process but cannot be further implemented in the series production phase. To restore the possibility to localize the quench in the superconducting coils, external devices like quench antenna are commonly used. The pick-up coils of the antenna detect the redistribution of the current inside the superconductor during the quench development and precisely localize the region of the superconducting coil which started the transition to the normal conducting state. However, quench antennae are suitable for superconducting magnets with low multipole numbers like dipoles and quadrupoles due to the complexity of the pick-up coils which have to be sensitive to all the different regions of the superconducting coils. With high values of the multipole number of the magnet, the number of the coils used increases proportionally and the complexity of the quench antenna design is not more feasible for the construction of real devices. With the here proposed method, using only a single rotating coil shaft and measuring the residual magnetic field produced by the magnet after a quench event, we can identify which of the superconducting coils started the transition. In particular, the quenched coil, which has no magnetization due to the transition, creates an asymmetry of the shape of the residual magnetic field flux in the magnet bore, sampled by the rotating coil, which can be isolated performing a harmonic analysis reconstructing

the position of the quenched coil in the magnet. The complexity of the rotating coil is not linked to the number of the superconducting coils in the magnet, like the quench antenna, and therefore this method can be used to monitor any magnet order with the same identical measuring device. The first hint for the possibility to localize the quenched coil in the HO corrector magnets using the same magnetic measurement system installed at LASA has been observed in the residual magnetic field incremental flux produced by the quadrupole MQSXFP1c assembly. In particular, the signal produced after a quench event and the one after a slow ramp down of current have completely different shapes and amplitudes. To verify that the cause of this difference can be assigned to the asymmetry of the residual superconductor magnetization due to a single quenched coil has been evaluated with two main methods. At first, an analytical model of the superconductor magnetization has been developed and tested trying to reproduce the experimental data. The analytical model can describe an asymmetric distribution of the residual incremental flux but the amplitude of the flux variation as a function of the angle does not match the experimental curve. To match the measured data amplitude, the only found solution is to scale the iron residual magnetization added to the superconductor contribution to obtain the total incremental field flux. To verify the obtained results with the analytical model a FEM simulation model has been developed in OPERA 2D. Thanks to the observation that the BH curve of the iron at low magnetic field strength presents a low value of permeability we understood that the difference in the amplitude of the signal obtained after the quench or after the slow ramp-down is mainly due to the iron contribution. To exactly reproduce this part of the incremental flux we upgraded the 2D model using permanent magnets to exactly model the influence of the iron on the superconducting magnetization distribution. Also, in this case, the only way to reach the same amplitude of the signal after a quench event has been to reduce the strength of the permanent magnet changing the hysteretic loop curve of the iron. To fine-tuning the model to the measured data, complete asymmetric distribution of the superconductor magnetization has been used finding a very good agreement with the experimental data and showing that the position of the quenched coil in the magnet can be reproduced with the simulations. To generalize the model to analyze the residual flux of a generic m-order magnet, where one of the 2m coils has quenched, we analyzed the harmonic coefficients produced by the superconducting magnetization distribution of the not quenched coil. The expected harmonic coefficients have been evaluated both with an analytical model here described and FEM simulations finding very good agreement of the predicted initial phase dependence from the position of the quenched coil in the magnet. Finally, to verify the accuracy of the model the quench event of the skew quadrupole MQSXFP1c and the sextupole MCSXF01 magnets have been analyzed and reconstructed finding

perfect agreement with the QDS signals. This method has then proved that the exact quenched coil position inside a generic m-order magnet can be easily reconstructed with the analysis of the superconducting magnetization distribution effect on the residual magnetic field produced at zero current after the quench event.

Chapter 5
General Conclusions and Perspectives

The Ph.D. thesis work, presented in these chapters, is only one of the many contributions to the development of the next phase of the most powerful particle accelerator ever built: HL-LHC. The constant need for more particle interactions to evaluate the future of the discoveries in the modern particle research field has required the development of a new configuration of the particle accelerator collider which will be able to provide more than ten times the number of collisions produced per second today. Different technological improvements will be the basis for the realization of such an ambitious upgrade project. In particular, many different upgrades will be required for the new superconducting magnet region beside the main Interaction Regions of the CMS and ATLAS experiments to provide more focus on the particle at the collision point. The presented work is inserted in this scenario and has focused on the new type of High Order superferric corrector magnets that will be built by INFN Milano LASA within the collaboration framework with CERN. In particular, within the development program of the HO corrector magnets, the need for a new magnetic field measurement system, optimized exactly for the particular design of this type of superconductor magnets, has brought to the study of the possible interactions between the different magnets both in the LASA vertical cryostat test station and in the LHC corrector package cryostat near the Interaction Region of the particle accelerator. Even if a first analysis of the possible interaction between the different HO corrector magnets was already done for the first design of the magnets, an improved analysis has been necessary to precise evaluate the possible effect on the upgraded magnet design performances. This particular study, however, has also been extended to evaluate all the possible sources of errors in the magnetic field produced by the HO correctors showing that the particular design of the superconductor magnets has very stable performances and high reliability of the produced magnetic field quality.

Thanks to the collaboration with CERN, a new magnetic field measurement system has been developed and installed at LASA to evaluate the performances of all the 54 magnets that INFN has been in charged to test and characterize before the installation in the LHC machine lattice. To calibrate and integrate the magnetic measurement system with the vertical cryostat test station at

LASA a temporary 1.3 m long PCB rotating coil shaft made with a carbon fiber shell has been used for the characterization of the last HO corrector prototypes and the first magnet of the series production. The different order of the HO corrector magnets represents a difficult challenge for the magnetic field measurement system both for the noise during the measurements produced by the residual field of the neighbor magnets inside the PCB coil and the accuracy of the measured data to calculate magnetic field harmonics up to the 18 order. The magnetic field characterizations of the tested magnet using the temporary shaft have been compared with 3D simulations made with OPERA providing also feedback on the magnetic properties of the material used in the simulations. All the built and tested magnets have satisfied the requirements, requested by CERN, for the energization test performance and the magnetic field quality produced.

Despite the compact dimensions of the HO corrector magnet and the relatively small values of current used for their energization, if compared to main superconducting dipoles and quadrupoles produced for modern particle accelerators like LHC, the quench protection study of these magnets is a very challenging aspect of their development. Starting from the unconventional quench protection system that will be adopted at LHC during magnet operation, the requirements for the protection of these magnets have pushed the optimization of the HO corrector design to its limit. To evaluate the performances of this type of magnet and their quench protection, a detailed study has been firstly produced on the prototype design of the magnet focusing on the maximum hot spot temperature and voltage to ground reachable without any damage or degradation of the superconductor material. Thanks to this preliminary study, the protection system of the HO corrector magnets in LHC has been optimized to cope with the high energy density stored by the skew quadrupole. Also, this study has shown that all the chosen designs of the other magnet types can be protected during the operation at LHC without any of the conventional quench protection systems and relying only on their ability to absorb their stored electromagnetic energy without overtaking the safe margin for their protection. The accuracy of the presented simulation model, used to perform the quench protection study of the magnet prototype, has been tested with several experimental data taken from the already built first version of the magnet prototype and tested at the LASA laboratory. The results of the comparison of the model with the experimental data have shown the necessity to increase the accuracy of the used models.

An improved simulation model, based on the co-simulations between the program QLASA, used for the thermal analysis studies, and the program LTSpice, used to solve the magnet circuit equation, has been optimized to simulate the

performances of the final design of the HO corrector magnet in case of quench events. The main improvements of this new model are the novel description of the differential inductance of the magnet which represents a very difficult aspect of the simulations. Thanks to the details of the magnetostatic performances of the HO corrector magnets on all range of possible energizing currents, obtained with 3D OPERA simulations, the improved model of the differential inductance can be easily obtained and used as a new input parameter of the co-simulations of the magnet. The results of a new upgraded quench protection study, performed on the final design of the HO corrector magnet, show that all the magnet can be protected by the developed corresponding quench protection system. The newly developed model accuracy has been also tested with experimental quench events of the magnet prototype design showing a very high accuracy of the results and very good compatibility with real measured data. Thanks to the presented model, the performance of every single different type of the HO corrector magnets can be predicted and compared with the experimental behavior of the new magnet series production that will be tested in the next two years in the LASA laboratories.

Finally, the most innovative aspect of this thesis is the demonstration of the possibility to reconstruct the exact position of a quenched coil inside the final design of the HO corrector magnet after the quench event through the use of only the already developed and optimized magnetic measurement system installed at LASA laboratories. Using the simple rotating coil system to acquire the magnetic field of the magnet at zero current, the effect of the residual superconductor magnetization of the not quenched coils can be isolated and decomposed to detect in which of the magnet superconducting winding the quench has developed and propagated. In principle, this method is completely independent of the features of the analyzed magnet and it can be optimized and adjusted without affecting any aspect of the magnet configuration. The development process of the model has been presented enlightening the improvements in the simulation of the quench events recorded in the energizing test of the quadrupole MQSXFP1b assembly. Both an analytical model and FEM simulations, of the superconducting magnetization distribution effect on the residual magnetic field flux, have been developed and compared finding very good agreement with the data. Also, from experimental data, evidence of a correlation between the iron residual magnetization and the current decay rate has been observed. This anomalous behavior has not been specifically found in literature resulting to be a very interesting aspect to be studied during the series production of the HO corrector magnets.

To generalize the developed model for any type of magnet order m and be able

to detect in which one of the 2m coils the quench developed and propagated, we upgraded the already considered model focusing on the harmonic spectrum of an asymmetric configuration of the magnetized superconducting coil inside the magnet. The true power of the model stands in the ability to predict the initial phase and amplitude, of each single harmonic of the magnetic field produced, which are uniquely determined by the position of the quenched coil inside the magnet. The accuracy of the model and its predictions have been tested and compared during the cryogenic test of the first sextupolar magnet of the series production and the last assembly of the first skew quadrupole prototype. A perfect agreement with the standard QDS signal data has been found proving that we are able not only to evaluate the polarity of the magnet but also to specify which one of the superconducting coil has provoked the magnet discharge. The simplicity of the model and the diagnostic power which can be obtained from it make this new method a promising way to further improve the quench localization diagnostic systems of the superconducting magnets for particle accelerators.

BIBLIOGRAPHY

[1] Lucio; Rossi and Massimo Sorbi. QLASA: A Computer Code For Quench Simulation In Adiabatic Multicoil Superconducting Windings. pages 1–56, 2004.

[2] CERN STEAM webpage [ONLINE]. STEAM: Simulation of Transient Effects in Accelerator Magnets. URL: `https://espace.cern.ch/steam/`.

[3] Daniel Dominguez. 3D cut of the LHC dipole. Coupe 3D du dipôle du LHC. Jul 2014. General Photo.

[4] C. Wyss. LHC arc dipole status report. *Proceedings of the IEEE Particle Accelerator Conference*, 1:149–153, 1999.

[5] Animesh K. Jain. Basic Theory of Magnets. *CERN Accelerator School: Measurement and Alignment of Accelerator and Detector Magnets*, (2):1–26, 1997.

[6] The Nobel Prize in Physics. Nobel Media AB 2021, 2013.

[7] Observation of a new particle in the search for the standard model higgs boson with the atlas detector at the lhc. *Physics Letters B*, 716(1):1 – 29, 2012.

[8] Observation of a new boson at a mass of 125 gev with the cms experiment at the lhc. *Physics Letters B*, 716(1):30 – 61, 2012.

[9] G. Apollinari, O. Bruning, and L. Rossi. High Luminosity LHC - Project Description. *Cern Internal Reports, CERN-ACC*, Dec 2014.

[10] Giorgio Apollinari, I. Béjar Alonso, Oliver Brüning, M. Lamont, and Lucio Rossi. *High-luminosity large hadron collider (HL-LHC): Preliminary design report*. 2015.

[11] D Schoerling and A V Zlobin. *Nb3Sn Accelerator Magnets: Designs, Technologies and Performance*. 2019.

[12] E. Todesco, H. Allain, G. Ambrosio, G. Arduini, F. Cerutti, R. De Maria, L. Esposito, S. Fartoukh, P. Ferracin, H. Felice, R. Gupta, R. Kersevan, N. Mokhov, T. Nakamoto, I. Rakno, J. M. Rifflet, L. Rossi, G. L. Sabbi, M. Segreti, F. Toral, Q. Xu, P. Wanderer, and R. Van Weelderen. A first baseline for the magnets in the high luminosity LHC insertion regions. *IEEE Transactions on Applied Superconductivity*, 24(3), 2014.

[13] Jesus A. Garcia-Matos, Fernando Toral, and Paolo Fessia. Magnetic and Mechanical Design of the Nested Orbit Correctors for HL-LHC. *IEEE Transactions on Applied Superconductivity*, 26(4):1–5, 2016.

[14] Marco Statera, Franco Alessandria, Francesco Broggi, Augusto Leone, Samuele Mariotto, Antonio Paccalini, Danilo Pedrini, Mauro Quadrio, Massimo Sorbi, Maurizio Todero, Carlo Uva, Riccardo Valente, Paolo Fessia, Andrea Musso, and Ezio Todesco. Construction and cold test of the superferric decapole for the lhc luminosity upgrade. *IEEE Transactions on Applied Superconductivity*, 29(5):10–14, 2019.

[15] Radiation Applications. Epoxy Resin System Room Temperature Performance of CTD-101 Resin. pages 392–394.

[16] V. Kashikhin. A novel design of iron dominated superconducting multipole magnets with circular coils. *IEEE Transactions on Applied Superconductivity*, 20(3):196–199, 2010.

[17] V. Kashikhin and D. Turrioni. Hts quadrupole magnet for the persistent current mode operation. *IEEE Transactions on Applied Superconductivity*, 30(4):1–4, 2020.

[18] G. Volpini, J. Rysti, and M. Statera. Electromagnetic study of a round coil superferric magnet. *IEEE Transactions on Applied Superconductivity*, 26(4):1–5, June 2016.

[19] Samuele Mariotto, Vittorio Marinozzi, Juho Rysti, Massimo Sorbi, and Marco Statera. Study of a Sextupole Round Coil Superferric Magnet. 28(3):2–6, 2018.

[20] Samuele Mariotto, Augusto Leone, Antonio Paccalini, Alessandro Pasini, Danilo Pedrini, Mauro Quadrio, Massimo Sorbi, Marco Statera, Maurizio Todero, and Riccardo Valente. Activity on the Sextupole Round Coil Superferric Magnet Prototype at LASA. 29(5):14–18, 2019.

[21] Samuele Mariotto, Augusto Leone, Antonio Paccalini, Alessandro Pasini, Danilo Pedrini, Marco Prioli, Mauro Quadrio, Massimo Sorbi, Marco Statera, Maurizio Todero, and Riccardo Valente. Fabrication and Results of the First MgB 2 Round Coil Superferric Magnet at LASA. 30(4), 2020.

[22] Massimo Sorbi, Franco Alessandria, Giovanni Bellomo, Francesco Broggi, Augusto Leone, Vittorio Marinozzi, Samuele Mariotto, Andrea Musso, Antonio Paccalini, Danilo Pedrini, Mauro Quadrio, Marco Statera, Maurizio Todero, Ezio Todesco, and Carlo Uva. Status of the activity for the construction of the HL-LHC superconducting high order corrector magnets at LASA-milan. *IEEE Transactions on Applied Superconductivity*, 28(3):1–5, 2018.

[23] Marco Statera, Franco Alessandria, Giovanni Bellomo, Francesco Broggi, Augusto Leone, Samuele Mariotto, Antonio Paccalini, Alessandro Pasini, Danilo Pedrini, Marco Prioli, Massimo Sorbi, Mauro Quadrio, Riccardo Valente, Maurizio Todero, Carlo Uva, Andrea Musso, Ezio Todesco, Marco Campaniello, Marco Canetti, Fabrizio Gangini, Paolo Manini, and Alessandro Zanichelli. Construction and Power Test of the Superferric Skew Quadrupole for HL-LHC. *IEEE Transactions on Applied Superconductivity*, 30(4), 2020.

[24] Giovanni Volpini. *Cross talk between high order correctors and update on correctors*. WP3 Meeting, 2014, October, 9th.

[25] Martin N. Wilson. *Superconducting Magnets*. Clarendon Press, Oxford, U.K., Mar 1987.

[26] Emanuele Ravaioli. *CLIQ. A new quench protection technology for superconducting magnets*. PhD thesis, University of Twente, June 2015.

[27] E. Ravaioli, G. Ambrosio, B. Auchmann, P. Ferracin, M. Maciejewski, F. Rodriguez-Mateos, G. Sabbi, E. Todesco, and A. P. Verweij. Quench protection system optimization for the high luminosity lhc nb $_3$sn quadrupoles. *IEEE Transactions on Applied Superconductivity*, 27(4):1–7, 2017.

[28] M. Prioli, B. Auchmann, L. Bortot, M. Maciejewski, T. Salmi, and A. Verweij. Conceptual design of the fcc-hh dipole circuits with integrated cliq protection system. *IEEE Transactions on Applied Superconductivity*, 29(8):1–9, 2019.

[29] Crouvizier M. MCBXF Coils stacks analysis. *CERN EDMS 1554721*, 2016.

[30] Lucio Rossi and Massimo Sorbi. MATPRO: a Computer Library of Material Property at Cryogenic Temperature, January 2006. CARE-Note-2005-018-HHH.

[31] Andrew Davies. *Material properties data for heat transfer modeling in Nb3Sn magnets*. 2011.

[32] Eckels Engineering Inc. CryoComp. URL: `http://www.eckelsengineering.com/`, January 1993-2012. Rapid Cryogenic Design, 88 Materials in the Properties Database. Thermal Analysis Software.[ONLINE].

[33] Marco Statera, Franco Alessandria, Francesco Broggi, Augusto Leone, Vittorio Marinozzi, Samuele Mariotto, Antonio Paccalini, Danilo Pedrini, Mauro Quadrio, Massimo Sorbi, Maurizio Todero, Carlo Uva, Paolo Fessia, Andrea Musso, and Ezio Todesco. Construction and Cold Test of the Superferric Octupole for the LHC Luminosity Upgrade. 28(4):14–18, 2018.

[34] Vittorio Marinozzi. Protection of HO correctors. URL: `https://indico.cern.ch/event/647416`.

[35] E. Todesco, A. Musso, H. Prin, M. Sorbi, and M. Statera. Acceptance Criteria of INFN-LASA in-kind contribution (High Order Corrector Magnets). *CERN EDMS*.

[36] T. D. C. R. da Rosa and M. J. Bednarek. Electrical design criteria for the hl-lhc high order corrector magnets. *CERN EDMS*.

[37] M. Sorbi, F. Alessandria, G. Bellomo, F. Broggi, M. Campaniello, M. Canetti, A. Fumagalli, F. Gangini, A. Leone, S. Mariotto, A. Musso, A. Paccalini, A. Pasini, D. Pedrini, M. Quadrio, M. Statera, M. Todero,

E. Todesco, R. Valente, C. Uva, and A. Zanichelli. Construction and cold test of the superferric dodecapole high order corrector for the lhc high luminosity upgrade. *IEEE Transactions on Applied Superconductivity*, 29(5):1–5, 2019.

[38] M. Prioli, S. Mariotto, M. Sorbi, and M. Statera. Quench Protection Study for the High-Luminosity LHC High Order Corrector Magnets. *CERN EDMS*.

[39] Giorgio Bertotti. Chapter 14 - hysteresis in preisach systems. In Giorgio Bertotti, editor, *Hysteresis in Magnetism*, Electromagnetism, pages 479–506. Academic Press, San Diego, 1998.

[40] B. Osgood Peirce. The anomalous magnetization of iron and steel. *Proceedings of the American Academy of Arts and Sciences*, 47(17):633–670, 1912.

[41] C. P Bean. Magnetization of hard superconductors. *Physical review letters*, 8(6):250–253, 1962.

[42] Y. B. Kim, C. F. Hempstead, and A. R. Strnad. Critical persistent currents in hard superconductors. *Phys. Rev. Lett.*, 9:306–309, Oct 1962.

[43] P. W. Anderson. Theory of flux creep in hard superconductors. *Phys. Rev. Lett.*, 9:309–311, Oct 1962.

[44] Pasquale Arpaia, Marco Buzio, Susana Izquierdo Bermudez, Annalisa Liccardo, Alessandro Parrella, Mariano Pentella, Pedro M. Ramos, and Edvard Stubberud. A Superconducting Permeameter for Characterizing Soft Magnetic Materials at High Fields. *IEEE Transactions on Instrumentation and Measurement*, 69(7):4200–4209, 2020.

[45] Marco Buzio. IT4009 Low Carbon Steel, CERN MSC TM Presentation. [ONLINE]. URL: `https://indico.cern.ch/event/439191`.

[46] Zdzisław Włodarski. Analytical description of magnetization curves. *Physica B: Condensed Matter*, 373(2):323–327, 2006.

[47] G Ambrosio and G Bellomo. Magnetic field, multipole expansion and peak field in 2D for superconducting accelerator magnets. Technical Report INFN-TC-96-15, INFN, Rome, Oct 1996.

List of Figures

List of Tables

List of Abbreviations

ALICE	A Large Ion Collider Experiment
ATLAS	A Toroidal LHC ApparatuS
BCS	Bardeen Cooper Schrieffer
CERN	Conseil européen pour la recherche nucléaire
CLIQ	Coupling-Loss Induced Quench
CMS	Compact Muon Solenoid
CTD	Composite Technology Development Inc.
DFT	Discrete Fourier Transform
FDI	Fast Digital Integrator
FEM	Finite Element Method
FFMM	Flexible Framework for Magnetic Measurements
HL-LHC	High Luminosity Large Hadron Collider
HO	High Order Corrector Magnets
INFN	Istituto Nazionale di Fisica Nucleare
IP	Interaction Point of LHC collider
IR	Interaction Region of LHC collider
LASA	Laboratorio di Acceleratori e Superconduttività Applicata
LHCb	Large Hadron Collider beauty
MCU	Motor Control Unit
MgB_2	Magnesium Diboride
MIITs	Acronym for the quantities Mega-Current-Current-Time
MPZ	Minimum Propagating Zone
NbTi	Niobium Titanium superconductor material
Nb_3Sn	Niobium Tin superconductor material
PCB	Printed Circuit Boards
PID	Proportional Integral Derivative
QDS	Quench Detection System
RF	Radio Frequency
RRR	Residual Resistivity Ratio
SM	Standard Model of Particles
SSL	Short Sample Limit
SRV	Saes Rial Vacuum
TF	Transfer Function